

NOTA: anche questa pagina bianca fa parte del blocco di pagine della tesi

NOTA: tagliare il blocco di pagine della tesi (stampata fronte-retro)  
lungo le due linee qui tracciate prima di effettuare la rilegatura





UNIVERSITÀ DEGLI STUDI DI CATANIA

FACOLTÀ DI INGEGNERIA

DOTTORATO DI RICERCA IN INGEGNERIA ELETTRONICA, AUTOMATICA  
E DEL CONTROLLO DI SISTEMI COMPLESSI

XXIV CICLO

ANGELA BENINATO

**Development of innovative transducers based on  
Magnetic Fluids**

Ph.D. Thesis

*Tutor:* Prof. Ing. Salvatore Baglio

*Coordinator:* Prof. Ing. Luigi Fortuna

*December 2011*



*To Alessandro*



# *Acknowledgements*

During the period of my Doctorate I had the support of many people who contributed, in different ways, to the realization of this work.

First of all I would like to thank my guardian Angels, my parents, whose sacrifices allowed me to reach this important achievement, and my brother Danio, whose support was very important for me.

A very special thank to Alessandro, who always sustained and encouraged me with love and patience and who believed in me and in this project. He stood by me in the most difficult periods of my life, helping me to overcome them. He was and he is my light in the dark. For all these reasons and for much more this Thesis is dedicated to him.

I want to say how grateful I am to Prof. Salvatore Baglio and Prof. Bruno Andò for the thrust they had in me and for all their lessons and

suggestions; they were an inexhaustible source of ideas, inspirations and enthusiasm, and I have learned a lot from them.

I would like to thank Prof. Luigi Fortuna, Coordinator of my Ph.D. course, for the opportunity he gave to me.

I want to say thanks to my colleagues Elena, Vincenzo, Carlo, Salvo and Gaetano for the several mutual information exchanges that have been very relevant to improve my knowledge, and for making my working days very pleasant.



# *Preface*

The investigation of new approaches and methodologies for the development of sensors and actuators is strictly related to the investigation of novel materials and technologies allowing for widening devices usability well beyond traditional fields of applications.

Actually, the use of novel materials can permit the development of sensing methodologies and readout strategies with interesting peculiarities.


This Ph.D. thesis addresses the possibility to exploit magnetic fluids for the realization of innovative sensors and actuators. The use of such “shapeless” materials allows the synthesis of transducers with dramatic features especially in terms of reliability to mechanical shocks and architectural flexibility which opens the use of these devices to a wide range of real applications.

Above a general introduction on magnetic fluids and their standard applications, the thesis covers aspects related to innovative sensing strategies adopting a ferrofluid sample as the active inertial mass of the transducer. Novel ideas, design, models, simulations, implementation of lab-scale prototypes and their metrological characterizations are the main contributions of this Ph.D. Thesis.

The Thesis content is really deep and, although rich of already concrete methodologies assessed by real working devices, in my opinion it represents a milestone in the context of ferrofluid transducers stimulating further research activities in this field.

This Thesis resumes an intense research activity that Angela well conducted within the research group working in the sensor laboratory at the DIEEI in Catania. Reading this work evidences the original and valuable contribution of the author in the field of innovative transducers using ferrofluids, her competencies and scientific maturity.

I would like to give to Angela my personal compliments for this exhaustive and high level job and I wish the best for her future job and success for her life.

A handwritten signature in blue ink, appearing to read "Antonio Picerno", with a horizontal line underneath.

# Contents

|   |          |
|---|----------|
| <b>INTRODUCTION .....</b>                       | <b>1</b> |
| <b><u>CHAPTER 1</u></b>                         |          |
| <b>THE MAGNETISM .....</b>                      | <b>5</b> |
| 1.1. MAGNETISM IN MATTER .....                  | 5        |
| 1.2. CLASSIFICATION OF MAGNETIC MATERIALS ..... | 7        |
| <i>Ferromagnetism</i> .....                     | 8        |
| <i>Paramagnetism</i> .....                      | 11       |
| <i>Diamagnetism</i> .....                       | 12       |
| <i>Antiferromagnetism</i> .....                 | 12       |
| <i>Ferrimagnetism</i> .....                     | 13       |
| 1.3. SOURCES OF MAGNETIC FIELD .....            | 15       |
| <i>Electromagnets</i> .....                     | 15       |
| <i>Permanent magnets</i> .....                  | 17       |
| 1.4. MAGNETIC SENSORS.....                      | 19       |

|  |    |
|--|----|
| <i>Magnetic field sensors</i> .....                                  | 20 |
| <i>Sensors of magnetic quantities</i> .....                          | 22 |
| <i>Sensors exploiting magnetic forces as working principle</i> ..... | 23 |

## **CHAPTER 2**

|  |           |
|--|-----------|
| <b>FERROFLUIDS AND THEIR APPLICATIONS</b> .....          | <b>25</b> |
| 2.1. FERROFLUIDS.....                                    | 25        |
| 2.2. APPLICATIONS OF FERROFLUIDS .....                   | 30        |
| <i>Commercial applications of ferrofluids</i> .....      | 31        |
| <i>Biomedical applications of ferrofluids</i> .....      | 32        |
| <i>Transducers based on the use of ferrofluids</i> ..... | 34        |
| 2.3. EFH1 FERROFLUID BY FERROTEC .....                   | 37        |
| 2.4. MAIN FORCES ACTING ON A FERROFLUID MASS .....       | 38        |

## **CHAPTER 3**

|  |           |
|--|-----------|
| <b>SENSORS BASED ON FERROFLUIDS</b> .....                      | <b>43</b> |
| 3.1. A FERROFLUID GYROSCOPE .....                              | 44        |
| <i>The working principle</i> .....                             | 45        |
| <i>The sensing strategy</i> .....                              | 47        |
| <i>The model</i> .....   | 50        |
| <i>The experimental results</i> .....                          | 62        |
| 3.2. AN INERTIAL SENSOR EXPLOITING A SPIKE SHAPED FERROFLUID . | 64        |
| <i>The working principle</i> .....                             | 65        |
| <i>The sensing strategy</i> .....                              | 68        |
| <i>The model</i> .....   | 71        |
| <i>The experimental results</i> .....                          | 72        |
| 3.3. A FERROFLUID FLOW SENSOR.....                             | 77        |
| <i>The working principle</i> .....                             | 79        |
| <i>The sensing strategy</i> .....                              | 80        |

|  |            |
|--|------------|
| <i>The model</i> .....   | 81         |
| <i>The experimental results</i> .....  | 89         |
| 3.4. A FERROFLUID INCLINOMETER WITH A TIME DOMAIN READOUT                        |            |
| STRATEGY .....   | 92         |
| <i>The working principle</i> .....   | 93         |
| <i>The model</i> .....   | 100        |
| <i>The real device</i> .....   | 101        |
| <b><u>CHAPTER 4</u></b>  |            |
| <b>ACTUATORS BASED ON FERROFLUIDS .....</b>                                      | <b>109</b> |
| 4.1. THE “ONE DROP” FERROFLUID PUMP .....  | 110        |
| <i>The pump architecture</i> .....   | 112        |
| <i>The actuation strategy</i> .....  | 114        |
| <i>The prototype realization</i> .....   | 123        |
| <i>Characterization of the FP1_A pump</i> .....                                  | 125        |
| <i>An IR based methodology for the validation of the pumping mechanism</i> ..... | 134        |
| 4.2. PATH TRACKING OF FERROFLUID SAMPLES FOR BIO-SENSING                         |            |
| APPLICATIONS .....   | 140        |
| <i>The working principle</i> .....   | 142        |
| <i>The device</i> .....  | 144        |
| <i>The GUI for path definition and tracking</i> .....                            | 146        |
| <i>The experimental results</i> .....  | 147        |
| <b><u>CHAPTER 5</u></b>  |            |
| <b>TOWARDS INTEGRATED MICROFLUID MAGNETIC DEVICES .....</b>                      | <b>149</b> |
| 5.1. AN INTEGRATED DEVICE FOR BIOLOGICAL MEASUREMENTS .....                      | 150        |
| <i>The device architecture</i> .....   | 151        |
| <i>The magnetic sensor</i> .....   | 152        |
| 5.2. A MULTI-SENSING STRUCTURE FOR INERTIAL MEASUREMENTS ..                      | 161        |

|   |            |
|---|------------|
| <b>CONCLUSIONS .....</b>                          | <b>163</b> |
| <b>REFERENCES .....</b>                           | <b>165</b> |
| <b>LIST OF PUBLICATIONS.....</b>                  | <b>173</b> |
| <i>Book contributions .....</i>                   | 173        |
| <i>International journals .....</i>               | 174        |
| <i>International conference proceedings .....</i> | 175        |
| <i>National conference proceedings .....</i>      | 176        |

## *List of figures*

|  |    |
|--|----|
| FIGURE 1-1 A) RANDOM ORIENTATION OF ATOMIC MAGNETIC MOMENTS IN AN UNMAGNETIZED SUBSTANCE. B) WHEN AN EXTERNAL FIELD $\mathbf{B}_0$ IS APPLIED, THE ATOMIC MAGNETIC MOMENTS TEND TO ALIGN WITH THE FIELD, GIVING THE SAMPLE A NET MAGNETIZATION VECTOR $\mathbf{M}$ . ..... | 9  |
| FIGURE 1-2 IN BULK FERROMAGNETIC MATERIALS DIPOLE ALIGNMENT IS SPLIT UP INTO DOMAINS.....  | 10 |
| FIGURE 1-3 MAGNETIC HYSTERESIS LOOPS FOR SOFT AND HARD MATERIALS.....  | 11 |
| FIGURE 1-4 TYPES OF MAGNETISM: PARAMAGNETISM, FERROMAGNETISM, ANTIFERROMAGNETISM AND FERRIMAGNETISM. ....  | 14 |
| FIGURE 1-5 BEHAVIOR OF THE MAGNETIC FIELD PRODUCED BY AN ELECTROMAGNET CENTERED IN $x = 0\text{ m}$ WITH A RADIUS $R = 0.008\text{ m}$ .   | 17 |
| FIGURE 1-6 BEHAVIOR OF THE MAGNETIC FIELD PRODUCED BY A PERMANENT MAGNET CENTERED IN $x = 0\text{ m}$ AND WITH A RADIUS $R = 0.005\text{ m}$ . ....  | 19 |

|   |    |
|---|----|
| FIGURE 1-7 MAGNETIC FIELD SENSORS ARE DIVIDED INTO TWO CATEGORIES BASED ON THEIR FIELD STRENGTHS AND MEASUREMENT RANGE: MAGNETOMETERS MEASURE LOW FIELDS AND GAUSSMETERS MEASURE HIGH FIELDS. ....  | 22 |
| FIGURE 2-1 SCHEMATIC OF FERROFLUID PARTICLES, WITH HIGHLIGHTED THE MAGNETIC CORE AND THE SURFACTANT. ....   | 27 |
| FIGURE 2-2 EXAMPLES OF FERROFLUIDS SUBJECTED TO MAGNETIC FIELDS. ....   | 29 |
| FIGURE 2-3 STRUCTURAL LATTICES FORMED IN A THIN LAYER OF THE MAGNETIC FLUID EXPOSED TO AN ALTERNATING ELECTRIC FIELD AT DIFFERENT FREQUENCIES: A) 2 kHz AND B) 10 kHz. ....   | 29 |
| FIGURE 2-4 $B$ VS $H$ , AND $\mu r$ VS $H$ FOR EFH1 FERROFLUID. ....  | 38 |
| FIGURE 2-5 QUALITATIVE BEHAVIOR OF THE MAGNETIC FORCE PRODUCED BY AN ELECTROMAGNET. ....  | 41 |
| FIGURE 3-1 SCHEMATIZATION OF THE FERROFLUID GYROSCOPE. ....   | 45 |
| FIGURE 3-2 SCHEMATIC OF THE MOTION OF THE FERROFLUID MASS A) WITHOUT ANGULAR RATE AND B) WITH ANGULAR RATE. THE DISTANCE $D$ DEPENDS ON THE ANGULAR RATE AMPLITUDE ACTING ON THE SYSTEM. ....   | 46 |
| FIGURE 3-3 BLOCK DIAGRAM OF THE DRIVING ELECTRONICS. ....   | 47 |
| FIGURE 3-4 SCHEMATICS OF THE READOUT SENSING ELECTRONICS. ....  | 48 |
| FIGURE 3-5 A TYPICAL FRAME AND THE SUPERIMPOSED GRID WITH A RESOLUTION OF 5 mm. ....  | 51 |
| FIGURE 3-6 TIME EVOLUTION OF THE FERROFLUID MASS (0.1 ml) POSITION FOR A DRIVING SIGNAL OF: A) 1.4 Vpp @690 mHz, B) 1.4 Vpp @500 mHz C) 1.4 Vpp @1 Hz, AND FOR TWO DIFFERENT TILTS. CASES B) AND C) ARE EXAMPLES WHERE THE FERROFLUID MASS FAILS TO FOLLOW THE DRIVING SIGNAL. .... | 52 |
| FIGURE 3-7 DRIVING PARAMETER MAP HIGHLIGHTING THE OPTIMAL WORKING REGION (TILT=0°). ....  | 53 |
| FIGURE 3-8 REAL VIEW OF THE SENSOR ARRAY USED FOR THE ESTIMATION OF THE ELECTROMAGNETS FIELDS. ....   | 54 |
| FIGURE 3-9 SCHEMATIZATION OF THE SENSOR ARRAY USED TO MEASURE THE GENERATED MAGNETIC FIELDS. ....   | 55 |



|  |    |
|--|----|
| FIGURE 3-10 SPATIO-TEMPORAL BEHAVIOR OF THE MAGNETIC FIELD MEASURED ALONG THE DRIVING AXIS DUE TO ONE ELECTROMAGNET..  | 55 |
| FIGURE 3-11 EVOLUTION OF THE MAGNETIC FIELD AND THE MAGNETIC FORCE ALONG THE DRIVING AXIS. ....  | 56 |
| FIGURE 3-12 TIME EVOLUTION OF THE MAGNETIC FORCE, THE MAGNETIC FIELD AND THE FERROFLUID MASS POSITION A) IN A GENERIC POINT ALONG THE DRIVING AXIS, AND B) IN THE LOCATION OF ONE ELECTROMAGNET.....   | 57 |
| FIGURE 3-13 BEHAVIOUR OF THE MAGNETIC FIELD AND THE MAGNETIC FORCE ALONG THE DRIVING AXIS FOR THE SPECIFIC TIME SLOT WHERE THE MAGNETIC FIELD AMPLITUDE REACHES ITS MAXIMUM VALUE (SCALING FACTORS GIVEN IN THE VERTICAL AXIS LABEL HAVE BEEN USED FOR THE SAKE OF CONVENIENCE). ....  | 58 |
| FIGURE 3-14 MODEL OF THE NUMERICAL INTEGRATION ADOPTED.....  | 59 |
| FIGURE 3-15 COMPARISON BETWEEN THE EXPERIMENTAL AND THE PREDICTED EVOLUTION OF THE FERROFLUID MASS. ....   | 60 |
| FIGURE 3-16 SIMULATION RESULTS OF THE MASS TRAJECTORY INTERSECTIONS WITH THE Y AXIS AS A FUNCTION OF THE IMPOSED ANGULAR RATE.....   | 61 |
| FIGURE 3-17 EXPERIMENTAL SET-UP ADOPTED FOR THE DEVICE CHARACTERIZATION; A) SENSING-DRIVING SYSTEM AND B) STEP MOTOR. ....   | 63 |
| FIGURE 3-18 CALIBRATION DIAGRAM OF THE FERROFLUID GYROSCOPE...   | 64 |
| FIGURE 3-19 SCHEMATIZATION OF FORCES ACTING ON THE FERROFLUID MASS: $F_m$ IS THE MAGNETIC FORCE, $F_g$ IS THE GRAVITATIONAL FORCE AND $F_{si}$ IS THE HYDROSTATIC FORCE. ON THE LEFT HAND SIDE THE STEADY STATE REGIME IS SHOWN; ON THE RIGHT HAND SIDE AN EXTERNAL STIMULUS PERTURBS THE SYSTEM AND THE FREE-END OF THE FERROFLUID SPIKE CHANGES ITS POSITION. THE DIODE USED TO PRODUCE THE IR EMISSION IS REPRESENTED WITH FOUR YELLOW AND SYMMETRICALLY ARRANGED CIRCULAR RING SEGMENTS, WHILE THE PHOTODIODE IS REPRESENTED WITH A FILLED YELLOW CIRCLE. .... | 66 |
| FIGURE 3-20 BLOCK DIAGRAM OF THE READOUT STRATEGY. THE FIRST BLOCK IN THE LEFT-HAND SIDE IS THE PIPETTE WITH THE SPIKE SHAPED FERROFLUID MASS; THE SECOND BLOCK REPRESENTS THE   |    |

|   |    |
|---|----|
| CONVERSION BETWEEN THE FERROFLUID DISPLACEMENT AND THE IRRADIATED AREA OF THE IR DEVICE; THE LAST BLOCK IN THE RIGHT-HAND SIDE REPRESENTS THE IR DEVICE. A VOLTAGE TO CURRENT CONVERTER WAS USED TO DRIVE THE IR TRANSMITTER, WHILE A STANDARD VOLTAGE DIVIDER WAS USED TO OBTAIN AN OUTPUT VOLTAGE FROM THE IR DEVICE..... | 68 |
| FIGURE 3-21 SCHEMATIZATION OF THE INTERACTION BETWEEN THE FERROFLUID SPIKE AND THE IR DEVICE.....   | 69 |
| FIGURE 3-22 THE RELATIONSHIP BETWEEN THE DISPLACEMENT OF THE FERROFLUID SPIKE (FREE-END) AND THE IRRADIATED AREA. A LINEAR FITTING BY MODEL $y = 0.7x + 0.06$ PRODUCES AN ESTIMATED RESIDUAL OF $0.008 \text{ mm}^2$ . .....  | 70 |
| FIGURE 3-23 A) REAL VIEW OF THE DEVICE; B) ZOOM OF THE FERROFLUID SPIKE; THE IR EMITTER DIODE IS REPRESENTED BY A DOTTED CIRCLE WHILE THE PHOTODIODE IS REPRESENTED BY A FILLED WHITE CIRCLE. ....  | 72 |
| FIGURE 3-24 CONDITIONING ELECTRONICS USED FOR A) DIODE AND B) PHOTODIODE. ....  | 73 |
| FIGURE 3-25 EXPERIMENTAL SET-UP FOR THE DEVICE CHARACTERIZATION. ....   | 74 |
| FIGURE 3-26 FREQUENCY RESPONSE OF THE SHAKER.....   | 75 |
| FIGURE 3-27 FREQUENCY RESPONSE OF THE DEVICE.....   | 75 |
| FIGURE 3-28 CALIBRATION DIAGRAMS FOR STIMULI A) @4 Hz AND B) @8 Hz. DOTTED LINES REPRESENT THE UNCERTAINTY BAND ESTIMATED. ....   | 77 |
| FIGURE 3-29 SCHEMATIZATION OF FLOW SENSOR. ....   | 80 |
| FIGURE 3-30 CONDITIONING ELECTRONIC FOR THE INDUCTIVE READOUT STRATEGY. ....  | 80 |
| FIGURE 3-31 THE FERROFLUID SPIKE INSIDE THE PIPE FOR A) NULL FLOW RATE AND B) $0.3 \text{ ml/s}$ . THE MASS OF FERROFLUID CHANGES ITS SHAPE DUE TO THE TIP MOVEMENT .....   | 82 |
| FIGURE 3-32 THE FERROFLUID SPIKE INSIDE THE PIPE FOR A) NULL FLOW RATE, B) $1 \text{ ml/s}$ AND C) $1.7 \text{ ml/s}$ . THE MASS OF FERROFLUID CHANGES BOTH ITS SHAPE (TIP DEFLECTION) AND POSITION. ....   | 83 |

|  |     |
|--|-----|
| FIGURE 3-33 BEHAVIORS OF THE FERROFLUID SPIKE TIP DISPLACEMENT, X, AS A FUNCTION OF THE FLOW RATE INTENSITY FOR DIFFERENT VALUES OF THE RETAINING MAGNETIC FIELD. ....   | 84  |
| FIGURE 3-34 TWO TYPICAL FRAMES FOR THE ESTIMATION OF THE FERROFLUID SPIKE TIP POSITION. ....   | 85  |
| FIGURE 3-35 SIMULATED FREQUENCY RESPONSES OF THE DEVICE. ....  | 88  |
| FIGURE 3-36 SIMULATED STEP RESPONSES (FOR $Q=1$ ml/s) OF THE DEVICE. ....  | 88  |
| FIGURE 3-37 A) REAL VIEW OF THE FLOW SENSOR; B) EXPERIMENTAL SET-UP ADOPTED TO CHARACTERIZE THE SENSOR PROTOTYPE. ....   | 90  |
| FIGURE 3-38 THE SENSOR RESPONSE FOR RETAINING MAGNETIC FIELDS OF 133 G, 153 G AND 186 G. ....  | 90  |
| FIGURE 3-39 SCHEMATIZATION OF THE DEVELOPED TDR INCLINOMETER. ....   | 94  |
| FIGURE 3-40 BLOCK DIAGRAM OF THE SENSOR WORKING PRINCIPLE. ....  | 96  |
| FIGURE 3-41 QUALITATIVE BEHAVIOR OF THE SIGNAL MODULATION DUE TO THE MASS MOVEMENT: $\theta_1 < \theta_2 < \theta_3$ . ....  | 98  |
| FIGURE 3-42 A SCHEME OF THE ELECTRONICS USED TO DRIVE THE ACTUATION COIL. ....   | 99  |
| FIGURE 3-43 A SCHEME OF THE ELECTRONICS USED TO SENSE THE MASS POSITION. ....  | 99  |
| FIGURE 3-44 REAL VIEW OF THE DEVELOPED PROTOTYPE. ....   | 101 |
| FIGURE 3-45 SNAPSHOTS OF THE REALIZED INTERFACE: A) CONTROL OF THE TILT, B) COMPARISON OF THE OUTPUT SIGNAL WITH THE TWO THRESHOLD VALUES AND MONITORING OF THE SIGNAL PROCESSING, C) ACQUISITION OF THE OUTPUT DATA. .... | 103 |
| FIGURE 3-46 OUTPUT SIGNALS OBTAINED IMPOSING DIFFERENT TILT VALUES. ....   | 105 |
| FIGURE 3-47 COMPARISON BETWEEN TWO OUTPUT SIGNAL WITH CONSECUTIVE VALUES OF IMPOSED TILT. ....   | 106 |
| FIGURE 3-48 POWER SPECTRUM DENSITY VS FREQUENCY FOR FOUR DIFFERENT IMPOSED TILTS: A) $1.2^\circ$ , B) $4.8^\circ$ , C) $8.4^\circ$ AND D) $13.2^\circ$ . IT IS EVINCIBLE THAT THE PEAK DEPENDS ON THE TILT. ....           | 108 |
| FIGURE 3-49 CALIBRATION MODEL OF THE TDR INCLINOMETER. ....  | 108 |

|  |     |
|--|-----|
| FIGURE 4-1 SCHEMATIC OF THE PROPOSED DESIGN FOR FP1 PUMP ARCHITECTURE. IT IS POSSIBLE TO VIEW THE MAGNETIC VOLUME FLATTENED IN THE CHANNEL DUE TO THE MAGNETIC FORCE APPLIED BY THE PERMANENT MAGNET, THE POLARIZATION OF THE ELECTROMAGNET AND THE COILS, USED TO CREATE AND MOVE THE CAP OF MAGNETIC FLUID IN THE GLASS PIPE, WOUNDED AROUND PIPE AND MAGNET. .... | 113 |
| FIGURE 4-2 SCHEMATIZATION OF THE ACTUATION STRATEGY USED TO PUMP THE LIQUID FROM THE LEFT TO THE RIGHT SIDE OF THE PIPE. .   | 115 |
| FIGURE 4-3 THE BEHAVIOUR OF THE TOTAL MAGNETIC FORCE INSIDE THE CHANNEL AND THE CONDITION FOR THE CAP FORMATION. THE DRIVING SIGNALS CONSIDERED ARE OF $400 \text{ mApp} @ 0.5 \text{ Hz}$ , WHILE OTHER SIMULATION PARAMETERS ARE EVINCIBLE BY TABLE 4-1. ....  | 116 |
| FIGURE 4-4 TIME EVOLUTION OF THE CAP POSITION FOR DIFFERENT PHASE LAGS. THE FERROFLUID CAP CAN BE MOVED FROM THE LEFT TO THE RIGHT OF THE ACTIVE AREA. EACH PLOT SHOWS THE IDEAL CAP TRAJECTORY (THE CONTINUOUS LINE) AND THE SIMULATED BEHAVIOUR (SYMBOLS). ELECTROMAGNETS ARE DRIVEN WITH SIGNALS WITHOUT SUPERIMPOSED BIAS. ....                                  | 119 |
| FIGURE 4-5 THE J INDEX ADOPTED FOR THE OPTIMIZATION OF THE PHASE LAG BETWEEN THE DRIVING SIGNALS.....  | 120 |
| FIGURE 4-6 TIME EVOLUTION OF THE CAP POSITION FOR DIFFERENT PHASE LAGS. THE FERROFLUID CAP CAN BE MOVED FROM THE LEFT TO THE RIGHT OF THE ACTIVE AREA. EACH PLOT SHOWS THE IDEAL CAP TRAJECTORY (THE CONTINUOUS LINE) AND THE SIMULATED BEHAVIOR (SYMBOLS). ELECTROMAGNETS ARE DRIVEN WITH SIGNAL WITH OFFSET. ....  | 122 |
| FIGURE 4-7 EVOLUTION OF $J$ AS FUNCTION OF THE PHASE LAG. ....   | 123 |
| FIGURE 4-8 THE FERROFLUID PUMP, FP1, PROTOTYPE: VIEW OF THE ACTUATION SYSTEM WRAPPED AROUND THE GLASS PIPE AND OF THE MAGNET. ....   | 123 |
| FIGURE 4-9 EXPERIMENTAL SETUP USED TO CHARACTERIZE THE FP1_A PUMP.....   | 125 |

|   |     |
|---|-----|
| FIGURE 4-10 RESULTS OBTAINED THROUGH THE DEVICE CHARACTERIZATION PROCEDURE. THE DRIVING CURRENT HAS BEEN FIXED TO: A) 300 $mApp$ , B) 400 $mApp$ , AND C) 450 $mApp$ .....  | 128 |
| FIGURE 4-11 RESULTS OBTAINED THROUGH THE DEVICE CHARACTERIZATION PROCEDURE. THE DRIVING CURRENT HAS BEEN FIXED TO: A) 180 $mApp$ + 90 $mAdc$ , B) 200 $mApp$ + 100 $mAdc$ AND C) 230 $mApp$ + 115 $mAdc$ . .....  | 129 |
| FIGURE 4-12 THRESHOLD PRESSURE AND THE CORRESPONDING PUMP FLOW RATE AS A FUNCTION OF THE EXCITATION CURRENT: A) SIGNALS WITHOUT SUPERIMPOSED BIAS AND B) SIGNAL WITH SUPERIMPOSED BIAS. ....  | 130 |
| FIGURE 4-13 DP <sub>MAX</sub> VS FREQUENCY: A) SIGNALS WITHOUT SUPERIMPOSED BIAS AND B) SIGNALS WITH SUPERIMPOSED BIAS. ....  | 131 |
| FIGURE 4-14 AMOUNT OF PUMPED LIQUID IN VACUUM. ....   | 132 |
| FIGURE 4-15 A) AVERAGE AMOUNT OF PUMPED LIQUID FOR THE TWO DIFFERENT TANKS AND B) MAXIMUM DROP PRESSURE FOR THE TWO DIFFERENT TANKS.....  | 133 |
| FIGURE 4-16 THE SENSING ARCHITECTURE REALIZED TO OBSERVE THE CAP EVOLUTION INSIDE THE CHANNEL. A) SCHEMATIZATION OF THE DEVICE HOUSING THE IR SENSOR ARRAY; B) A REAL VIEW OF THE IR SENSOR ARRAY. ....   | 135 |
| FIGURE 4-17 TIME EVOLUTION OF SIGNALS, $V_{sl}$ , COMING FROM EACH SENSOR OF THE IR-LED ARRAY DURING EXPERIMENTS ASSESSING THE OPERATION OF THE SENSING STRATEGY ADOPTED TO SENSE THE FERROFLUID CAP POSITION INSIDE THE CHANNEL. A) THE WHOLE SIGNAL EVOLUTIONS; B) A DETAIL OF A CAP EVOLUTION FROM THE LEFT-HAND SIDE TO THE RIGHT-HAND SIDE OF THE ACTUATION AREA, CORRESPONDING TO THE TIME INTERVAL HIGHLIGHTED IN FIGURE 4A; C) SYNTHESIS OF THE RESULTS SHOWN IN FIGURE 4-17B. .... | 136 |
| FIGURE 4-18 TIME EVOLUTION OF SIGNALS COMING FROM THE IR-LED ARRAY DURING A PUMPING SESSION. A) ORIGINAL SIGNALS AND B) FILTERED SIGNALS. THE DRIVING SIGNAL PARAMETERS ARE: 200 $mA$ + 100 $mAdc$ @ 0.6 $Hz$ .....   | 138 |
| FIGURE 4-19 OBSERVED EVOLUTION OF THE CAP POSITION DURING A PUMPING SESSION (DIAGONAL BANDS) AND COMPARISON WITH THE  |     |

|  |     |
|--|-----|
| THEORETICAL TREND (SOLID LINE) IN FIGURE 4-6. FORCING SIGNALS PARAMETERS ARE: A) $200\text{ mApp} + 100\text{ mAdc} @ 1\text{ Hz}$ AND B) $0.6\text{ Hz}$ ...  | 139 |
| FIGURE 4-20 SCHEMATIZATION OF THE MECHANISM OF MAGNETIC LABELLING: THE ANTIGEN IS LINKED ON THE ONE HAND WITH A CAPTURING ANTIBODY AND ON THE OTHER HAND WITH A DETECTING ANTIBODY, LINKED WITH THE MAGNETIC MARKER COATED WITH A BIOCOMPATIBLE MOLECULE.....  | 140 |
| FIGURE 4-21 A) SCHEMATIZATION OF THE MATRIX OF THE SITES IN WHICH FERROFLUID CAN BE STATES AND B) SCHEMATIZATION OF THE MAGNETIC ACTUATION SYSTEM.....   | 143 |
| FIGURE 4-22 BLOCK DIAGRAM OF THE SEQUENCE PERFORMED TO MOVE THE MASS FROM THE A POSITION TO THE B POSITION.....  | 144 |
| FIGURE 4-23 REAL VIEW OF THE REALIZED PROTOTYPE.....   | 144 |
| FIGURE 4-24 SCHEME OF THE ELECTRONICS.....   | 145 |
| FIGURE 4-25 A PICTURE OF THE REALIZED INTERFACE IN LABIEW® SOFTWARE.....   | 146 |
| FIGURE 4-26 FRAMES OF A VIDEO SHOWING THE MOVEMENT OF THE FERROFLUID MASS ALONG A PRE-DEFINED PATH.....  | 147 |
| FIGURE 4-27 NUMBER OF SUCCESSFUL TRANSITIONS BETWEEN TWO ADJACENT POSITIONS VS MINIMUM TIME STEP BETWEEN THE INPUT SIGNAL FOR TWO CONSECUTIVE ELECTROMAGNETS.....  | 148 |
| FIGURE 5-1 THE FUNCTIONAL BLOCK SCHEME OF THE LAB ON CHIP SYSTEM EMBEDDING THE INDUCTIVE SENSOR FOR MAGNETIC BEADS. ....   | 152 |
| FIGURE 5-2 WORKING PRINCIPLE OF THE PLANAR DIFFERENTIAL TRANSFORMER. ....  | 154 |
| FIGURE 5-3 SCHEMATIC OF THE CROSS-SECTION ALONG A RADIAL DIRECTION. ....   | 156 |
| FIGURE 5-4 DISTRIBUTION OF THE MAGNETIC FIELD PRODUCED BY THE PRIMARY COIL AND VIEW OF THE SECONDARY COILS (TOP). ZOOM OF THE AREA INSIDE THE ACTIVE COIL (THE ONE AT THE RIGHT IN THE TOP FIGURE) BOTH IN ABSENCE -PICTURE B) ON THE TOP SIDE- AND IN PRESENCE -PICTURE B) IN THE BOTTOM SIDE- OF MAGNETIC BEADS. . | 157 |
| FIGURE 5-5 THE DEDICATED TECHNOLOGY USED TO REALIZE THE DIFFERENTIAL INDUCTIVE SENSOR. ....  | 158 |

|  |     |
|--|-----|
| FIGURE 5-6 PICTURES OF THE ACTIVE SECONDARY COIL WITH DIFFERENT DEPOSITION OF MAGNETIC PARTICLES: A) QUANTITY $Q_1$ ; B) QUANTITY $Q_2=2*Q_1$ AND C) QUANTITY $Q_3=10*Q_1$ ..... | 159 |
| FIGURE 5-7 SENSOR OUTPUT VOLTAGE WITH DIFFERENT AMOUNT OF DEPOSITED MAGNETIC PARTICLES.....  | 160 |
| FIGURE 5-8 MEAN VALUE OF THE SENSOR OUTPUT AS FUNCTION OF THE MAGNETIC PARTICLES AMOUNT.....   | 160 |
| FIGURE 5-9 SCHEMATIZATION OF THE MULTI-SENSING STRUCTURE. ....   | 162 |





## *List of tables*

|  |     |
|--|-----|
| TABLE 1-1 COMPARISON BETWEEN DIFFERENT KIND OF MAGNETIC MATERIALS AS FUNCTION OF PERMEABILITY AND SUSCEPTIBILITY ..... | 15  |
| TABLE 2-1 PHYSICAL PROPERTIES OF THE EFH1 FERROFLUID. ....   | 38  |
| TABLE 3-1 SPECIFICATIONS OF DRIVING ELECTROMAGNETS AND PLANAR COILS. ....  | 48  |
| TABLE 3-2 ELECTRICAL PARAMETERS OF ENCODER. ....   | 62  |
| TABLE 3-3 LASER SPECIFICATIONS.....  | 74  |
| TABLE 3-4 SUMMARY OF THE DEVICE PERFORMANCES AS A FUNCTION OF THE RETAINING MAGNETIC FIELD. ....                       | 87  |
| TABLE 3-5 CALIBRATION MODELS OF THE FLOW SENSOR IN DIFFERENT OPERATING CONDITIONS. ....                                | 91  |
| TABLE 3-6 DEVICE SPECIFICATIONS FOR THREE DIFFERENT VALUES OF THE RETAINING MAGNETIC FIELD. ....                       | 91  |
| TABLE 3-7 PARAMETER VALUES OF THE DRIVING SYSTEM.....  | 104 |
| TABLE 3-8 PARAMETER VALUES OF THE SENSING SYSTEM. ....   | 104 |
| TABLE 4-1 CHARACTERISTIC OF ELECTROMAGNETS USED IN THE MATLAB® SIMULATION. ....  | 117 |

|   |     |
|---|-----|
| TABLE 4-2 OPERATIVE CONDITIONS OF THE ELECTROMAGNET AS<br>FUNCTION OF THE DESIRED CURRENT VALUE. .... | 145 |
| TABLE 5-1 GEOMETRIC CHARACTERISTICS OF DIFFERENTIAL<br>TRANSFORMER. ....                              | 156 |
| TABLE 5-2 OPTIMIZED INDUCTIVE MICROSENSOR PARAMETERS. ....  | 158 |

# *Introduction*

It is quite common, in the advances on scientific research, to witness how material properties are exploited toward sensing applications in order to realize novel devices with high performances and tunable characteristics.

The synthesis of materials that are not in nature but that are realized in chemical laboratories is often a response to such a requirement.

In particular “meta” materials and, in general, those materials made by the aggregation of several components to result into a multi-phase compound, are often very flexible and can provide very interesting performance in many different application fields.

Among these, magnetic materials have gained great relevance thanks to the possibility of controlling many of their features via external magnetic fields but also to the fact that their presence, position or space distribution, is easily detectable by using magnetic sensors.

In this Thesis an innovative approach to the development of complex devices made by multiple sensing parts together with actuators, and an integrated micro-fluidic system are considered.

The basic concept here is the use of new materials, called ferrofluids or magnetic fluids, made by a suspension of magnetic nanoparticles in a carrier fluid; several different devices have been developed and are shown here in order to demonstrate the possibility to use ferrofluids as a core material to realize both the actuating section of a fluidic system and the sensing.

The devices realized have been developed as laboratory prototypes and as proofs of concept of the ideas that have been first conceived, and then mathematical and numerical modeled prior to be designed as experimental devices.

Due to the intrinsic magnetic nature of the ferrofluids, a briefly introduction on basic concepts about magnetism is discussed in Chapter 1. A classification of materials in nature according to their magnetic behavior is reported, together with some details about the two fundamental source of magnetism: permanent magnets and electromagnets. Finally the main typologies of magnetic sensors commercially available are discussed.

In Chapter 2 the magnetic fluids are presented, together with their applications both in the market and in the research world. The main forces acting on a ferrofluid mass are discussed and modeled.

In Chapter 3 the attention is focused toward sensors realized during this Ph.D. research activity: a gyroscope, a displacement/acceleration sensor, a flow sensor and an inclinometer are dis-

cussed, together with their physical model and with the experimental characterization.

In Chapter 4 research results on ferrofluids when used in actuators are presented. Plungers, valves and a position control system for ferrofluids drop in water have been developed. Two devices are presented: a pump in which a ferrofluid mass is controlled by an array of electromagnets, and a path tracking system, in which a mass is moved along a pre-defined path by a matrix of electromagnets.

The implementation toward integrated device is nowadays of paramount importance in the development of novel systems and transducers. The devices presented here has been developed as laboratory prototype and their scaling toward microsystems is straightforward and has been also addressed during this Ph.D. activity. In Chapter 5 two examples of integrated system in which ferrofluids can be used both in the fluidic part and in the sensing devices are presented. The former structure is a system that can be used for biological measures; in this case ferrofluid is used both in the fluidic part implementing valves and plunger, and as magnetic label for biological entities. The latter one represents a multi-sensorial systems, in which ferrofluids are used in order to implement valves and also as inertial mass of the sensors integrated in the structure.



# Chapter 1

## *THE MAGNETISM*

### **1.1. Magnetism in matter**

An electron moving around his nucleus constitutes a tiny current loop (because it is a moving charge), having in this way a magnetic moment associated with the orbital motion.

All substances contain electrons, but not all substances are magnetic, because in most substances the magnetic moment of one electron in an atom is canceled by that of another electron orbiting in the opposite direction. The net result is that, for most materials, the magnetic effect produced by the orbital motion of the electrons is either zero or very small.

In addition to its orbital magnetic moment, the spin of the electron contributes to its magnetic moment. The magnitude of the angular mo-

mentum associated with spin is of the same order of magnitude as the angular momentum due to the orbital motion. In non-magnetic atoms, for each electron spinning in one direction, there is another electron spinning in the opposite direction. The atom is said to be in a state of magnetic balance and the total spin magnetic moments is zero. A state of magnetic unbalance exists when there are more electrons spinning in one direction than the opposite direction.

The magnetic properties of an atom increase in direct proportion to the number of electrons that are not compensated. The total magnetic moment of an atom is the vector sum of the orbital and spin magnetic moments.

The nucleus of an atom also has a magnetic moment associated with its constituent protons and neutrons. However, the magnetic moment of a proton or neutron is much smaller than that of an electron (due to their much greater mass) and can usually be neglected.

The magnetic state of a substance is described by the magnetization  $\mathbf{M}$ . The magnitude of this vector is defined as the magnetic moment per unit volume of the substance. The total magnetic field  $\mathbf{B}$  at a point within a substance depends both on the applied (external) field and on the magnetization of the substance, in according with the following equation:

$$\mathbf{B} = \mathbf{B}_0 + \mu_0 \mathbf{M} \quad (1.1)$$

where  $\mu_0 \mathbf{M}$  is the field produced by the magnetic substance,  $\mathbf{B}_0$  is the applied magnetic field and  $\mu_0$  is the permeability of the free space ( $4\pi \cdot 10^{-7}$  H/m).



Introducing the magnetic field strength  $\mathbf{H}$ , the previous equation can be expressed as:

$$\mathbf{B} = \mu_0(\mathbf{H} + \mathbf{M}) \quad (1.2)$$

## 1.2. Classification of magnetic materials

Substances can be classified in three categories depending on their magnetic properties. Paramagnetic and ferromagnetic materials are those made of atoms that have permanent magnetic moments. Diamagnetic materials are those made of atoms that do not have permanent magnetic moments [1], [2].

For paramagnetic and diamagnetic substances, the magnetization vector  $\mathbf{M}$  is proportional to the magnetic field strength  $\mathbf{H}$ . For these substances placed in an external magnetic field, it can be written:

$$\mathbf{M} = \chi\mathbf{H} \quad (1.3)$$

where  $\chi$  is a dimensionless factor called the *magnetic susceptibility*. For paramagnetic substances,  $\chi$  is positive and  $\mathbf{M}$  is in the same direction as  $\mathbf{H}$ . For diamagnetic substances,  $\chi$  is negative and  $\mathbf{M}$  is opposite to  $\mathbf{H}$ . Substituting Equation 1.3 into Equation 1.2 the following relationship is obtained:

$$\mathbf{B} = \mu_m\mathbf{H} \quad (1.4)$$

where the constant  $\mu_m$  is called the *magnetic permeability of the substance* and is related to the susceptibility by:

$$\mu_m = \mu_0(1 + \chi) \quad (1.5)$$

Substances may be classified in terms of how their magnetic permeability  $\mu_m$  compares with  $\mu_0$  as follows:

$$\text{Paramagnetic} \quad \mu_m > \mu_0$$

$$\text{Diamagnetic} \quad \mu_m < \mu_0$$

Because  $\chi$  is very small for paramagnetic and diamagnetic substances  $\mu_m$  is nearly equal to  $\mu_0$  for these substances. For ferromagnetic substances, however,  $\mu_m$  is typically several thousand times greater than  $\mu_0$ .  $\mathbf{M}$  is not a linear function of  $\mathbf{H}$  for ferromagnetic substances. This is because the value of  $\mu_m$  is not only a characteristic of the ferromagnetic substance but also depends on the previous state of the substance and on the process underwent when it moved from its previous state to its present one.

### *Ferromagnetism*

A small number of crystalline substances in which the atoms have permanent magnetic moments exhibit strong magnetic effects called ferromagnetism.

These substances contain atomic magnetic moments that tend to align parallel to each other even in a weak external magnetic field. Once the moments are aligned, the substance remains magnetized after the external field is removed. This permanent alignment is due to a strong coupling between neighboring moments.

All ferromagnetic materials are made up of microscopic regions called domains, regions within which all magnetic moments are aligned. In an unmagnetized sample, the domains are randomly oriented so that the net magnetic moment is zero, as shown in Figure 1-1a. When the

sample is placed in an external magnetic field, the magnetic moments of the atoms tend to align with the field, which results in a magnetized sample, as in Figure 1-1b.

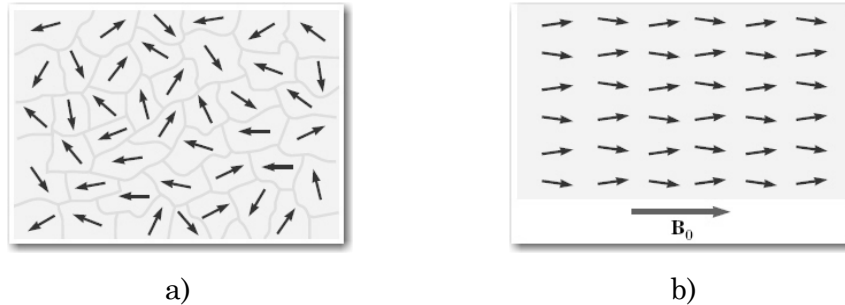


Figure 1-1 a) Random orientation of atomic magnetic moments in an unmagnetized substance. b) When an external field  $B_0$  is applied, the atomic magnetic moments tend to align with the field, giving the sample a net magnetization vector  $M$ .

When the external field is removed, the sample may retain a net magnetization in the direction of the original field. At ordinary temperatures, thermal agitation is not sufficient to disrupt this preferred orientation of magnetic moments.

The described dipole ordering usually does not extend over the entire volume of a sample. Rather, a sample of magnetic material is split up into domains in which all dipoles are ordered along a preferential direction (see Figure 1-2). This direction changes from domain to domain, and it is for this reason that bulk magnetic materials may be unmagnetized, even though they are magnetized on the length scale of the domains.

In an external magnetic field, the magnetization directions of the domains are forced to align with the field, or domains with favorable magnetization direction will grow at the cost of domains with unfavorable directions. Both mechanisms increase the net magnetization of the bulk material. At infinite magnetic field strength, all dipoles are aligned with the field, and the system has reached its saturation magnetization.

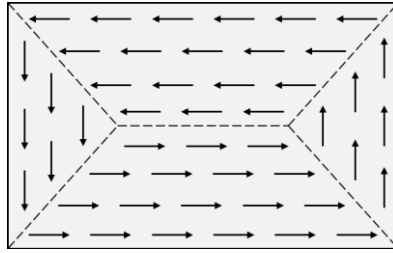


Figure 1-2 In bulk ferromagnetic materials dipole alignment is split up into domains.

After the field is removed, the magnetization tends to relax into its original state with randomly oriented domains. However, in order to reach that equilibrium state, the system may have to pass unfavorable states that can keep it from actually reaching equilibrium. Materials for which the relaxation to the unmagnetized state is prevented, are called “*hard*” magnetic, as opposed to “*soft*” magnetic materials, which demagnetize quickly upon removal of the external field or application of a small field opposing the magnetization.

The magnetic properties of ferroelectric materials can be described by plotting a hysteresis loop for the magnetization,  $\mathbf{M}$ , of the material as a function of the applied magnetic field,  $\mathbf{B}$ . Its shape and size depend on

the properties of the ferromagnetic substance and on the strength of the maximum applied field.

The hysteresis loop for *hard* ferromagnetic materials is characterized by a large remanent magnetization. *Soft* ferromagnetic materials have a very narrow hysteresis loop and a small remanent magnetization, as shown in Figure 1-3.

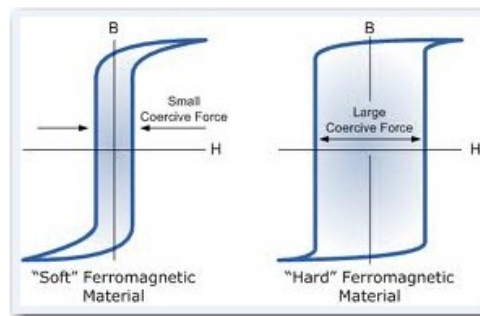


Figure 1-3 Magnetic hysteresis loops for Soft and Hard materials

By heating the material above a critical temperature (the Curie temperature), the thermal agitation is great enough to cause a random orientation of the moments: the substance loses its ferromagnetic properties and becomes paramagnetic.

### *Paramagnetism*

Paramagnetic substances have a small but positive magnetic susceptibility resulting from the presence of atoms (or ions) that have permanent magnetic moments. These moments interact only weakly with each other and are randomly oriented in the absence of an external magnetic field.

When a paramagnetic substance is placed in an external magnetic field, its atomic moments tend to line up with the field. However, this alignment process must compete with thermal motion, which tends to randomize the magnetic moment orientations. The magnetization of a paramagnetic substance is proportional to the applied magnetic field and inversely proportional to the absolute temperature, as expressed in the Equation 1.6:

$$M = C \frac{B_0}{T} \quad (1.6)$$

This relationship is known as Curie's law and the constant  $C$  is called *Curie's constant*;  $T$  is the absolute temperature measured in *Kelvin*.

### *Diamagnetism*

When an external magnetic field is applied to a diamagnetic substance, a weak magnetic moment is induced in the direction opposite the applied field. This causes diamagnetic substances to be weakly repelled by a magnet.

Although diamagnetism is present in all matter, its effects are much smaller than those of paramagnetism or ferromagnetism, and are evident only when those other effects do not exist.

### *Antiferromagnetism*

In materials that exhibit antiferromagnetism, the magnetic moments of atoms or molecules align in a regular pattern with neighboring spins pointing in opposite directions. This spontaneous antiparallel coupling of atomic magnets may exist at sufficiently low temperatures: in fact, it

is disrupted by heating and disappears entirely above a certain temperature, called the Néel temperature, characteristic of each antiferromagnetic material. Some antiferromagnetic materials have Néel temperatures at, or even several hundred degrees above, the room temperature, but usually these temperatures are lower. Above the Néel temperature, the material is typically paramagnetic.

Antiferromagnetic solids exhibit special behaviour in an applied magnetic field depending upon the temperature. At very low temperatures, the solid exhibits no response to the external field, because the antiparallel ordering of atomic magnets is rigidly maintained. At higher temperatures, some atoms break free of the orderly arrangement and align with the external field. This alignment and the weak magnetism it produces in the solid reach their peak at the Néel temperature. Above this temperature, thermal agitation progressively prevents alignment of the atoms with the magnetic field, so that the weak magnetism produced in the solid by the alignment of its atoms continuously decreases as temperature is increased.

#### *Ferrimagnetism*

The ferrimagnetism is a type of magnetism in which the magnetic moments of neighboring ions tend to align nonparallel, usually antiparallel, to each other, as in the antiferromagnetic materials; but unlike the antiferromagnetic, in the ferromagnetic substances the moments are of different magnitudes, so there is an appreciable resultant magnetization.

The materials are less magnetic than ferromagnets. Ferrimagnetic materials are like ferromagnets in that they hold a spontaneous magne-

tization below the Curie temperature, and show no magnetic order (are paramagnetic) above this temperature, but the spontaneous alignment is restored upon cooling below the Curie point. However, there is sometimes a temperature below the Curie temperature at which the number of ions aligned parallel is equal to the number of ions aligned antiparallel, resulting in a net magnetic moment of zero; this is called the *magnetization compensation point*.

Ferrimagnetism occurs mainly in magnetic oxides known as ferrites.

In Figure 1-4 schematic pictures of the magnetic moments behavior in the different kind of materials above described, are reported.

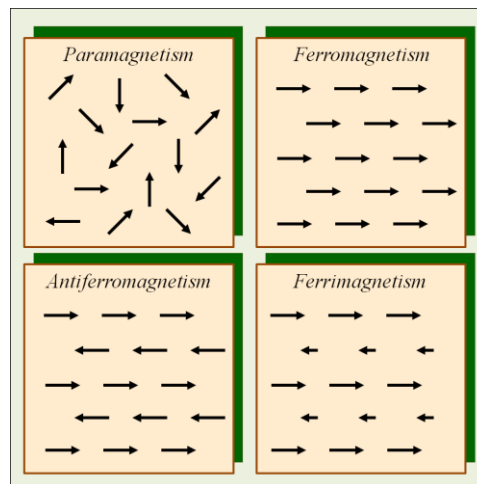


Figure 1-4 Types of magnetism: paramagnetism, ferromagnetism, antiferromagnetism and ferrimagnetism.

In Table 1-1 magnetic response of various materials is compared with their susceptibility and permeability values.



Table 1-1 Comparison between different kind of magnetic materials as function of permeability and susceptibility

|                              | <i>Diamagnetism</i> | <i>Paramagnetism</i> | <i>Ferro-<br/>Ferrimagnetism</i> |
|------------------------------|---------------------|----------------------|----------------------------------|
| <i>Susceptibility</i>        | $<0$                | $\geq 0$             | $\gg 0$                          |
| <i>Relative permeability</i> | $<1$                | $\geq 1$             | $\gg 1$                          |

### 1.3. Sources of magnetic field

A magnetic field can be arisen from two sources:

- Electric currents or more generally, moving electric charges create magnetic fields. Electromagnets exploit such a physical principle.
- Hard ferromagnetic materials can be magnetized by a strong magnetic field, becoming themselves sources of magnetic field.

Permanent magnets or electromagnets can produce the same magnetic field.

#### *Electromagnets*

An electric current flowing in a wire creates a magnetic field around the wire, as expressed by the Biot-Savart law, reported in Equation 1.7.

$$\mathbf{B} = \int \frac{\mu_0 I d\mathbf{l} \times \hat{\mathbf{r}}}{4\pi |r|^2} \quad (1.7)$$

where  $I$  is the current,  $d\mathbf{l}$  is a vector, whose magnitude is the length of the differential element of the wire, and whose direction is the direction of conventional current, and  $\hat{\mathbf{r}}$  is the displacement unit vector in the

direction pointing from the wire element towards the point at which the field is being computed.

To concentrate the magnetic field, the electromagnet wire is wound into a coil, with many turns of wire lying side by side. The magnetic field of all the turns of wire passes through the center of the coil, creating a strong magnetic field there.

Much stronger magnetic fields can be produced if a "core" of ferromagnetic material, such as soft iron, is placed inside the coil. The ferromagnetic core increases the magnetic field to thousands of times the strength of the field of the coil alone, due to the high magnetic permeability  $\mu$  of the ferromagnetic material.

The main advantage of an electromagnet over a permanent magnet is that the magnetic field can be rapidly manipulated over a wide range by controlling the amount of electric current. The poles of an electromagnet can even be reversed by reversing the flow of electricity. However, a continuous supply of electrical energy is required to maintain the field.

The magnetic field produced by an electromagnet driven with a current  $I$  can be expressed as:

$$B_x(x) = \frac{\mu_0 \mu_r n I}{2L} \left[ \frac{\frac{L}{2} - x}{\sqrt{\left(x - \frac{L}{2}\right)^2 + R^2}} + \frac{\frac{L}{2} + x}{\sqrt{\left(x + \frac{L}{2}\right)^2 + R^2}} \right] \quad (1.8)$$

where  $n$  is the turn number,  $L$  is the length of the electromagnet and  $R$  is the radius of the electromagnet.

The qualitative magnetic field behavior is shown in Figure 1-5: the maximum value is at the electromagnet center ( $x = 0$ ).

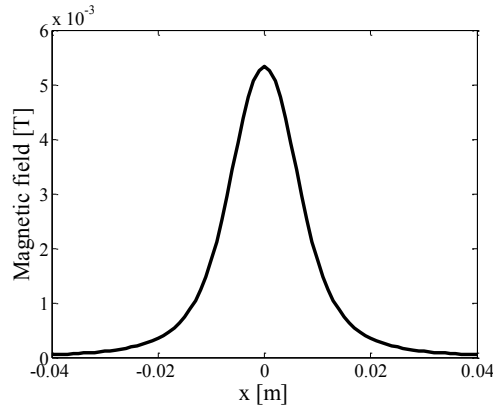


Figure 1-5 Behavior of the magnetic field produced by an electromagnet centered in  $x = 0$  m with a radius  $R = 0.008$  m.

### *Permanent magnets*

A permanent magnet is an object made of ferromagnetic material that is magnetized in one direction by a very strong field and that creates its own persistent magnetic field; due to the ferromagnetic properties of the used material, a magnet doesn't relax back to zero magnetization when the imposed magnetizing field is removed. To demagnetize the magnet it has to be put inside a strong field in the opposite direction of that one used to magnetize it.

A good permanent magnet should produce an high magnetic field with a low mass, and should be stable against the influences which would demagnetize it.

Permanent magnets have several advantages over conventional electromagnets. The fundamental advantage is that they can provide a

relatively strong magnetic field over an extended spatial region for an indefinite period of time with no expenditure of energy.

Another advantage of permanent magnets is that they can be fabricated with a wide range of structural properties, geometric shapes, and magnetization patterns.

Permanent magnets have an additional advantage over electromagnets in that their performance scales well with size. Specifically, if we change a linear dimensions  $L$  of an electromagnet, while keeping the field strength at all the rescaled observation points fixed, the current density must be adjusted by a factor of  $1/L$ . By comparison, if we change the linear dimensions of a permanent magnet, the field strength at all the rescaled observation points remains constant (assuming the magnetization is constant).

Thus, there will be a dimension below which a permanent magnet will be the only viable field source.

The magnetic field produced by a cylindrical magnet of magnetization  $M$  can be expressed as:

$$B_x(x) = \frac{\mu_0 M}{2} \left[ \frac{x+L}{\sqrt{(x+L)^2 + R^2}} - \frac{x}{\sqrt{x^2 + R^2}} \right] \quad (1.9)$$

where  $L$  is the length of the magnet and  $R$  is the radius of the magnet. Equation 1.9 is valid only for  $x > 0$ .

The qualitative magnetic field behavior is shown in Figure 1-6.

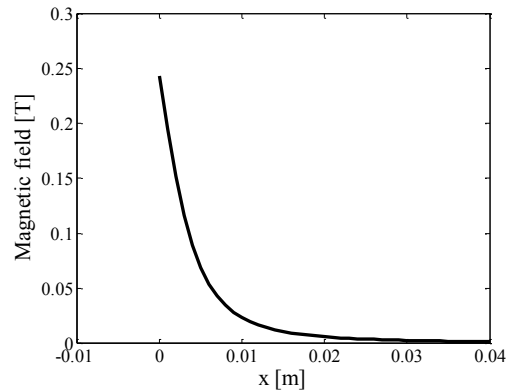


Figure 1-6 Behavior of the magnetic field produced by a permanent magnet centered in  $x = 0$  m and with a radius  $R = 0.005$  m.

#### 1.4. Magnetic sensors

The term *magnetic sensor* refers to various kinds of sensor based to different working principles and used to sense different physical entities.

However, all the magnetic sensors are based on a response to a magnetic quantity: such a response can be directly or indirectly related to the quantity to measure.

Magnetic field sensors are used to measure the amplitude of a magnetic field acting in the area surrounding the device or a field perturbation due to the presence of some magnetic materials. Their output is directly connected with the magnetic field amplitude to detect.

If the target to detect is the amount of a magnetic material, sensors of magnetic materials can be utilized; the amplitude of an external applied magnetic field is modified by the magnetic material, and the change depends on the material amount. The output of this kind of de-

vices is directly connected with the amount of magnetic material to detect.

The third class of sensors exploits the relationship between an external magnetic field or a magnetic force and a physical internal entity of the sensor; the target is not a magnetic quantity, but it is related with it; in this way, the output can be indirectly obtained through this relationship.

### *Magnetic field sensors*

Magnetic field strength is measured using a variety of different technologies. Each technique has unique properties that make it more suitable for particular applications. These applications can range from simply sensing the presence or change in the field to the precise measurements of a magnetic field's scalar and vector properties.

Magnetic field sensors can be divided into vector component and scalar magnitude types. The vector types can be further divided into sensors that are used to measure low fields (<1 mT) and high fields (>1 mT). Instruments that measure low fields are commonly called magnetometers. High-field instruments are usually called gaussmeters. A schematization of the different kind of sensor is reported in Figure 1-7.

The induction coil and fluxgate magnetometers are the most widely used vector measuring instruments. They are rugged, reliable, and relatively less expensive than the other low-field vector measuring instruments.

The fiber optic magnetometer is the most recently developed low-field instrument. Although it currently has about the same sensitivity as a fluxgate magnetometer, its potential for better performance is

large. The optical fiber magnetometer has not yet left the laboratory, but work on making it more rugged and field worthy is under way.

The superconducting quantum interference device (SQUID) magnetometers are the most sensitive of all magnetic field measuring instruments. These sensors operate at temperatures near absolute zero and require special thermal control systems. This makes the SQUID based magnetometer more expensive, less rugged, and less reliable.

The Hall effect device is the oldest and most common high-field vector sensor used in gaussmeters. It is especially useful for measuring extremely high fields ( $>1$  T).

The magnetoresistive sensors cover the middle ground between the low- and high-field sensors. Anisotropic magnetoresistors (AMR) are currently being used in many applications, including magnetometers.

The recent discovery of the giant magnetoresistive (GMR) effect, with its tenfold improvement in sensitivity, promises to be a good competitor for the traditional fluxgate magnetometer in medium-sensitivity applications.

The proton (nuclear) precession magnetometer is the most popular instrument for measuring the scalar magnetic field strength. Its major applications are in geological exploration and aerial mapping of the geomagnetic field. Since its operating principle is based on fundamental atomic constants, it is also used as the primary standard for calibrating magnetometers. The proton precession magnetometer has a very low sampling rate, on the order of 1 to 3 samples per second, so it cannot measure fast changes in the magnetic field.

The optically pumped magnetometer operates at a higher sampling rate and is capable of higher sensitivities than the proton precession magnetometer, but it is more expensive and not as rugged and reliable.

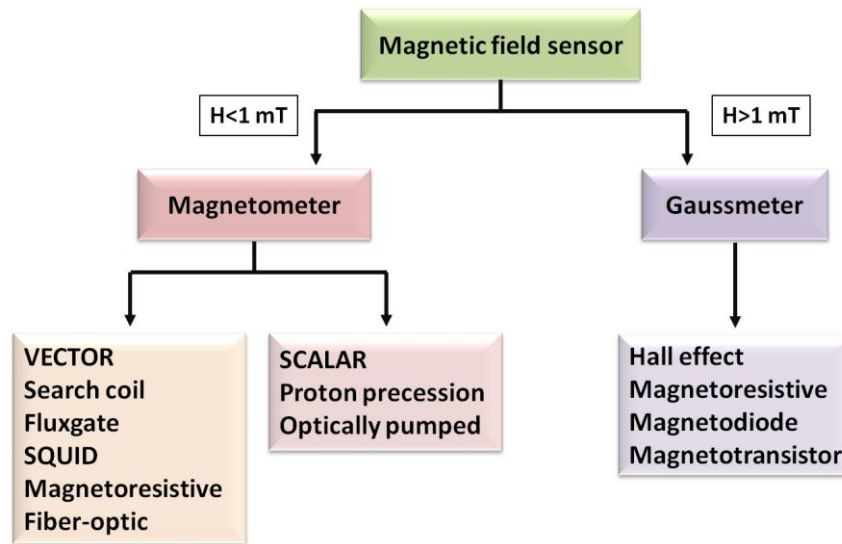


Figure 1-7 Magnetic field sensors are divided into two categories based on their field strengths and measurement range: magnetometers measure low fields and gaussmeters measure high fields.

### *Sensors of magnetic quantities*

Magnetic fields are typically conceptualized with so-called “*flux lines*” or “*lines of force*.” When such flux lines encounter a magnetic material, an interaction takes place and consequently the number of flux lines is either increased or decreased. The original magnetic field density therefore becomes amplified or diminished as a result of the interaction.



The amount of the magnetic field change depends on the quantity of the magnetic material placed in the area in which the magnetic field is acting. Measuring the magnetic field change it is possible to obtain the magnetic material amount; this kind of sensors allows to detect also the presence of a single bead of a magnetic material, for example, if the dimension of the active part of the sensor is comparable with the dimension of the bead.

Usually superparamagnetic beads are used due to their property to not retain a magnetization imposed through an external magnetic field when the field is removed.

Several kinds of sensor were developed and used to sense an amount of magnetic beads. Usually they are based on a differential configuration: the sensor compares the output due only to the field with the output due to the field increased by the beads. The sensor output is then related with the beads quantity.

#### *Sensors exploiting magnetic forces as working principle*

This class of sensors is based on a relationship between the magnetic force (or the magnetic field) and the entity to detect; the output of the sensor is then indirectly related with the target entity. The most common sensor is the LVDT (Linear Variable Differential Transformer).

It is based on the variation in mutual inductance between a primary winding and each of two secondary windings when a ferromagnetic core moves along its inside, dragged by a nonferromagnetic rod linked to the moving part to sense. When the primary winding is supplied by an ac voltage, in the center position the voltages induced in each secondary winding are equal and the output voltage is zero because it is differen-

tial. When the core moves from that position, one of the two secondary voltages increases and the other decreases of the same amount, and the output is different from zero. The secondary coil voltage changes with the position of the core because the core modifies the field produced by the primary winding; such a modification changes the auto inductance value of the secondary coil, that it is reported on the output voltage. Such a sensor exploits the relationship between the magnetic core and the output voltage in order to detect the core position. The output then is indirectly related with the target represents by the core position.

# Chapter 2

## *FERROFLUIDS AND THEIR APPLICATIONS*

### **2.1. Ferrofluids**

Ferrofluids (also called magnetic fluids or magnetic nanofluids) are a special category of nanomaterials which exhibit simultaneously liquid and superparamagnetic properties.

Due to the fact that no natural liquids offer these features, the starting point of the field of magnetic fluid research can be found in a work of Resler and Rosensweig [3]. Such a work showed that a liquid material with controllable magnetic properties can be used in many development possibilities. After that, strong efforts have been undertaken to synthesize a system enabling the mentioned magnetic control. Suspensions of magnetic nanoparticles in appropriate carrier liquids are a sufficient realization of such a new class of smart materials. Although

non-stable suspensions have been produced much earlier, the first stable synthesis of a ferrofluid was reported in the pioneering work by Pappell [4], in 1965. The development of these suspensions – called ferrofluids – proved the high potential of the new research field.

In the past 40 years since the first synthesis of a ferrofluid has been reported, a large number of technical applications was realized. Reviewing the proposed applications it can be noticed that those which have been successful on the market are characterized by two basic traits. The first one consists in the use of the magnetic field only to exert a force in order to fix the mass position. The second one is that all technical applications were realized mainly in the field of mechanical engineering.

Today the perspectives of ferrofluid research are much broader. The force enters directly into the Navier–Stokes equation and can thus be utilized to control and drive flows in the fluid, not only to provide a force positioning the ferrofluid. Taking into account that strength and direction of magnetic fields and field gradients can be tailored for a specific need, one can imagine the variety of arising possibilities. Furthermore not only the flow of magnetic suspensions can be changed by magnetic fields but also their thermophysical properties –in particular the rheological behavior– change significantly in the presence of magnetic fields. In fact, modifying the magnetic field intensity, is possible to change parameters as density and viscosity.

Modern ferrofluids are colloidal magnetic fluids. A colloid is a suspension of finely divided nanoparticles [5], such as  $\text{Fe}_3\text{O}_4$ ,  $\gamma\text{-Fe}_2\text{O}_3$ ,  $\text{CoFe}_2\text{O}_4$ , Co, Fe or Fe-C, in a continuous medium. They are composed by small particles of solids, magnetic, single-domain particles coated with a molecular layer and a dispersant (surfactant), and suspended in

a liquid carrier. The colloidal ferrofluid must be synthesized, because it is not found in nature. The three primary constituents of these magnetic liquids are:

- The liquid carrier in which the particles are suspended. Ferrofluids can be water- or oil-based [6].
- The suspended superparamagnetic particles are made from materials such as iron oxide, and have a diameter of the order of 10-20 nm. The small size is necessary to maintain stability of the colloidal suspension; particles significantly larger than this would precipitate.
- The surfactant coats the ferrofluid particles to help maintain the consistency of the colloidal suspension. The surfactant prevents interactions and agglomeration of particles caused by Van der Waals forces [7].

A scheme of ferrofluid particles is reported in Figure 2-1.

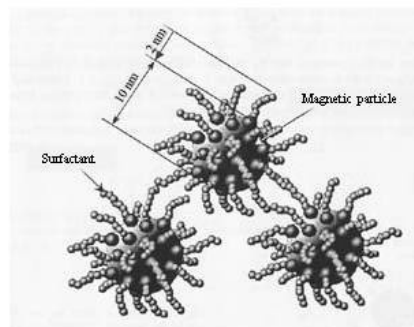


Figure 2-1 Schematic of ferrofluid particles, with highlighted the magnetic core and the surfactant.

The particles are sufficiently small so that the ferrofluid retains its liquid characteristics even in the presence of a magnetic field, and substantial magnetic forces can be induced which results in fluid motion. The magnetic liquid can then be considered as an ultrafine particle system with interparticle spacing large enough to approximate the particles as non-interacting.

The size of the particles makes the difference between the two types of fluids which depend on the applied magnetic field: ferrofluids and magneto-rheological fluids. Magneto-rheological fluids are stable suspensions of magnetically polarisable micron-sized particles suspended in a carrier fluid. These fluids vary their viscosity with the applied magnetic field and can solidify in the presence of a sufficient magnetic field. In comparison, ferrofluids retain liquid flowability even in the most intense applied magnetic fields. Ferrofluids are usually described as magnetically soft material, which means that the magnetism vector follows the applied field without hysteresis, and a small applied field is required to produce saturation. Instead an high magnetization strength implies high magnetic pressure exerted by the fluid. The latter property is strategic for the implementation of transducers adopting ferrofluids as functional or inertial masses. Ferrofluids present a high magnetization saturation ranges from 200 to 900 G, approximately with no remanence and, as a liquid, they can be easily moved through microchannels, and perfectly adapt to any geometry.

When a ferrofluid mass is subjected to an external magnetic field, hits flat surface could become unstable and shows a behavior called *Rosensweig effect*. At a certain intensity of the field, peaks appear at the fluid surface, which typically form a static hexagonal pattern at the fi-

nal stage of the pattern forming process. Such a typical response is shown in Figure 2-2.

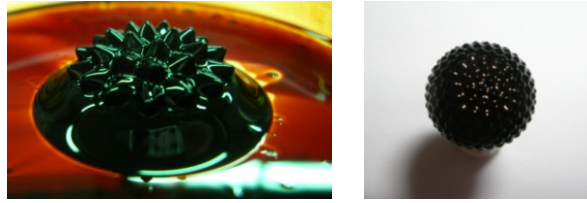


Figure 2-2 Examples of ferrofluids subjected to magnetic fields.

Magnetic fluids show also interesting patterns, coming from ferrohydrodynamic instabilities, such as lines, labyrinths and various structures which could be exploited to produce actuation. In [8] authors impose, on a magnetic fluid preliminarily separated into concentrated and dilute phases, an alternating electric field of opportune amplitude and frequency, and a superimposed orthogonal constant magnetic field. The imposed field causes the formation of a labyrinth structure, as reported in Figure 2-3.

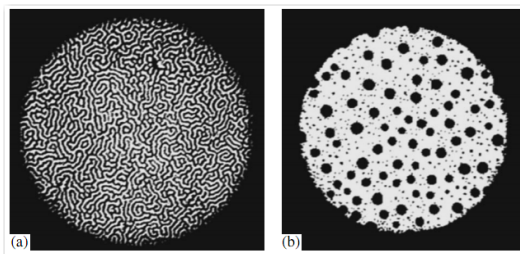


Figure 2-3 Structural lattices formed in a thin layer of the magnetic fluid exposed to an alternating electric field at different frequencies: a) 2 *kHz* and b) 10 *kHz*.

A magnetic field applied to a ferrofluid volume exerts a magnetic force which causes the alignment of the ferrofluid particles in the direction of the field. In the absence of external magnetic field the ferrofluid maintains its liquid status while under the magnetization produced by a strong magnetic field the ferrofluid modifies its physical properties, as viscosity and density, and moves to a more compliant position.

## **2.2. Applications of ferrofluids**

Fluids which can be controlled and manipulated by external magnetic fields of moderate strength are a challenging subject for scientists interested in fluid movement or in application engineering.

When the magnetic influence exerted by an external magnetic field becomes strong enough to compete with gravitational forces, it is possible a complete control of the magnetic fluid mass movement and of its physical properties.

The possibility of using different types of coils (controlling and switching electronically the current) and permanent magnets allows for a wide range of magnetic field intensity, so the technical application of such a materials is very large and various.

The research field of magnetic fluids is a multi-disciplinary area: chemists study their synthesis and produce the ferrofluids, physicists study their physical properties and propose theories which explain them, engineers study their applicability and use them in technological products, biologists and physicians study their biomedical possibilities and use them in medicine and in research on the biological area.



With modern advances in understanding nanoscale systems, current research focuses on synthesis, characterization, and functionalization of nanoparticles with magnetic and surface properties tailored for application as micro-nanoelectromechanical sensors, actuators, in micro-nanofluidic devices, as nanobiosensors, and in biomedical applications.

#### *Commercial applications of ferrofluids*

Ferrofluids allow applications in each of its constituent disciplines of chemistry, fluid mechanics, and magnetism. An important property of concentrate ferrofluids is that they are strongly attracted by permanent magnets, while their liquid nature is preserved. The attraction can be strong enough to overcome the gravity force. Many commercial applications of ferrofluids are based on this properties. Sealing for several industrial processes, loudspeakers, inertial dampers, angular position sensors, computer disk drives are examples of applications where this kind of materials has been widely adopted [9],[10].

For example, in hard disks they are used to form liquid seals around the spinning drive shafts. The rotating shaft is surrounded by magnets. A small amount of ferrofluid, placed in the gap between the magnet and the shaft, will be held in place by its attraction to the magnet. The fluid of magnetic particles forms a barrier which prevents debris from entering the interior of the hard drive.

In loudspeakers ferrofluids are used to remove heat from the voice coil, and to passively damp the movement of the cone. They reside in what would normally be the air gap around the voice coil, held in place by the speaker's magnet. Since ferrofluids are paramagnetic, they obey

Curie's law, thus become less magnetic at higher temperatures. A strong magnet placed near the voice coil (which produces heat) will attract cold ferrofluid more than hot ferrofluid thus forcing the heated ferrofluid away from the electric voice coil and toward a heat sink.

### *Biomedical applications of ferrofluids*

Ferrofluids are nowadays assuming a fundamental role in biomedical applications for diagnostic and therapy [11]. These materials find interesting applications in magnetic bio-assay tasks, such as magnetic separation, drug delivery, hyperthermia treatments, magnetic resonance imaging (MRI) and magnetic labelling. In fact, due to the different and controllable sizes of their particles (from few nanometers up to micrometers), they can interact with the biological entity of interest like a cell (10–100  $\mu\text{m}$ ), a virus (20–450 nm), a protein (5–50 nm) or a gene (2 nm wide and 10–100 nm long), thus offering attractive possibilities to develop efficient solutions in the bio-medical field. Examples of such techniques can be found in [12], [13], [14].

Magnetic particles coated with biocompatible molecules act as markers to identify bio-entities. The main advantage of this form of labelling as compared to other techniques is related to the simple mechanisms to identify, to localize and to transport magnetic labelled entities. Actually, all these mechanisms are based on the use of magnetic fields which are also intrinsically penetrable into human tissue. Magnetic labelling is used for both entities localization and separation.

Magnetic separation is a two-step process: the first step consists in labelling the molecules to be detected with magnetic beads; this is obtained by coating the magnetic particle surface with specific biocom-

patible molecules to allow the binding with the target entity. The second step consists in separating the labelled molecules from their native by blocking the magnetic particles via a magnetic field. The same principle is used to remove unwanted biomaterials from a fluid, capturing the magnetic particles with a magnet or with a magnetic field gradient and letting flow the remaining fluid.

A promising use of magnetic fluid in biomedicine is drug delivery which has peculiar advantages as compared to traditional techniques. In fact, today therapeutic drugs act on the entire body (e.g. by attacking both tumour tissue and healthy ones) while with selective drug delivery only specific locations of the body are attacked. This approach allows to reduce the required drug dosage, to increase drugs specificity as well as prolonging the use of these effective agents. The magnetic particles bounded with the drugs are injected through the circulatory system while an external high-gradient magnetic field is used to deliver tasks.

Another possibility for tissues (e.g. cancer) treatments is the hyperthermia. Such technique consists of embedding magnetic particles into the target tissue and applying a suitable magnetic field to cause particles heating. This heat radiates into the surrounding tumour tissue thus to destroy, after a specific length of time, the cancer cells. While other hyperthermia methods produces unacceptable heating of human healthy tissue, magnetic hyperthermia overcome these drawbacks by a selective heating of target cells.

MRI is a non-invasive technique that allows the characterization of morphology and physiology in vivo through the use of magnetic scanning. The human body is mainly composed of water molecules containing protons which under powerful magnetic field align with the direc-

tion of the field. A second radio frequency electromagnetic field is then briefly turned on causing the protons to absorb some of its energy. When this field is turned off the protons release this energy at a radio frequency which can be detected by a scanner. Relaxation times of protons in diseased tissue, such as tumours, are different than in healthy tissue and this information is used for the sake of inspection. Magnetic nanoparticles can be conveniently used in MRI techniques as contrast agent.

#### *Transducers based on the use of ferrofluids*

Practical interest in magnetic fluids derives from the possibility to implement valuable and efficient conversion of elastic energy into mechanical energy [15].

The use of magnetic fluids in transducers is now widely diffused due to valuable properties of these fluids compared to traditional materials [16]. Actually, fast response, shock resistance and their intrinsic feature to be shapeless allow to develop suitable sensors and actuators.

The idea of using ferrofluids as the active mass in inertial sensors offers the opportunity to control the device specifications by manipulating the ferrofluid core properties (such as viscosity, volume, etc.) via electric signals. Moreover, the absence of mechanical moving parts and solid-inertial masses provide high reliability and robustness against mechanical shocks.

Actually in case of traditional inertial sensors exploiting a solid mass a mechanical shock could compromise the device functionality while the use of ferrofluid allows for recovering the system functionality by re-aggregation.

Usually, in ferrofluid devices, the electric part is intrinsically isolated from the liquid medium: this gives the possibility to maintain the same circuitry (that is the more expensive part in a ferrofluid system) and change or modify the rest of the device. The latter is strategic in contexts requiring the replacement of the beaker (e.g. due to the use of invasive media or contaminants).

Various examples of devices exploiting non-conventional materials such as ferrofluids to implement sensors and transducers are available in the literature.

The possibility to use these materials in combination with Micro-Electro-Mechanical-Systems (MEMS) to develop efficient sensors and actuators [17] is pushing the interest of the scientific community toward the development of new and efficient magnetic fluids and specific coatings. Miniaturized permanent magnets, ferromagnetic patterned layers, and integrated coils are traditionally implemented in MEMS technology. Anyway, such realizations host small volumes of magnetic material which can provide a negligible magnetic force which is unsuitable for actuation purposes. The use of MEMS cavity filled with ferrofluids could be a valuable solution to obtain high volumes of magnetic material of appropriate density.

Several examples of sensors using a ferrofluid mass are available in literature. In particular, a cantilever beam dip in magnetic fluid has been proposed to change the operative range of the device simply exploiting external magnetic field actions on the ferrofluid [18]; the device uses a feedback compensation scheme and a capacitive readout strategy.

Another example is represented by an inductive tilt sensor composed of a cylindrical container housing a mobile magnetic core clamped

to two permanent magnets [19]. Magnetic liquid coats the permanent magnet so to create a cushion, which allows for the core sliding consequently to a device tilt. The repulsion force between the supporting magnets and two magnets disposed outside the container imposes an equilibrium position at the core when the device is tilted. Two coils are used to detect the position of the magnetic core.

In [20] a magnetometer using a ferrofluid fluxgate sensor is used to measure the intensity of a dc magnetic field by using a second harmonic principle. A cylindrical ferrofluid sample is subjected to the simultaneous action of a circular field produced by an axial alternating current and a dc field parallel to the cylinder axis. The induced electromotive force is detected by a cylindrical coil surrounding the sample, and it depends on the target magnetic field.

In [21] authors have developed a temperature sensor using a ferrofluid thin film. When a magnetic field parallel to the plane of the ferrofluid is applied, magnetic chains form in the same direction of the magnetic field, which results in the suppressing of optical transmission; this behavior depends on the room temperature.

Concerning the implementation of actuation systems, the possibility to easily drive ferrofluids through micro-channels of various geometry represents a convenient solution. Nanogenerators and nanomotors, micropipettes, alternating micropumps and valves, rotating micropumps and electromagnetic micropumps are examples of ferrofluid integrated transducers.

In [22] a micropipette exploiting the magnetic force generated by external electromagnets is proposed. The mechanism implemented allows to suck and release fluid through the same gate, because inlet and

outlet tanks have been implemented on the same side of the micropipette. To perform the pumping operation external magnets moved by a DC motor are used; moreover, an interesting solution is proposed to realize the valve by exploiting a dedicated geometry of the channel.

A rotating micropump implementing fluid sampling through two ferrofluid cup is discussed in [23]. In this case caps are created and managed by two permanent magnets actuated through a DC motor.

In [24] a pump handling magnetic particles is described. The device exploits an array of electromagnets to move a volume of magnetic nanoparticles from an inner tank to a destination tank.

The behaviour of ferrofluid in a travelling wave magnetic field has been experienced and can be suitably exploited for actuation purposes [25]. Below a critical magnetic field strength the fluid moves in the opposite direction of the travelling wave while above the critical field the ferrofluid moves in the same direction. Quantities affecting the critical magnetic field are frequency of the magnetic field, concentration of the magnetic particles, and the fluid viscosity.

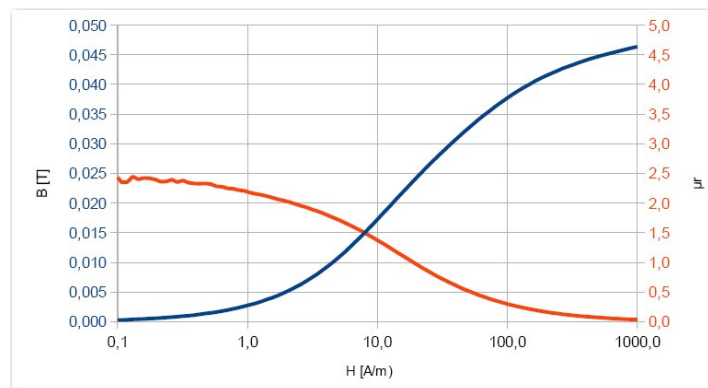
### 2.3. EFH1 Ferrofluid by Ferrotec

Several kind of ferrofluids are today commercially available. The ferrofluid used in the realization and characterization of the devices presented in this work is the EFH1 of Ferrotec.

Table 2-1 summarizes the main physical properties of the EFH1 ferrofluid, while in Figure 2-4 the relationship between  $B$  and  $H$  and between  $\mu_r$  and  $H$  are reported.

Table 2-1 Physical properties of the EFH1 ferrofluid.

|  |  |
|--|--|
| <i>Carrier liquid</i>                  | <i>Light mineral oil</i>                 |
| <i>Saturation Magnetization</i>        | <i>44 mT</i>                             |
| <i>Viscosity @ 27°C</i>                | <i>6 mPas</i>                            |
| <i>Nominal Particle Diameter</i>       | <i>10 nm</i>                             |
| <i>Density</i>                         | <i>1.21 g/ml (1210 Kg/m<sup>3</sup>)</i> |
| <i>Magnetic Particle Concentration</i> | <i>7.9% by Volume</i>                    |
| <i>Flash Point</i>                     | <i>92 °C</i>                             |
| <i>Pour point</i>                      | <i>-94 °C</i>                            |
| <i>Surface Tension</i>                 | <i>29 mN/m</i>                           |
| <i>Volatility (1 h @ 50 °C)</i>        | <i>9 %</i>                               |

Figure 2-4  $B$  vs  $H$ , and  $\mu_r$  vs  $H$  for EFH1 ferrofluid.

#### 2.4. Main forces acting on a ferrofluid mass

In this section the main forces acting on a ferrofluid mass, and that play a significant role in the modeling and realization of the developed



transducers shown in this work, are investigated. The relative equations will be recalled and utilized in the next two chapters.

– Gravitational force

Due to the magnetic field of the Earth, all objects are subject to the gravitational force, and then also a ferrofluid mass; the force exerted on a ferrofluid mass can be expressed as:

$$\mathbf{F}_g = m_f \mathbf{g} = \rho_f V_f \mathbf{g} \quad (2.1)$$

where  $\mathbf{g}$  is the gravitational acceleration,  $m_f$  is the ferrofluid mass,  $\rho_f$  is the ferrofluid density and  $V_f$  is the ferrofluid volume.

– Archimedes force

When an object is put in a liquid, the fluid exerts a force that opposes the object's weight. The manner in which buoyant force acts is summarized by Archimedes's principle, which states that the magnitude of the buoyant force always equals the weight of the fluid displaced by the object. The force exerted on a ferrofluid mass placed inside a liquid is expressed as:

$$\mathbf{F}_a = V_f \rho_l \mathbf{g} \quad (2.2)$$

where  $\mathbf{g}$  is the gravitational acceleration,  $V_f$  is the ferrofluid volume and  $\rho_l$  is the density of the liquid in which the ferrofluid mass is immersed.

– Magnetic force

A source of magnetic field exerts a force on the surrounding magnetic objects, expressed as:

$$\mathbf{F}_m = -\nabla U = (\mathbf{B} \cdot \nabla) \mathbf{m} + (\mathbf{m} \cdot \nabla) \mathbf{B} \quad (2.3)$$

where  $U$  is the magnetic potential energy,  $\mathbf{m}$  is the magnetic moment of dipole and  $\mathbf{B}$  is the magnetic flux density.

When  $\mathbf{B}$  is high enough to saturate  $\mathbf{m}$ , the previous expression becomes:

$$\mathbf{F}_m = (\mathbf{m} \cdot \nabla)\mathbf{B} \quad (2.4)$$

The magnetic force acting on the ferrofluid volume, making explicit the magnetic dipole, can be expressed as:

$$\mathbf{F}_m = V_f \chi_f (\mathbf{H} \cdot \nabla)\mathbf{B} = \frac{V_f \chi_f \mathbf{B}_x}{\mu_0} \partial \mathbf{B}_x \quad (2.5)$$

where  $\chi_f$  is the magnetic susceptibility of the ferrofluid,  $\mathbf{H}$  is the applied magnetic field and  $\mathbf{B}_x$  is the component of the magnetic flux density along the axis of the displacement.

The qualitative magnetic force behavior, produced by the magnetic field shown in Figure 1-5, is reported in Figure 2-5. The point of equilibrium is in  $x = 0$ , that corresponds to the electromagnet center and to the maximum value of the field. In fact, when  $x < 0$  the force is positive and tends to move the mass along the positive  $x$  axis, towards the point zero, where the force is null; when  $x > 0$ , the force is negative and tends to move the mass along the negative  $x$  axis, also in this case towards the point zero.

For small displacements, the magnetic force is linear, as it is visible in Figure 2-5; in such a case, it is reasonable to assess that the magnetic force along the sensing axis acts on the ferrofluid mass as an equivalent spring, whose properties can be controlled by modulating the driving magnetic field amplitude. In this case the magnetic force can be expressed as:

$$F_m = -k(x - x_0) \tag{2.6}$$

where  $k$  is the equivalent elastic constant and  $x_0$  is the equilibrium position of the ferrofluid volume. This force acts as a retaining force which contrasts external perturbations on the device (and consequently on the ferrofluid volume) and governs the movement of the inertial mass around its equilibrium position.

The elastic constant  $k$  can be approximated with [16]:

$$k = \omega_n^2 \rho_f V_f \tag{2.7}$$

where  $\omega_n^2$  is the natural frequency of the system.

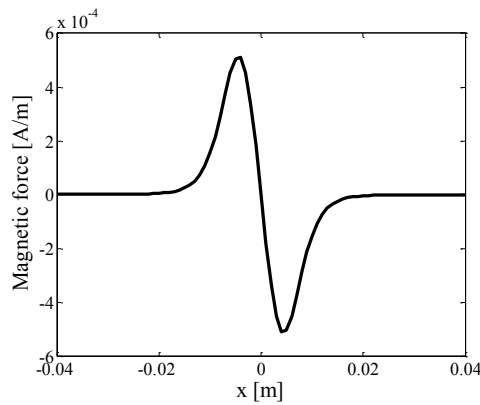


Figure 2-5 Qualitative behavior of the magnetic force produced by an electro-magnet.

– Hydrodynamic force

When an object moves inside a fluid, it is subjected to the hydrodynamic force.

If a ferrofluid mass is placed into a fluid not in movement, such a force can be expressed as:

$$\mathbf{F}_h = 6\pi\eta r_f \dot{\mathbf{x}}_f \quad (2.8)$$

where  $\eta$  is the ferrofluid viscosity,  $\dot{\mathbf{x}}_f$  is the acceleration of the ferrofluid mass inside the fluid, and  $r_f$  is the radius of an equivalent sphere modeling the ferrofluid volume, given from the following equation:

$$r_f = \left(\frac{3V_f}{4\pi}\right)^{1/3} \quad (2.9)$$

When also the fluid is in movement, in the Equation 2.8 a new term has to be added:

$$\mathbf{F}_h = 6\pi\eta r_f \left(\frac{\mathbf{Q}}{S} - \dot{\mathbf{x}}\right) \quad (2.10)$$

where  $\mathbf{Q}$  is the flow rate and  $S$  is the section of the pipe in which the fluid flows.

# Chapter 3

## *SENSORS BASED ON FERROFLUIDS*

Scientists are today oriented in the research of innovative materials and innovative sensing strategies in order to realize devices with high performances. In fact, sensor parameters such as sensitivity, resolution, operative range, robustness depend on physical, electrical and mechanical characteristic of the device. In this sense new materials and advanced topologies are largely inspected.

In this chapter sensors developed are presented.

According to the use of innovative materials in order to improve the sensor performances, realized devices exploit the use of a ferrofluid mass as inertial mass. This choice is due to the opportunity to control the device specifications by manipulating the ferrofluid mass properties (such as viscosity, volume, etc.) via permanent magnets or electromag-

nets. In fact, modifying the magnetic field produced by magnets or electromagnets it is possible to change the device specification, as operative range, sensitivity and resolution.

Moreover, the possibility to easily re-aggregate a ferrofluid mass after an occurred mechanical shock and the absence of mechanical moving parts and solid-inertial masses provide high reliability and robustness against shock.

The proposed sensor architectures demonstrate as a complete control of a ferrofluid mass and then of a sensor parameters is possible; this constitutes a concrete premise for integrated implementation of such class of transducers.

In this section developed sensors are reported, together with a description of their working principle, the model, the demomacroprototype realization and the characterization.

### **3.1. A ferrofluid Gyroscope**

In this section a developed ferrofluid gyroscope is presented, together with theoretical analysis aimed to model its behaviour; details on the readout methodology and the experimental results are reported. Moreover, the optimal operating regime of the device and its performances are also considered. This gyroscope is a good example of how it is possible to control the position of a ferrofluid mass used as inertial mass of the device.

The decoupling of the electric tools (the driving and the readout systems) from the beaker housing the ferrofluid mass confers interesting features to the device such as isolation between the electric tools and

the liquid media, the re-usability of the electric tools while the low cost beaker becomes the disposable part of the system, the possibility to implement such sensing strategy in pre-existing structure filled with a liquid media.

It should be highlighted that bio-medical systems, hydraulic systems, laboratory tests and contexts where non invasive measurement on liquids is required and that should be implemented through disposable devices could represent real application contexts for the proposed methodology.

### *The working principle*

The ferrofluid gyroscope developed is intended to sense an angular rate applied to a beaker housing a drop of ferrofluid acting as the inertial mass of the system [26], [27]. A schematization of the device is given in Figure 3-1.

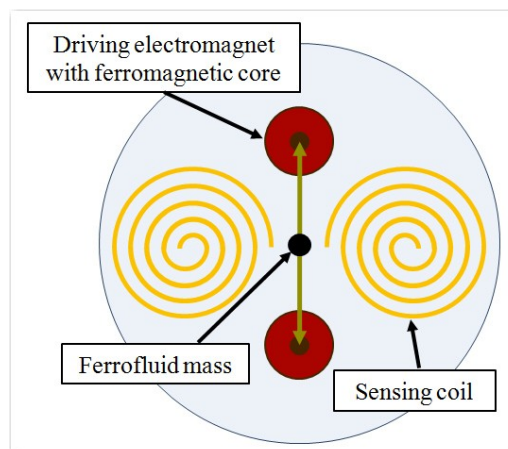


Figure 3-1 Schematization of the ferrofluid gyroscope.

The device consists of a glass plate filled with de-ionized water and a drop of ferrofluid. The magnetic fluid moves between two stable positions corresponding to the location of two electromagnets placed under the beaker. The electromagnets are driven by two sinusoidal currents with a phase shift of  $180^\circ$  each. The aim of the driving architecture is to implement the mechanism moving the ferrofluid volume from one electromagnet to the other.

In the absence of any angular rate applied to the structure, the ferrofluid movement takes place along the driving axis. Moreover, two permanent magnets are placed under the magnetic actuators to implement a retaining mechanism against the Coriolis force. When an angular rate is imposed on the device, the ferrofluid mass experiences a Coriolis force which produces a deformation of the linear trajectory, that becomes elliptical, as shown in Figure 3-2.

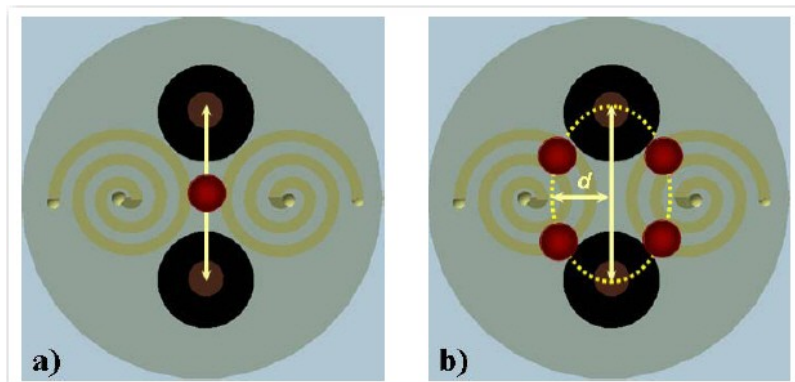


Figure 3-2 Schematic of the motion of the ferrofluid mass a) without angular rate and b) with angular rate. The distance  $d$  depends on the angular rate amplitude acting on the system.



The amplitude of the minor axis of such an ellipse depends on the angular rate: higher is the angular rate value, higher is the axis amplitude.

*The sensing strategy*

In order to sense the deformation from the linear trajectory a differential inductive sensing strategy has been used. The readout electronics consists in two planar coils whose inductance values change with the ferrofluid motion. The planar coils were realized in PCB technology exploiting the FR4 (Flame Retardant 4) process.

Actually, when an angular rate is forced on the device, the elliptical trajectory of the ferrofluid volume is perturbed producing an alteration of the magnetic coupling with the sensing coils. Figure 3-3 shows a schematization of the electronics controlling the driving electromagnets while Figure 3-4 shows the readout electronic processing signals coming from the sensing system.

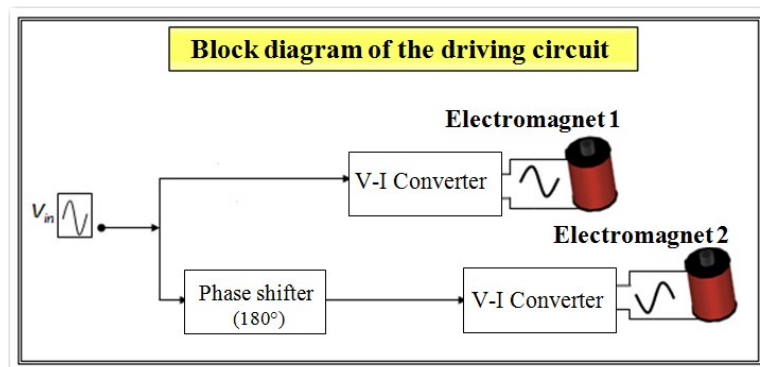


Figure 3-3 Block diagram of the driving electronics.

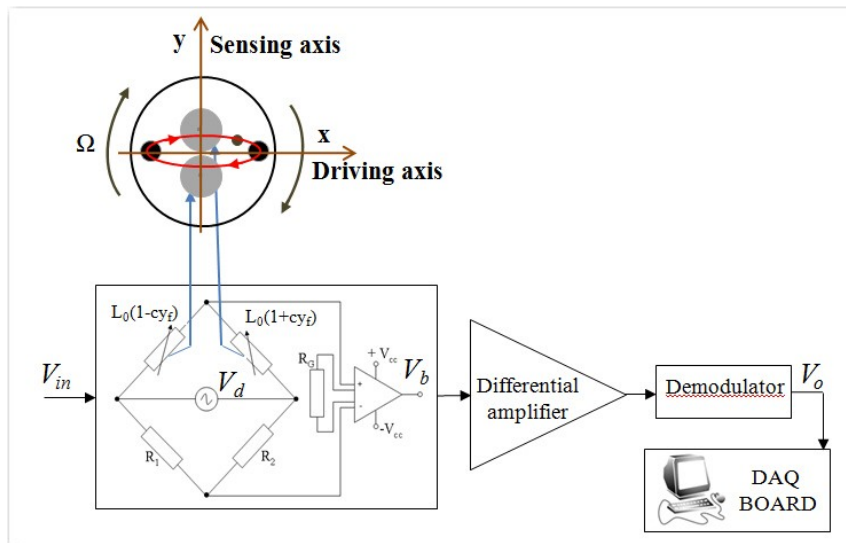


Figure 3-4 Schematics of the readout sensing electronics.

Some details on the implementation of the driving electromagnets and the planar sensing coils are given in Table 3-1.

Table 3-1 Specifications of driving electromagnets and planar coils.

| <b><i>Electromagnets specifications</i></b> |                                 |
|---|---------------------------------|
| <i>Length</i>                               | $28 \cdot 10^{-3} \text{ m}$    |
| <i>Internal diameter</i>                    | $15 \cdot 10^{-3} \text{ m}$    |
| <i>Wire diameter</i>                        | $0.233 \cdot 10^{-3} \text{ m}$ |
| <i>Layers number</i>                        | 21                              |
| <i>Turns number</i>                         | $\sim 2600$                     |
| <i>Resistance</i>                           | 80 $\Omega$                     |

| <b><i>Planar coils specifications</i></b> |                                 |
|---|---------------------------------|
| <i>Wire depth</i>                         | $0.4 \cdot 10^{-3} \text{ m}$   |
| <i>Spacing</i>                            | $0.4 \cdot 10^{-3} \text{ m}$   |
| <i>External diameter</i>                  | $20 \cdot 10^{-3} \text{ m}$    |
| <i>Turns number</i>                       | 12                              |
| <i>Inductance</i>                         | $0.907 \cdot 10^{-6} \text{ H}$ |
| <i>Distance between coils center</i>      | $21 \cdot 10^{-3} \text{ m}$    |

The inductive readout strategy exploits the variation of the planar coils inductance with the ferrofluid motion.

Actually, the interaction between the magnetic fluid and the sensing coils produces a modulation of the output voltage,  $V_b$ , of a bridge configuration followed by an instrumentation amplifier with gain  $G$ .

In the small displacement regime, assuming a linear dependence of the coil inductance value on the ferrofluid mass position

$$L = L_0(1 + cy_f) \quad (3.1)$$

where  $L_0$  is the nominal value of the inductance and  $c$  is a sensor parameter, the relationship between the mass position and the bridge output voltage,  $V_b$ , would be:

$$\frac{V_b}{V_d} = -G \frac{(k+1)(1+cy_f) - 2k}{2(k+1)} \quad (3.2)$$

where  $V_d$  is the bridge driving voltage,  $y_f$  is the position of the ferrofluid in the sensing axis and  $k = R_1/R_2$ .

In the case of  $R_1 = R_2$  Equation 3.2 becomes:

$$\frac{V_b}{V_d} = G \frac{cy_f}{2} \quad (3.3)$$

Obtained experimental results will make it possible to sustain the form (3.1) which would be strategic for the design of the sensing tool.

The bridge electronics is driven by a sinusoidal voltage with an amplitude of 300 mV@100 kHz.

In order to extract the information related to the ferrofluid position along the sensing axis a dedicated conditioning electronics was realized. In particular, a rectifier stadium followed by a 2<sup>nd</sup> order Sallen-Key filter and a further amplifier were used. The output signal  $V_0$  was collected by a DAQ card controlled via a LabVIEW<sup>®</sup> tool by National Instrument.

### *The model*

In the following, considerations leading to the definition of the optimal working conditions especially in terms of the driving signals amplitude and frequency are discussed along with a model of the device behavior.

A set of experiments have been performed to characterize the behavior of the ferrofluid mass subjected to the driving system. In particular, an experimental set-up based on a vision system has been developed to estimate the trajectory of the ferrofluid mass subjected to the electromagnetic driving mechanism. A set of frames has been acquired for different values of the frequency and amplitude of the driving signals.

In order to process the acquired images a dedicated software environment has been developed based on tracking the ferrofluid volumes position along its trajectory. The image processing tool was developed in the LabVIEW<sup>®</sup> environment exploiting features of the IMAQ vision toolbox with particular regards to standard filtering paradigms allowing

particle detection. Figure 3-5 shows a typical frame and the superimposed grid with a resolution of 5mm.

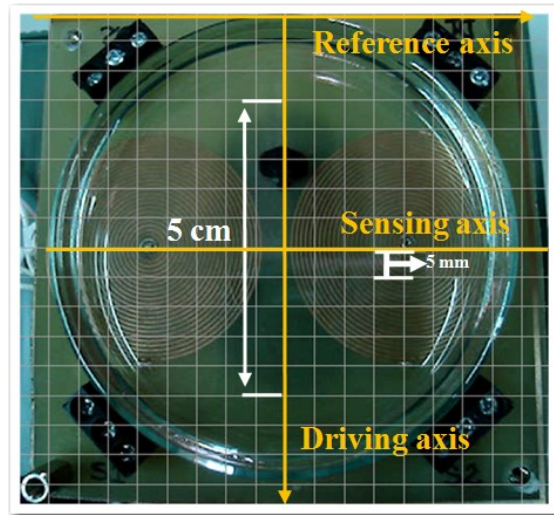


Figure 3-5 A typical frame and the superimposed grid with a resolution of 5 mm.

The reconstruction of the mass trajectory was performed for a set of different tilts of the device in the case of a 0.1ml volume of ferrofluid.

Figure 3-6 shows behaviors of the ferrofluid volume as a function of the driving signal amplitude and frequency for two different tilts of the device. As can be observed, due to the intrinsic properties (e.g. time constant and friction) of the system, the ferrofluid volume is able to follow the imposed dynamics for a well defined range of amplitudes and frequencies of the driving signals.

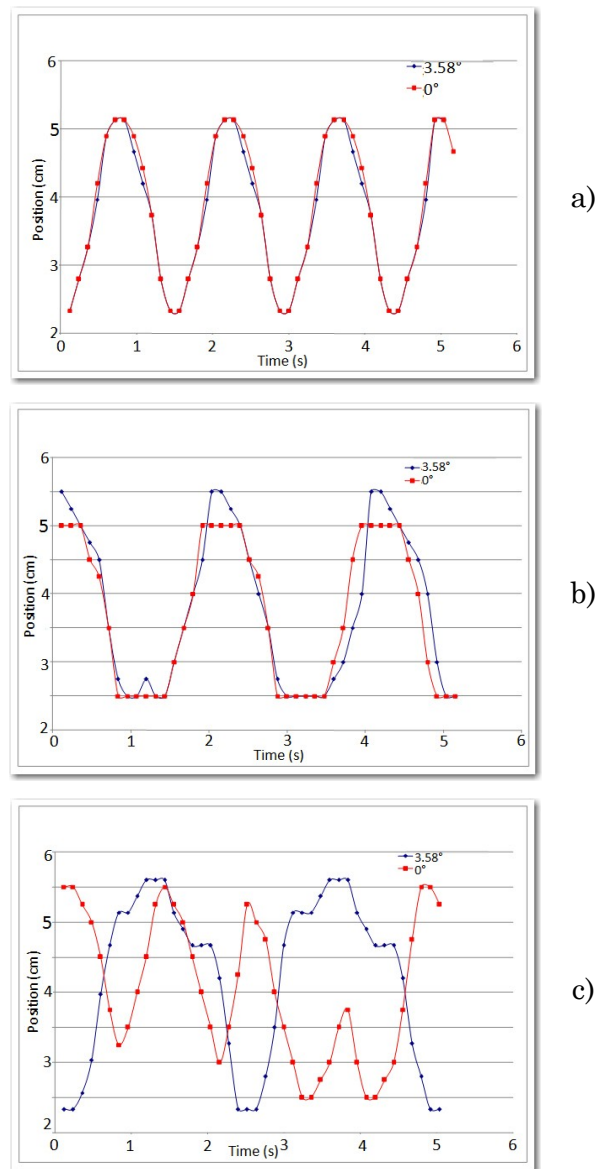


Figure 3-6 Time evolution of the ferrofluid mass ( $0.1 \text{ ml}$ ) position for a driving signal of: a)  $1.4 V_{pp}$  @  $690 \text{ mHz}$ , b)  $1.4 V_{pp}$  @  $500 \text{ mHz}$  c)  $1.4 V_{pp}$  @  $1 \text{ Hz}$ , and for two different tilts. Cases b) and c) are examples where the ferrofluid mass fails to follow the driving signal.

A deep analysis of the ferrofluid mass trajectory as a function of the frequency and amplitude of the driving signal leads to the driving parameters map shown in Figure 3-7. This map highlights the optimal working region for which the mass trajectory follows the driving dynamic.

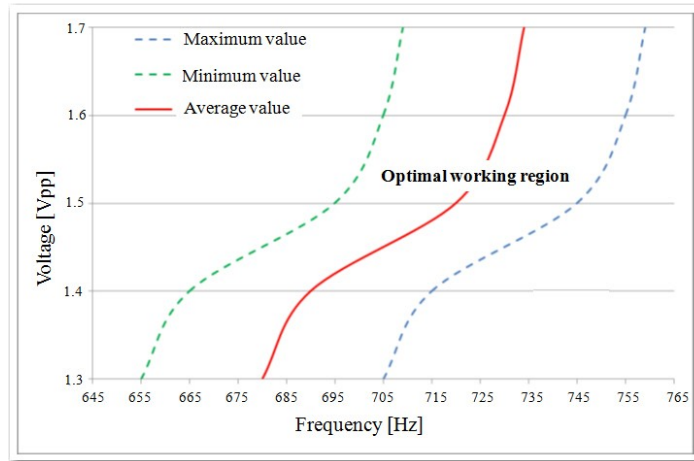


Figure 3-7 Driving parameter map highlighting the optimal working region (tilt=0°).

The effect of the driving mechanism on the ferrofluid behavior can be described by the following model adopting the axis reference system shown in Figure 3-5:

$$\rho_f V_f \ddot{x}_f = -k_x x_f - F_{h,x} + F_m \quad (3.4)$$

subjected to the initial position and velocity:

$$x_f(0) = 0; \quad \dot{x}_f(0) = 0 \quad (3.5)$$

where  $x_f$  is the position of the ferrofluid along the driving axis,  $V_f$  is the ferrofluid volume,  $\rho_f$  is the ferrofluid density,  $F_{h,x}$  is the hydrody-

dynamic drag force along the driving axis and  $k_x$  is the equivalent elastic constant describing the effects of the permanent magnets on the ferrofluid volume along the driving axis.

The magnetic force is expressed as an equivalent spring force because conditions expressed in section 2.4 are verified.

$F_m$  is the magnetic force generated along the driving axis by the electromagnetic system, that can be expressed as:

$$\mathbf{F}_m = V_f \chi_f (\mathbf{H} \cdot \nabla) \mathbf{B} \quad (3.6)$$

In order to fit model (3.4) on the experimental observations presented in Figure 3-6a an expression of the magnetic force (3.6) is required. To such aim an array of Hall sensors SS496A1 by Honeywell, having a declared sensitivity of  $2.5 \cdot 10^{-7} \pm 7.5 \cdot 10^{-9}$  V/T, was positioned along the driving axis.

Figure 3-8 shows the real view of the sensor array while Figure 3-9 shows a schematization of the array and their location as respect to the driving electromagnets.

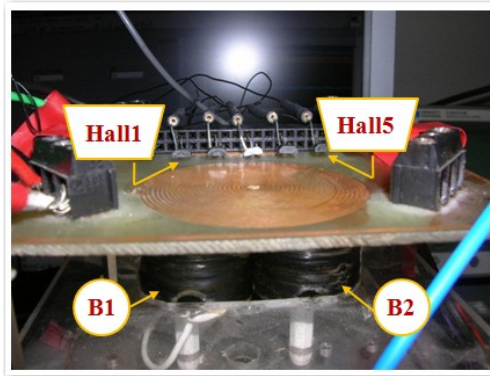


Figure 3-8 Real view of the sensor array used for the estimation of the electromagnets fields.



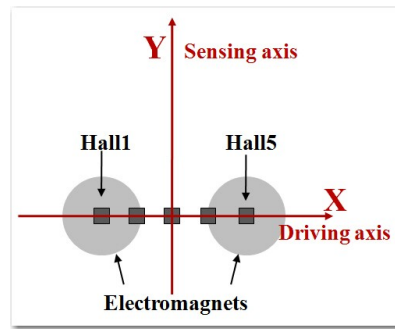


Figure 3-9 Schematization of the sensor array used to measure the generated magnetic fields.

Figure 3-10 shows the spatio-temporal behavior of the magnetic field measured along the driving axis when only one electromagnet is turned on. The same experiments were done activating also the other electromagnet.

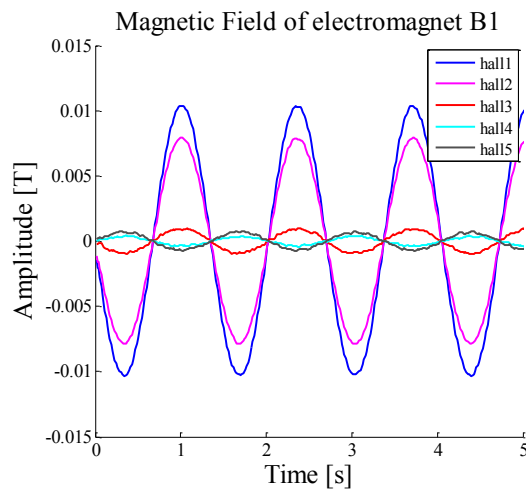


Figure 3-10 Spatio-temporal behavior of the magnetic field measured along the driving axis due to one electromagnet.

By interpolating the spatio-temporal evolution of the two magnetic fields generated by the two electromagnets the following expressions have been obtained:

$$B_1 = 105.3e^{-\left(\frac{x+0.0171}{0.0131}\right)^2} \sin(1.380\pi t) \quad (3.7)$$

$$B_2 = 105.3e^{-\left(\frac{x+0.0171}{0.0131}\right)^2} \sin(1.380\pi t + \pi) \quad (3.8)$$

The total magnetic field is given by:

$$B = B_1 + B_2 \quad (3.9)$$

while the corresponding magnetic force has been obtained through Equation 3.6.

Figure 3-11 shows the time evolution of the magnetic field and the magnetic force along the driving axis.

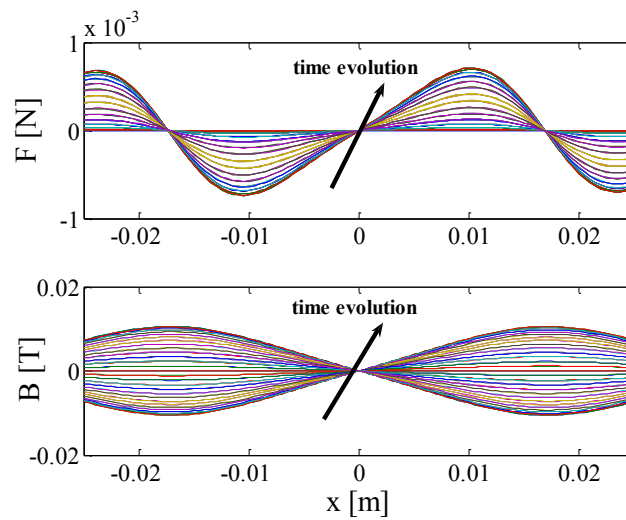


Figure 3-11 Evolution of the magnetic field and the magnetic force along the driving axis.

For the sake of clarity the model input, i.e. the time evolution of the magnetic force, in two different positions along the driving axis (in a generic position and in the position of one electromagnet) is given in Figure 3-12a/b along with the magnetic field and the observed mass position which represents the model output.

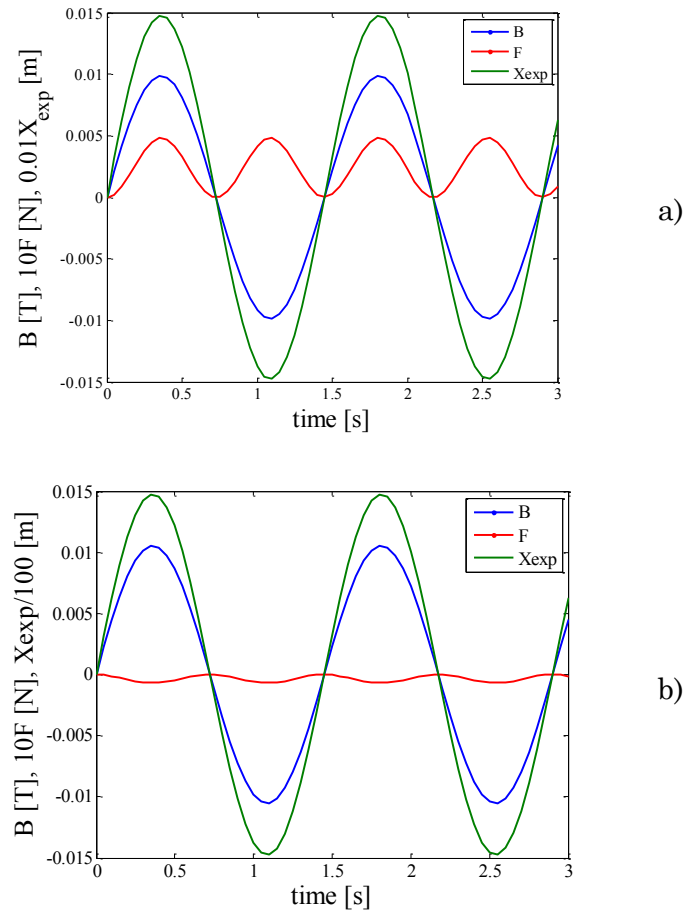


Figure 3-12 Time evolution of the magnetic force, the magnetic field and the ferrofluid mass position a) in a generic point along the driving axis, and b) in the location of one electromagnet.

Figure 3-13 shows the behavior of the magnetic field and the magnetic force along the driving axis for the specific time slot where the magnetic field amplitude reaches its maximum value. It can be observed that the stable position of the ferrofluid mass corresponds to the electromagnets location and as expected are identified by a null magnetic force.

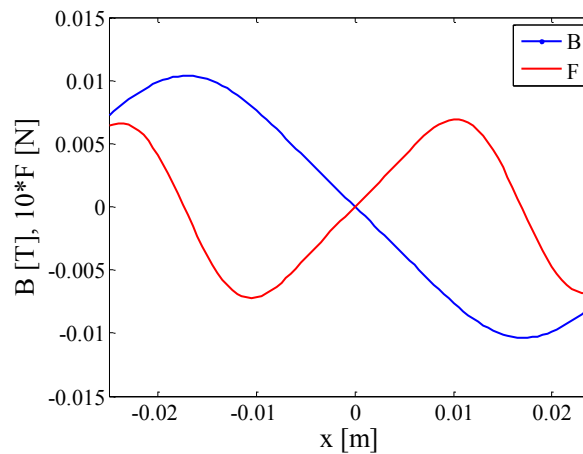


Figure 3-13 Behaviour of the magnetic field and the magnetic force along the driving axis for the specific time slot where the magnetic field amplitude reaches its maximum value (scaling factors given in the vertical axis label have been used for the sake of convenience).

In order to fit model (3.4) on the experimental observations given in Figure 3-6a the Nelder-Mead optimization algorithm has been adopted. The minimization approach is schematized in Figure 3-14 where the need for a routine estimating the magnetic force at each step,  $i$ , of the numerical integration of model (3.4) is evidenced.

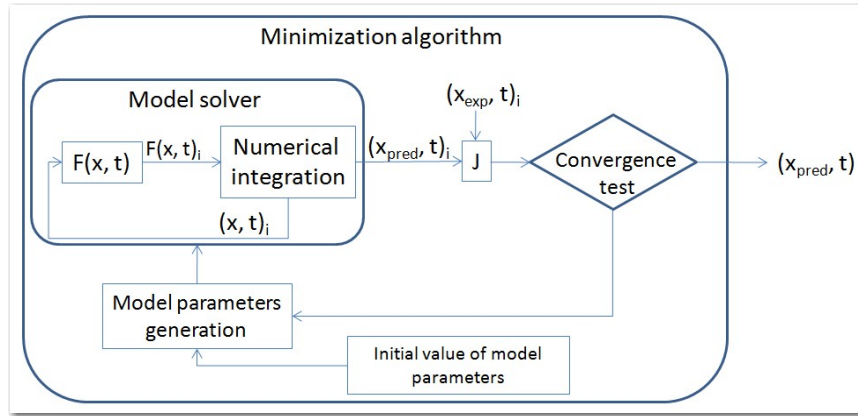


Figure 3-14 Model of the numerical integration adopted.

To minimize the squared difference between the experimental trend of the ferrofluid volume shown in Figure 3-6a,  $x_{exp}$ , and the trend predicted by model (3.4),  $x_{pred}$ , the following root mean square type functional  $J$  was used:

$$J\% = \frac{\sqrt{\sum (x_{pred} - x_{exp})^2}}{\sqrt{\sum (x_{exp})^2}} 100 \quad (3.10)$$

Figure 3-15 shows the comparison between the observed evolution of the ferrofluid mass and the one predicted by model (3.4).

Actually, the following model was used:

$$\begin{cases} a\ddot{x}_{norm,f} = -bx_{norm,f} - c\dot{x}_{norm,f} + dF_m + e \\ x_f = x_{norm,f} \cdot f \end{cases} \quad (3.11)$$

where  $x_{norm,f}$  is the normalized mass position along the driving axis.

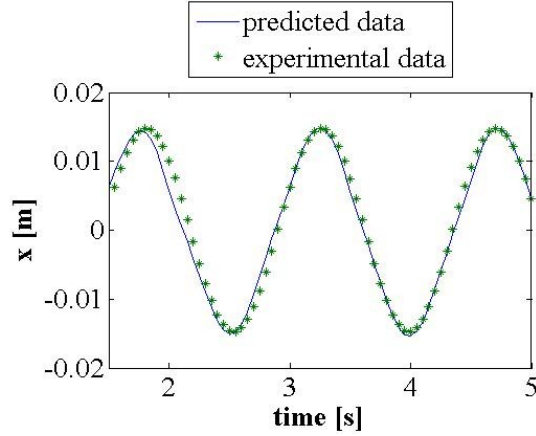


Figure 3-15 Comparison between the experimental and the predicted evolution of the ferrofluid mass.

The above considerations refer to the situation where no angular rate is applied to the gyroscope. In the presence of an angular rate the following model can be used to describe the behavior of the ferrofluid mass:

$$\rho_f V_f \ddot{y}_f = -k_y y_f - F_{h,y} + 2\rho_f V_f \Omega \dot{x} \quad (3.12)$$

Where  $y_f$  is the position of the ferrofluid along the sensing axis,  $F_{h,y}$  is the hydrodynamic drag force along the sensing axis,  $k_y$  is the equivalent elastic constant describing the effects of the permanent magnets on the ferrofluid volume along the sensing axis and  $\Omega$  is the applied angular rate.

The last term in (3.12) is the Coriolis force and it behaves like a forcing term which affects the trajectory component along the  $y$  axis. The amplitude of such perturbation will follow the amplitude of the angular rate  $\Omega$  and will be sensed by the planar coils.

Assuming homogeneous physical interaction along the  $x$  and  $y$  axis between the liquid media and the ferrofluid mass as well as uniform retaining effects of the permanent magnets, the following assumption can be made:

$$k_x = k_y \quad (3.13)$$

Under assumption (3.13) a simulation of the whole system behavior was hence implemented by combining models (3.4) and (3.12).

Simulation results are reported in Figure 3-16 showing the mass trajectory intersection with the  $y$  axis as a function of the angular rate. A linear relationship between these quantities is obtained. This consideration will be useful in the next section to demonstrate the hypothesis (3.1).

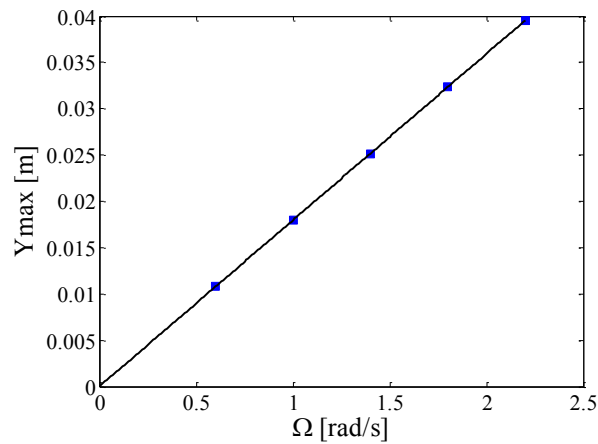


Figure 3-16 Simulation results of the mass trajectory intersections with the  $y$  axis as a function of the imposed angular rate.

*The experimental results*

Figure 3-17 shows the set-up adopted for the device characterization implemented by a step-motor and an high resolution encoder to obtain an independent estimation of the angular rate imposed. Specifications of the ELCIS I/38Z4-2000-5-BZ-H-CVC-R-01 encoder adopted are given in Table 3-2.

Table 3-2 Electrical parameters of encoder.

| <b><i>Encoder specifications</i></b> |                  |
|--------------------------------------|------------------|
| <i>Pulses per round</i>              | <i>1÷2000</i>    |
| <i>Max. frequency</i>                | <i>160 kHz</i>   |
| <i>Output signal</i>                 | <i>Push-pull</i> |
| <i>Voltage supply</i>                | <i>5 Vcc</i>     |

A dedicated software tool has been developed to control the imposed angular rate and to acquire data coming from both the encoder and the sensor readout system.

In order to characterize the device response a set of experimental surveys has been performed. In particular, the device response for different values of the angular rate imposed on the device has been observed. The working conditions of the driving system has been selected on the basis of the analysis illustrated above. In particular, a driving signal of 1.4 Vpp@690 mHz has been used.



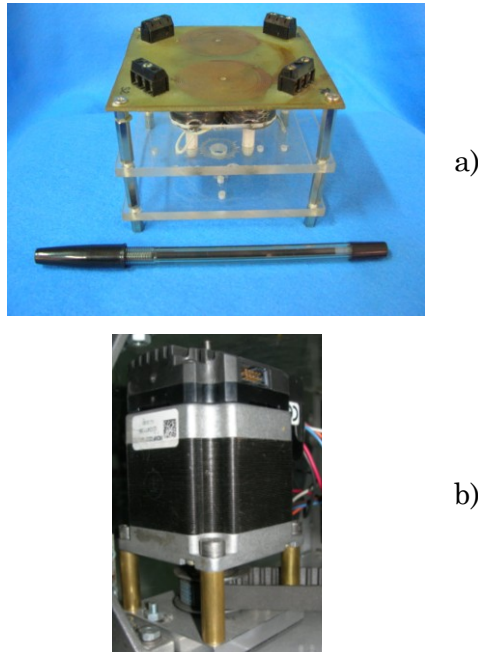


Figure 3-17 Experimental set-up adopted for the device characterization; a) sensing-driving system and b) step motor.

Figure 3-18 shows the behavior of the device as a function of the imposed angular rate, the latter being estimated by the encoder system. The linear trend highlighted by experimental observations in Figure 3-18 along with the expected behavior in Figure 3-16 states for the reliability of hypothesis (3.1). A device sensitivity of 0.12 rad/s has been estimated by observing and processing the output signal fluctuations while other specifications have been reported in Figure 3-18.

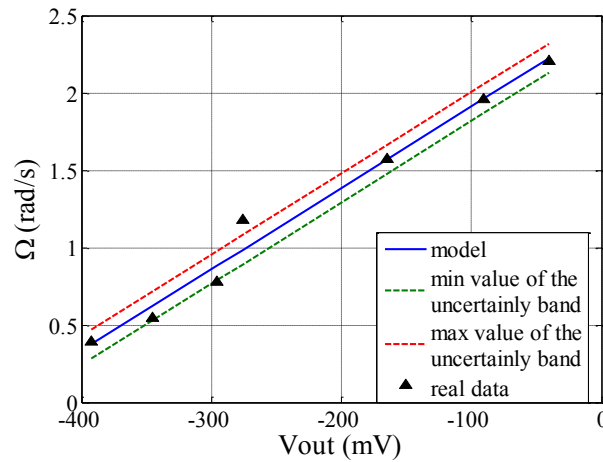


Figure 3-18 Calibration diagram of the ferrofluid gyroscope.

### 3.2. An inertial sensor exploiting a spike shaped ferrofluid

In this section a novel inertial sensor is presented; it can be used as low band accelerometer or as displacement sensor [28], [29].

The device exploits the *Rosensweig effect* to create a spike of ferrofluid inside a beaker filled with de-ionized water. An inertial stimulus applied to the structure produces a movement of the spike free-end. The latter is detected via a suitable low-cost Infra Red (IR) readout strategy. This approach offers the possibility to bypass drawbacks related to the mechanical frictions between the inertial mass and the structure wall which leads to advantages in terms of sensitivity for many applications.

Moreover, the use of a ferrofluid mass as the inertial mass of the transducer confers to the device high robustness against mechanical shocks and reliability. Actually in case of traditional inertial sensors exploiting a solid mass a mechanical shock could compromise the device

functionality while the use of ferrofluid allows for recovering the system functionality by re-aggregation.

A further outcome of the proposed approach is the possibility to implement the sensing strategy in a section of a preexisting structure where the monitoring of inertial quantities acting on a liquid media is required and the use of invasive technology is not admitted. In the case of the considered sensing strategy the idea could be to insert a drop of ferrofluid inside the channel housing the liquid media and to fix its position by an external magnetic force. Successively, the readout strategy can be easily integrated to the structure.

Above the already mentioned advantages, other interesting features arise from the physical decoupling between the sensing readout electronics and the beaker. Actually, the intrinsic isolation between the electric part and the liquid medium, the low cost and disposable housing for the liquid media (consisting of a low cost beaker), the re-usability of the readout system and the adaptability of the proposed sensing strategies to a wide set of real applications (from bio-medical systems to contexts where non invasive measurements on liquids are required) are advantages of such strategy.

In the next sections, theoretical analysis aimed to model its behaviour are reported, together with details on the readout methodology; finally the experimental results are shown and commented.

#### *The working principle*

As it is schematized in Figure 3-19, the sensor is based on a glass structure fixed by a plexiglass support. The beaker is filled with de-ionized

water. A drop of ferrofluid is magnetically fixed to the beaker wall. The fixing mechanism is based on the use of low cost permanent magnets.

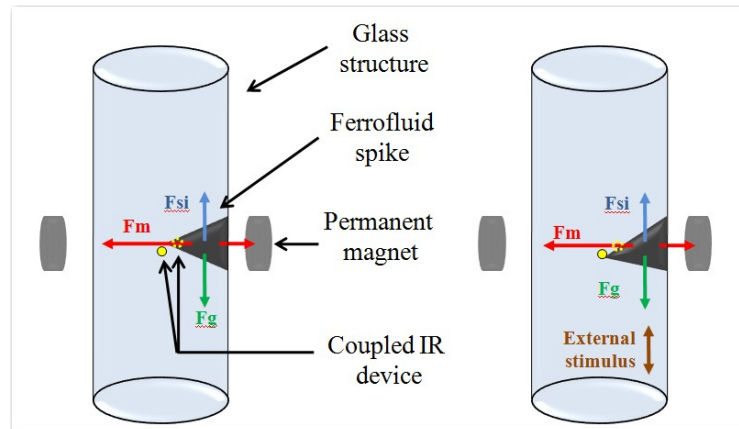


Figure 3-19 Schematization of forces acting on the ferrofluid mass:  $F_m$  is the magnetic force,  $F_g$  is the gravitational force and  $F_{si}$  is the hydrostatic force. On the left hand side the steady state regime is shown; on the right hand side an external stimulus perturbs the system and the free-end of the ferrofluid spike changes its position. The diode used to produce the IR emission is represented with four yellow and symmetrically arranged circular ring segments, while the photodiode is represented with a filled yellow circle.

The action of the magnetic force on the ferrofluid mass is twofold: it fixes the position of the ferrofluid volume on the beaker wall and it resembles an equivalent elastic force which acts to maintain the ferrofluid drop in a compliant position. Changing the force strength (the magnetic field strength) allows to modify the equivalent stiffness of the sensing element and consequently its behaviour to external stimuli in terms of responsivity and operating range.

The chosen configuration of permanent magnets produces a suitable magnetic field which provides a spike shape to the ferrofluid mass. Two oppositely aligned sets of magnets have been used. Magnets positioned on the right hand and on the left hand of the spike are used to fix the position of the ferrofluid mass and to define the desired force strength. Magnets positioned in front of and behind the ferrofluid mass are used to shape the sensing mass.

Although a electric control of magnetic sources would improve the flexibility and the efficiency of the sensing strategy, it must be considered that the use of passive magnetic actuators to implement the retaining/shaping mechanism is a dramatic advantages of the proposed approach in terms of power budget. The latter is a crucial specifications for several applications.

To such aim, sliding mechanisms have been also installed to assure a reasonable flexibility in the magnets position. Actually, the possibility to regulate the distance between magnets allows for defining the spike length (and thickness) and consequently some specifications of the device, such as the operating range and the sensitivity. Main forces ruling the spike behaviour are shown in Figure 3-19.

An external stimulus applied to the system, e.g. an acceleration, is transferred to the ferrofluid mass thus producing perturbation of the free-end around its equilibrium position. In order to convert the free end movement into an electrical output an external sensing strategy was required. Among the several available solutions investigated, including vision systems exploiting advanced image processing solutions, a low cost strategy based on Infra Red (IR) devices has been implemented.

*The sensing strategy*

The choice of using an IR strategy to read the mass position is strictly related to the idea of developing a low-cost system and to focus on solutions easy to be miniaturized.

The coupled IR device (diode and a photodiode) is suitably positioned to detect ferrofluid movements. In the absence of external stimulus the ferrofluid masks the receiving diode from the IR emission. An external stimulus produces the spike free-end movement with a consequent partially unmasking of the IR photodiode. The IR output signal is hence related to the ferrofluid movement and indirectly to the inertial stimulus. This readout strategy is schematized in Figure 3-19 and Figure 3-23b by small circles stating for the coupled IR device.

The sensing methodology is schematized in Figure 3-20. The IR readout strategy is based on the variation of the irradiated area of the IR receiver,  $A_d$ , due to a ferrofluid displacement.

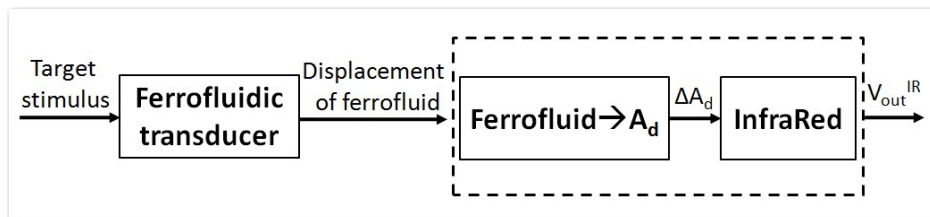


Figure 3-20 Block diagram of the readout strategy. The first block in the left-hand side is the pipette with the spike shaped ferrofluid mass; the second block represents the conversion between the ferrofluid displacement and the irradiated area of the IR device; the last block in the right-hand side represents the IR device. A voltage to current converter was used to drive the IR transmitter, while a standard voltage divider was used to obtain an output voltage from the IR device.

In the following the relationship between the ferrofluid movement and the irradiated area of the IR device will be addressed. As already evidenced, in the absence of external stimuli the ferrofluid spike practically masks the IR receiver thus minimizing the irradiate area.

Figure 3-21 depicts, in an axial symmetry, the contour of the spike free-end (represented by dotted lines) and the contour of the IR receiver area. The tangent line to the IR area corresponds to the null stimulus case where the ferrofluid spike almost covers the IR receiver. In the presence of an external stimulus, the free-end of the ferrofluid spike shifts (see dotted lines) and its displacement increases as the stimulus strength increases.

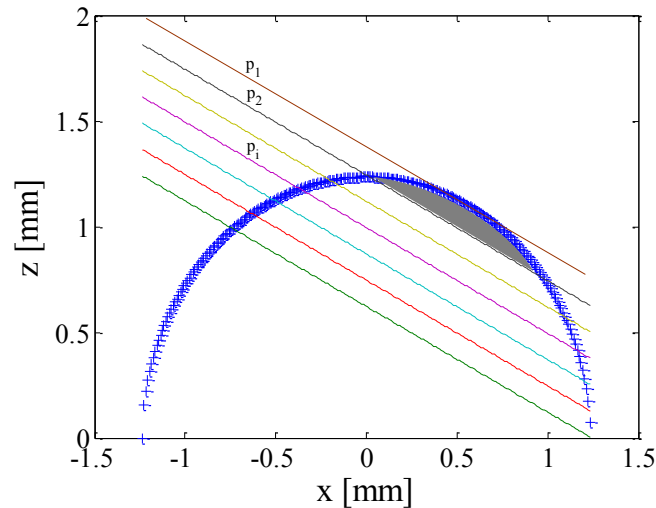


Figure 3-21 Schematization of the interaction between the ferrofluid spike and the IR device.

Simulations have been performed considering a uniform displacement of the ferrofluid (indicated with  $p_i$  in Figure 3-21) and its effect on

the IR receiver in terms of the irradiated area. The definition of irradiated area is evincible from Figure 3-21 by considering the filled area as the irradiated area obtained for the ferrofluid spike position  $p_2$ .

Figure 4 shows the irradiated area as a function of the spike free-end displacement. The estimated trend is well approximated by a linear relationship as evidenced by the linear fitting detailed in the figure captions.

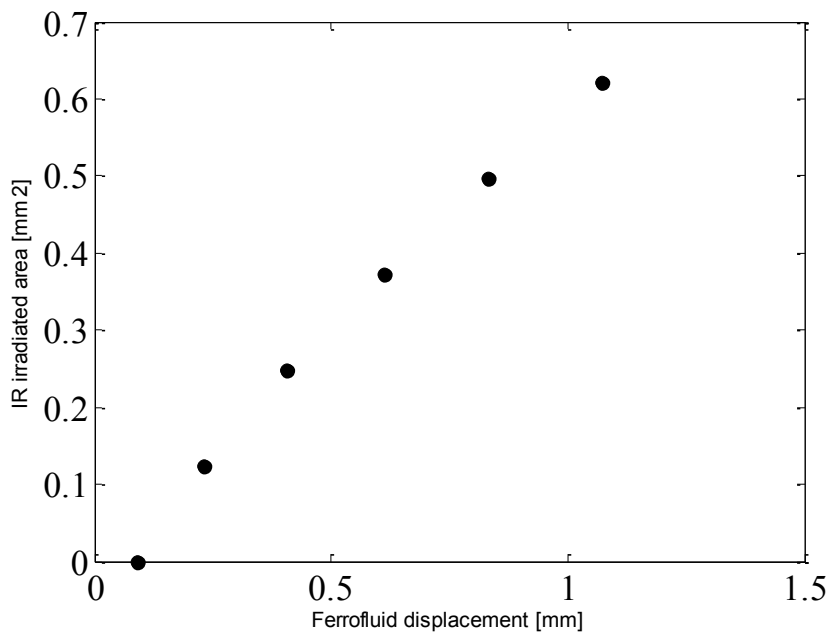


Figure 3-22 The relationship between the displacement of the ferrofluid spike (free-end) and the irradiated area. A linear fitting by model  $y = 0.7x + 0.06$  produces an estimated residual of  $0.008 \text{ mm}^2$ .

The relationship between  $A_d$  and the IR output voltage is sustained by the well known linear relationship:



$$V_{out}^{IR} = RHA_d \quad (3.14)$$

Where  $V_{out}^{IR}$  is the output voltage of the Infra-Red detector,  $R$  is the device responsivity,  $H$  is the irradiation,  $A_d$  is the irradiated area of the detector.

### *The model*

The ferrofluid behavior can be described by the following model, assuming  $\vec{z}$  the axis in the direction of the mass movement:

$$F_m - F_g + F_a + F_h + F_{st} = V_f \rho_f \ddot{z} \quad (3.15)$$

$F_m$  is the magnetic force generated by the permanent magnets acting on the ferrofluid mass. Being verified assumptions described in section 2.4, the magnetic force can be expressed as Equation 2.4: the magnetic force acts as a retaining force which contrasts external perturbations on the device (and consequently on the ferrofluid volume) and governs the movement of the inertial mass around its equilibrium position.

$F_g$  is the gravitational force,  $F_a$  is the Archimedes force,  $F_h$  is the hydrodynamic drag force along the sensing axis and  $F_{st}$  is related to the external stimulus:

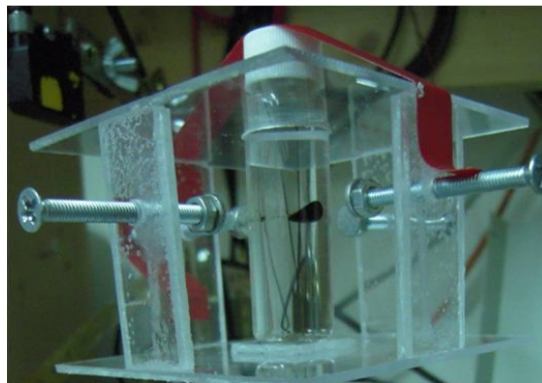
$$F_{st} = \rho_f V_f u(t) \quad (3.16)$$

where  $u(t)$  is the external acceleration applied to the device.

The linear relationship between the target stimuli applied to the device and the ferrofluid displacement, stated by model (3.15), and the linear behavior of the IR readout strategy above discussed would predict the almost linear behavior of the inertial sensor developed which is also evidenced by experiments presented in the following.

*The experimental results*

Figure 3-23 shows real views of the experimental prototype. In particular, Figure 3-23a is the assembled prototype where the plexiglass structure, the glass beaker filled with water and the sliding mechanism ruling the position of the magnetic actuators can be distinguished. Figure 3-23b is a detailed view of the ferrofluid spike.



a)



b)

Figure 3-23 a) real view of the device; b) zoom of the ferrofluid spike; the IR emitter diode is represented by a dotted circle while the photodiode is represented by a filled white circle.

For the prototype developed a volume of 0.15 ml of EFH1 ferrofluid by Ferrotec was used.

The readout strategy is based on a coupled IR device (OSRAM SFH 4350 - SHARP PT380F). In Figure 3-24 a schematization of the dedicated conditioning electronics used for the IR device is shown.

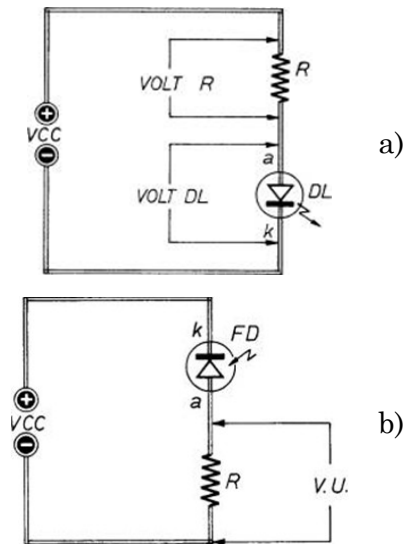


Figure 3-24 Conditioning electronics used for a) diode and b) photodiode.

The experimental set-up adopted to investigate the device behavior, shown in Figure 3-25, consists of a shaker to stimulate the device and a reference system to implement an independent measurement of the inertial stimulus imposed to the device. In particular, the OADM-12U6430/S35A laser device was used; main specifications for the laser device are reported in Table 3-3.

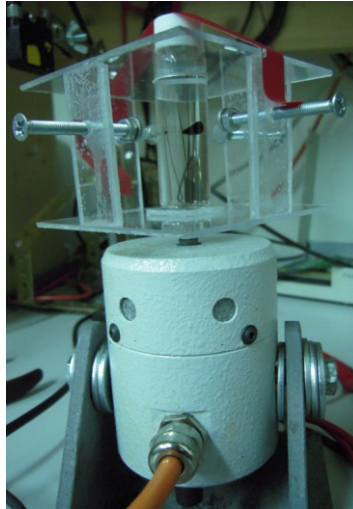


Figure 3-25 Experimental set-up for the device characterization.

Table 3-3 Laser specifications

| <i>Specifications</i>  | <i>Value</i>                          |
|------------------------|---------------------------------------|
| <i>Measuring range</i> | $16 \div 26 \text{ mm}$               |
| <i>Resolution</i>      | $0.002 \div 0.005 \text{ mm}$         |
| <i>Linearity error</i> | $\pm 0.006 \div \pm 0.015 \text{ mm}$ |
| <i>Response time</i>   | $< 900 \mu\text{s}$                   |

To characterize the behavior of the inertial sensor the system has been solicited by a frequency sweep signal.

Figure 3-26 shows the response of the shaker system to such stimulus measured through the laser system.

It must be observed that the obtained frequency response is fully coherent and compatible with the investigations to be accomplished on the developed prototype.

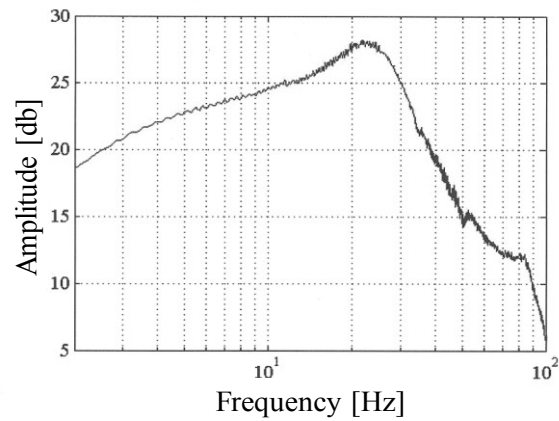


Figure 3-26 Frequency response of the shaker.

To characterize the behavior of the inertial sensor the shaker system has been solicited by a frequency sweep ranging from 1 Hz to 100 Hz. Figure 3-27 shows the frequency response obtained through the experimental survey which evidences a resonant frequencies of 5 Hz.

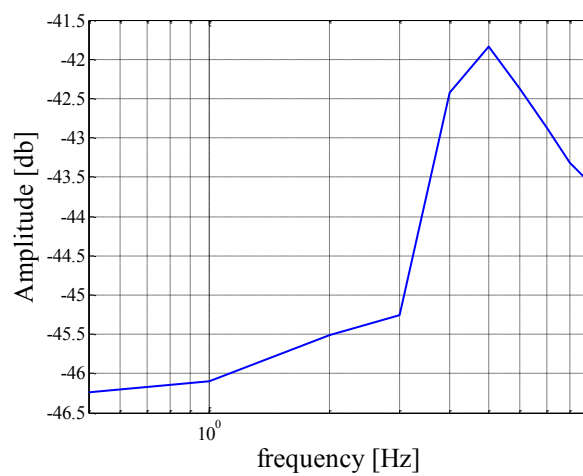


Figure 3-27 Frequency response of the device.

Taking into account the observed resonance frequency of 5.0 Hz, Equation 2.7 leads to a  $k$  value estimation of 0.16 N/m. The latter belongs to the typical range of values observed in case of ferrofluid volumes subjected to similar magnetic field strength. This result confirms the consistency of model (3.15).

Figure 3-28 evidences a quasi-linear trend in the device response according to considerations outlined above. Figure 3-28a shows the observed sensor response (in terms of the IR device output voltage) as a function of displacement and acceleration stimuli @4 Hz. Models adopted to interpolate data in case of displacement and acceleration stimuli are:

$$z = 420.74V_{out}^{IR} - 1.67 \quad (3.17)$$

$$\ddot{z} = 265.67V_{out}^{IR} - 1.05 \quad (3.18)$$

The sensor behaviors for stimuli @8 Hz are reported in Figure 3-28b, where the following fitting models have been used:

$$z = 869.12V_{out}^{IR} - 3.83 \quad (3.19)$$

$$\ddot{z} = 2195.2V_{out}^{IR} - 9.7 \quad (3.20)$$

Above equations are examples of the device behaviors for two different frequencies of the input stimulus.

The sensor resolution estimated for the cases considered are:

(0.023 mm, 0.014 m/s<sup>2</sup>) @4 Hz and (0.0479 mm, 0.12 m/s<sup>2</sup>) @8 Hz, respectively.

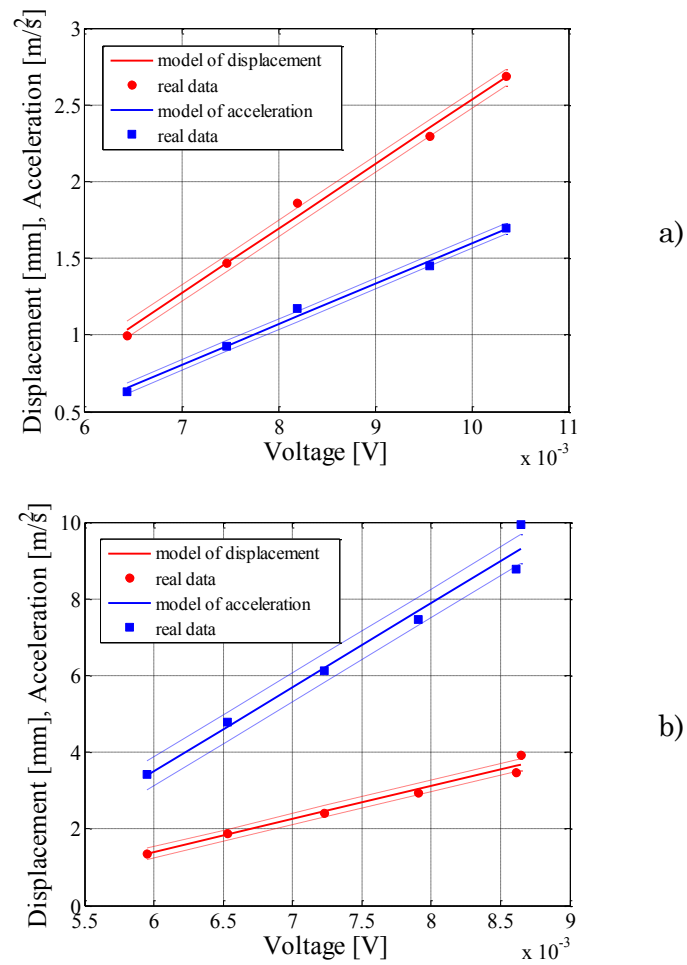


Figure 3-28 Calibration diagrams for stimuli a) @4 Hz and b) @8 Hz. Dotted lines represent the uncertainty band estimated.

### 3.3. A ferrofluid flow sensor

In this section a novel and low cost approach to implement a flow sensor is presented [30]. The proposed methodology exploits a ferrofluid mass

dispersed in water to convert the flow rate into the mass displacement which is then measured by an inductive readout strategy.

Advantages in the use of a magnetic fluid as the active mass of this device are due to the possibility to fix specifications such as operating range and responsivity by tuning the applied magnetic field intensity, high robustness against mechanical shocks, the electric isolation between the device electronics and the liquid media and the physical decoupling between the device structure and the readout system. The latter feature is strategic for measurement in hostile contexts involving invasive liquid media and requiring the substitution of the liquid housing. It must be considered that the disposable part of the device (the pipe) is very cheap while the external electronics implementing the readout strategy can be re-used. Another interesting feature of the proposed methodology consists in the possibility to implement such sensing strategy also in pre-existing channels by injecting a mass of ferrofluid and clamping the external control and reading units.

Above the already mentioned advantages, it must be highlight that the proposed sensor, conversely to traditional magnetic flow sensor, can operate also with non conductive liquid.

Mentioned features allow for the use of the device in several real contexts (from bio-medical systems to applications requiring non invasive measurements in liquids).

The working principle of the sensing strategy, the device architecture, the sensor implementation and experimental results aimed to demonstrate the efficiency of the proposed methodology are discussed in the following sections.



*The working principle*

The ferrofluid flow sensor consists of a glass pipe filled with water and a drop of ferrofluid, and external components used for shaping the ferrofluid mass as a spike. In particular, the shaping system, exploiting the *Rosensweig effect*, is composed by two permanent magnets placed on the top and on the bottom of the pipe.

The permanent magnet on the top of the pipe is used to implement a retaining magnetic force acting on the mass of ferrofluid. As it will be described in the following sections, the magnetic force acting on the ferrofluid mass resembles an equivalent elastic force (or equivalent spring) which maintains the ferrofluid drop in a compliant position.

Moreover, the distance between the top magnet and the ferrofluid defines the magnetic pressure acting on the ferrofluid and hence its physical properties such as viscosity and density. As it will be clearly stated and demonstrated in the following, this mechanism will allow for modifying the device performances (e.g. responsivity, operating range and bandwidth) which are strictly related to the value of the equivalent spring constant.

The magnet on the bottom side is used to confer the ferrofluid the spike shape.

A schematization of the device is shown in Figure 3-29.

The ferrofluid acts as the inertial mass of the system and an imposed flow rate produces a deformation of the spike around its equilibrium position; such a displacement from the equilibrium position is sensed through an inductive readout.

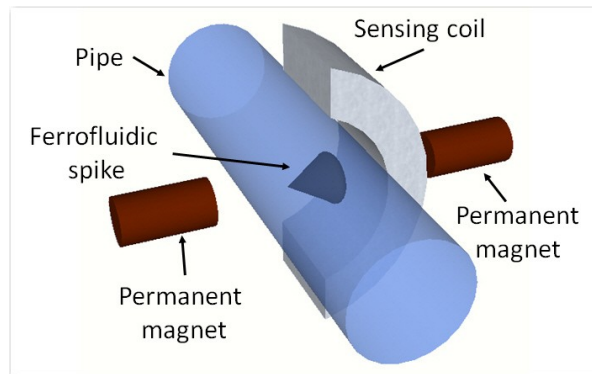


Figure 3-29 Schematization of flow sensor.

### *The sensing strategy*

The inductive readout strategy converting the ferrofluid displacement into an electric signal is implemented through a coil (wounded on the pipe) and the conditioning electronics shown in Figure 3-30.

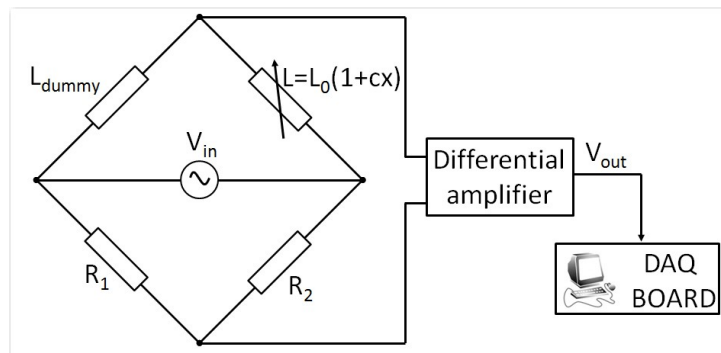


Figure 3-30 Conditioning electronic for the inductive readout strategy.

The reading electronic uses an AC bridge to produce a voltage signal related to the imposed flow rate.  $L_2 = L_0(1 + cx)$  is the inductive

sensor where  $c$  is a sensor parameter and  $x$  is the displacement of the ferrofluid. Due to the small displacement of the ferrofluid mass, a linear behaviour of  $L_2$  with  $x$  has been supposed.  $L_1$  is a dummy coil with the same structure of  $L_2$  and it is used to compensate exogenous effects acting on the sensing coil.

The relationship between the output voltage of the conditioning electronics,  $V_{out}$ , and  $x$  is supposed to be sustained by the following relationship:

$$\frac{V_{out}}{V_d} = -G \frac{(k+1)(1+cx) - 2k}{2(k+1)} \quad (3.21)$$

where  $V_d$  is the bridge driving voltage,  $k = R_1/R_2$  is the gain of the instrumentation amplifier.

In the case of  $R_1 = R_2$  Equation 3.21 becomes:

$$\frac{V_{out}}{V_d} = -G \frac{cx}{2} \quad (3.22)$$

Above assumptions, including Equation 3.21 will be confirmed by experiments presented in the following.

### *The model*

In order to investigate the qualitative behaviour of the device some experiments have been performed on the sensor prototype. In particular, the displacement of the ferrofluid spike for increasing values of the flow intensity,  $Q$ , and the retaining magnetic field,  $H_{ret}$  has been observed.

An Hall Effect sensor has been used to estimate the magnitude of the retaining magnetic field in the proximity of the ferrofluid spike base.

Although the device has been always tested in the laminar regime (the largest estimated Reynold number is around 630), snap shots shown in Figure 3-31 and Figure 3-32 highlight that flow rates lower than a fixed threshold produce only a displacement of the ferrofluid tip in the direction of the flow, while flow rate larger than the threshold value will cause also a displacement of the whole ferrofluid mass from the compliant position. Figure 3-31 shows the low flow rate case for  $H_{ret} = 153 G$ . Figure 3-31a and Figure 3-31b show the ferrofluid tip position for a null flow rate and a flow rate of 0.3 ml/s, respectively. Two bold lines highlight the tip movement while evidence the fixed position of the spike.

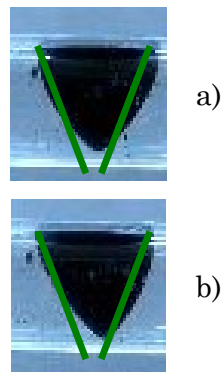


Figure 3-31 The ferrofluid spike inside the pipe for a) null flow rate and b) 0.3 ml/s. The mass of ferrofluid changes its shape due to the tip movement

Frames in Figure 3-32 show the ferrofluid mass behaviour for a null flow rate and for flow rates of 1ml/s and 1.7 ml/s. Two effects are evincible: the spike tip movement and the displacement of the whole mass in the flow direction. Three solid vertical lines highlight such behaviour.

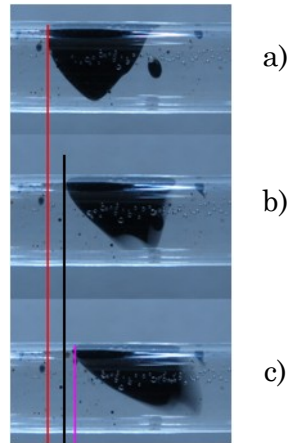


Figure 3-32 The ferrofluid spike inside the pipe for a) null flow rate, b) 1  $ml/s$  and c) 1.7  $ml/s$ . The mass of ferrofluid changes both its shape (tip deflection) and position.

These combined effects of the flow rate on the ferrofluid spike (deformation and displacement) strongly encourage the use of the inductive readout strategy which would detect the average modification of the ferrofluid.

Figure 3-33 shows the relationship between the flow rate and the ferrofluid mass displacement for different values of the retaining magnetic field. These results have been obtained through a dedicated image processing procedure. Actually, streaming of the ferrofluid peak movement for different flow rate intensity has been recorded. Frames extracted from each streaming have been then processed to estimate the steady state position of the ferrofluid spike tip. Two typical frames with superimposed cursors adopted to estimate the tip position of the ferrofluid spike are shown in Figure 3-34.

As expected, data shown in Figure 3-33 confirm the possibility to modify the operating range of the device and its responsivity by modifying the retaining magnetic field. In particular it can be observed that, the device responsivity increases as the magnetic field intensity decreases.

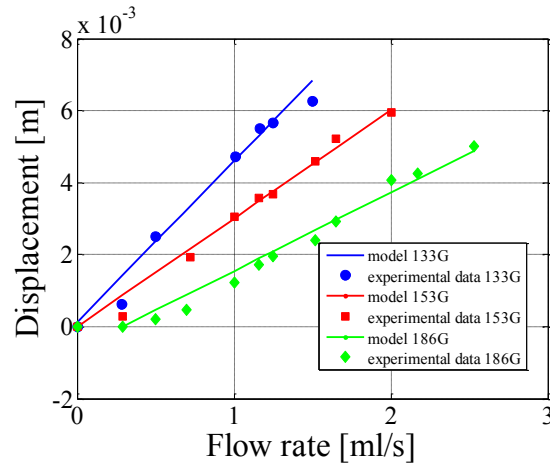


Figure 3-33 Behaviors of the ferrofluid spike tip displacement,  $x$ , as a function of the flow rate intensity for different values of the retaining magnetic field.

Models adopted to interpolate data in Figure 3-33 are shown in the figure. Linear relationships have been used which highlight the possibility to adopt a linear model to describe the device behavior. The latter consideration represents an important premise for the definition of the device model. In fact, the observed linear behavior encourages to model the magnetic force by a spring-like model.

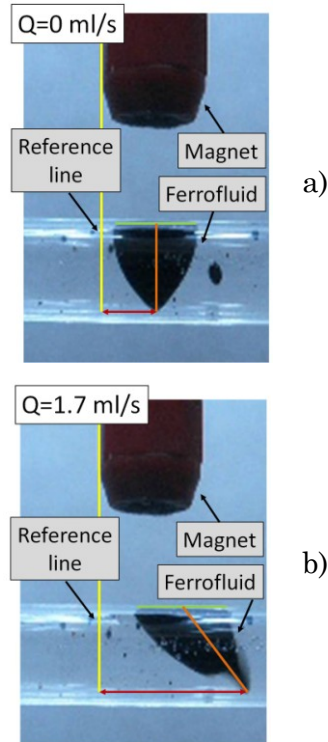


Figure 3-34 Two typical frames for the estimation of the ferrofluid spike tip position.

On the basis of the above considerations the following model has been adopted to describe the device behavior:

$$\rho_f V_f \ddot{x} = F_m + 6\pi\eta R_{eq} \left( \frac{Q}{S} - \dot{x} \right) \quad (3.23)$$

where  $x$  is the position of the ferrofluid spike along the sensing axis,  $V_f$  is the ferrofluid volume, which for the device under test is 0.01 ml,  $\rho_f$  is the ferrofluid density,  $\eta$  is the ferrofluid viscosity,  $F_m = -kx$  is the magnetic force generated by the retaining magnet and resembling the

equivalent elastic force,  $Q$  is the flow rate,  $S$  is the pipe section, which for the device under test is  $1.96 \cdot 10^{-5} \text{ m}^2$ ,  $R_{eq}$  is the radius of an equivalent ferrofluid sphere with the same volume of the adopted ferrofluid mass, which for the device under test is  $1.3 \cdot 10^{-3} \text{ m}$ .

The last term in Equation 3.23 represents the contributions of both the hydrodynamic force and the target flow rate.

As first, some considerations can be performed on the static behavior of the device described by the following relationship coming from Equation 3.23:

$$x = \frac{6\pi\eta R_{eq}}{Sk} Q \quad (3.24)$$

The following form of the device responsivity,  $R$ , is evincible from Equation 3.24:

$$R = \frac{x}{Q} = \frac{6\pi\eta R_{eq}}{Sk} \quad (3.25)$$

Table 3-4 summarizes the device specifications for the investigated values of the retaining magnetic field. Such values have been estimated by matching (3.24) and (3.25) to experimental data shown in Figure 3-33 and using specifications of the adopted ferrofluid given in Table 2-1.

Concluding it can be affirmed that results presented in Figure 3-33 along with Equation 3.25 can be used during the design phase to estimate the retaining magnetic field amplitude assuring the device performances in terms of responsivity and operating range.



Table 3-4 Summary of the device performances as a function of the retaining magnetic field.

| $H_{ret}$ | $k$        | <i>Responsivity</i> | <i>Max flow rate</i> |
|-----------|------------|---------------------|----------------------|
| 133 G     | 0.0017 N/m | 0.0046 m/(ml/s)     | 1.5 ml/s             |
| 153 G     | 0.0025 N/m | 0.0030 m/(ml/s)     | 2 ml/s               |
| 186 G     | 0.0034 N/m | 0.0022 m/(ml/s)     | 2.5 ml/s             |

Simulations have been also performed to investigate the dynamic behavior of the flow sensor by the numerical integration of model (3.23). Figure 3-35 shows how the frequency responses of the device change as a function of the retaining magnet field. Simulations have been performed in the Matlab® environment by using parameters reported in Table 2-1 and Table 3-4 and the specifications of the real architecture described in the next section.

As expected, due to the increment of the  $k$  factor with  $H_{ret}$ , the resonance frequency of the device increases as the magnetic field increases. The estimated frequency bands of the device are typical of sensing systems adopting ferrofluids as the active mass.

Experimental observations reported in Figure 3-33, in the case of  $H_{ret} = 186G$ , show a negligible device sensitivity to flow rate lower than 0.3 ml/s. This effect can be reasonably justified by static friction phenomena due to the high magnetic pressure acting on the ferrofluid. To simulate such effect a non linearity (dead zone) has been considered which null the flow rate effect up to 0.3 ml/s.

For the sake of completeness Figure 3-36 shows the simulated step response of the device as a function of the retaining magnetic field.

Above considerations reinforce the need for the preliminary observations shown in Figure 3-33, which become mandatory for a suitable modeling of the device behavior.

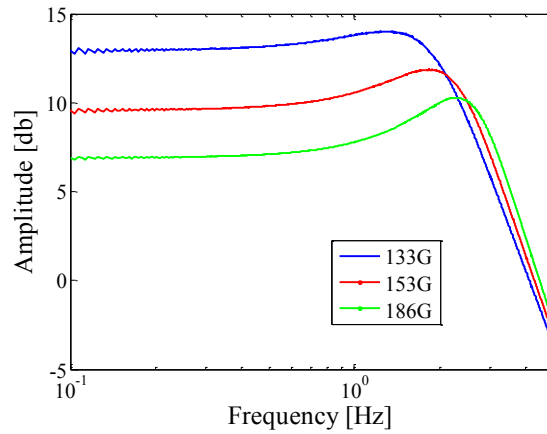


Figure 3-35 Simulated frequency responses of the device.

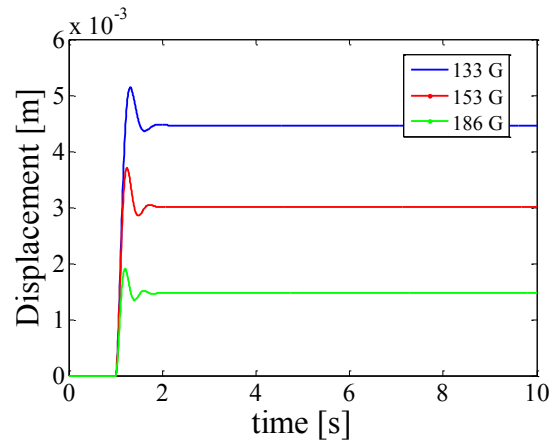


Figure 3-36 Simulated step responses (for  $Q=1$  ml/s) of the device.

*The experimental results*

The sensor prototype is shown in Figure 3-37a where the pipe, the sensing coil and the magnetic shaping system are evincible.

Figure 3-37b shows a real view of the experimental set-up adopted to characterize the behavior of the flow sensor prototype. The sensing coil has been omitted for the sake of convenience. A sliding mechanism ruling the position of the shaping magnets can be distinguished. As it will be demonstrated in next sections, the possibility to regulate the magnet position allows for defining some specifications of the device such as the operating range and the responsivity.

The adopted glass pipe has an inner diameter of 5 mm and a length of about 180 mm and it is filled with de-ionized water. A ferrofluid mass of 0.01 ml (EFH1 by Ferrotec) was used. The sensor is supported by a plexiglass structure which is positioned over a tank. A pump was used to force inside the channel a controlled flow rate which is independently measured by a graded outlet tank.

Experimental results obtained for retaining magnetic fields of about 133 G, 153 G and 186 G are given in Figure 3-38 which shows the device output voltage as a function of the flow rate intensity.

As shown in Figure 3-30 PC based measurement station including a data acquisition board and a LabVIEW® interface has been used to acquire and process signals given by the readout electronics.

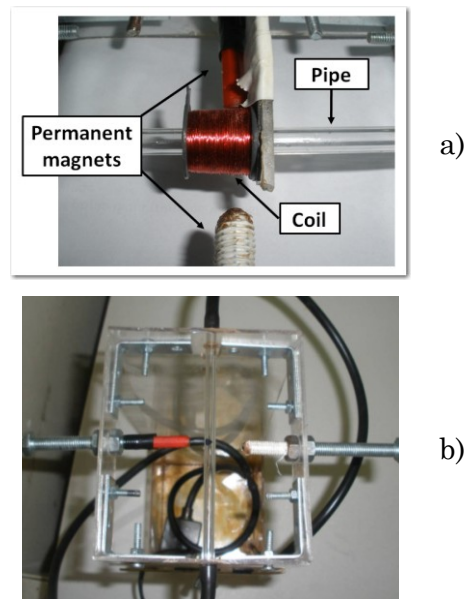


Figure 3-37 a) real view of the flow sensor; b) experimental set-up adopted to characterize the sensor prototype.

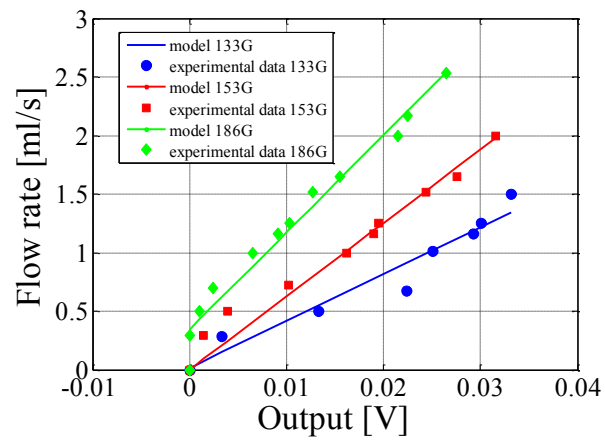


Figure 3-38 The sensor response for retaining magnetic fields of 133 G, 153 G and 186 G.

As expected, for increasing value of the magnetic field, the operative range increases and the sensitivity decreases.

The calibration models of the flow sensor in the operating conditions investigated ( $H_{ret}$  of 133G, 153G and 186G) are summarized in Table 3-5. The obtained linear behavior of the device (see Table 3-5) along with the observed linear relationship between  $Q$  and  $x$  (see Figure 3-33) allows for confirming assumption (3.21) related to the behavior of the readout electronics.

Table 3-5 Calibration models of the flow sensor in different operating conditions.

| $H_{ret}$ | <i>Calibration diagram</i> |
|-----------|----------------------------|
| 133 G     | $Q = 40.56 V_{out}$        |
| 153 G     | $Q = 62.72 V_{out}$        |
| 186 G     | $Q = 82.88 V_{out} + 0.35$ |

The device operating range, responsivity, resolution and uncertainty, in the different operating conditions are summarized in Tab.4.

Table 3-6 Device specifications for three different values of the retaining magnetic field.

| <i>Specifications</i> | $H_{ret}$              |                        |                        |
|-----------------------|------------------------|------------------------|------------------------|
|                       | <i>133 G</i>           | <i>153 G</i>           | <i>186 G</i>           |
| <i>Magnetic field</i> | <i>133 G</i>           | <i>153 G</i>           | <i>186 G</i>           |
| <i>Max flow rate</i>  | <i>1.5 ml/s</i>        | <i>2 ml/s</i>          | <i>2.5 ml/s</i>        |
| <i>Responsivity</i>   | <i>0.0247 V/(ml/s)</i> | <i>0.0159 V/(ml/s)</i> | <i>0.0121 V/(ml/s)</i> |
| <i>Resolution</i>     | <i>0.0117 ml/s</i>     | <i>0.0105 ml/s</i>     | <i>0.0130 ml/s</i>     |
| <i>Uncertainty</i>    | <i>5.41 %</i>          | <i>3.58 %</i>          | <i>3.40 %</i>          |

### **3.4. A ferrofluid inclinometer with a time domain readout strategy**

In this section a novel approach to implement a tilt sensor is presented. The proposed methodology exploits a continuous movement of a ferrofluid mass on the housing structure.

The novelty of this device as respect to solutions already available in the literature is the exploitation of a low cost reading architecture adopting a time domain readout strategy. The device output, in fact, consists in the frequency of an opportune signal coming from the modulation of a coil output voltage due to the mass movement. The output is then digital and it can be easily use with digital systems (e.g. microcontroller). Actually, the tilt information is achievable through the observation of the time elapsed by the ferrofluid mass moving between two fixed sections of the pipette.

Other advantages of the proposed inclinometer are related to the use of ferrofluid as inertial mass: high robustness against mechanical shocks, the electric isolation between the device electronics and the liquid media and the physical decoupling between the device structure and the readout system: the pipe, that is the disposable part of the device, is very cheap while the external electronics used to implement the readout strategy can be re-used.

As for the other devices above presented, also the inclinometer sensing strategy should be used in pre-existing channels by injecting a mass of ferrofluid and clamping the external control and the reading units; for such a reasons the device could be used also in several biomedical contexts.

The inclinometer working principle, the device architecture, the sensor implementation and experimental results are discussed in the following sections.

### *The working principle*

The TDR (Time Domain Readout) inclinometer resembles the same architectures implementing two other kinds of inclinometer recently developed at the DIEEI laboratory: a static inclinometer [31] and a resonant inclinometer [32].

In the static inclinometer the magnetic mass surrounded by de-ionized water is contained inside a glass pipe and is subjected to a magnetic field generated by external coil wounded around the pipe. The device exploits the relationship between the ferrofluid mass position and the device tilt coming from the equilibrium between the magnetic force and the gravitational force in the steady state regime. The mass position is detected by two coils (wound around the pipe) in differential configuration. The device shows some problems about the adhesion between the mass and the pipe for small tilts.

To improve the performance for small tilts, a resonant inclinometer was developed. The new configuration uses two actuation coils to move the ferrofluid mass around its equilibrium position thus preventing the adhesion of the ferrofluid to the glass pipe and therefore improving the sensor resolution.

The TDR inclinometer consists of a glass pipe containing a ferrofluid mass dispersed in water, an actuation coil to control the ferrofluid mass and to excite the sensing coils and two sensing coils to monitor the mass position. Both the actuation and the sensing coils are wound

around the pipe, as schematized in Figure 3-39: the actuation coil is positioned in the centre of the pipe while the sensing coils are symmetrically just opposed as respect to the actuation coil and they are connected in a differential configuration.

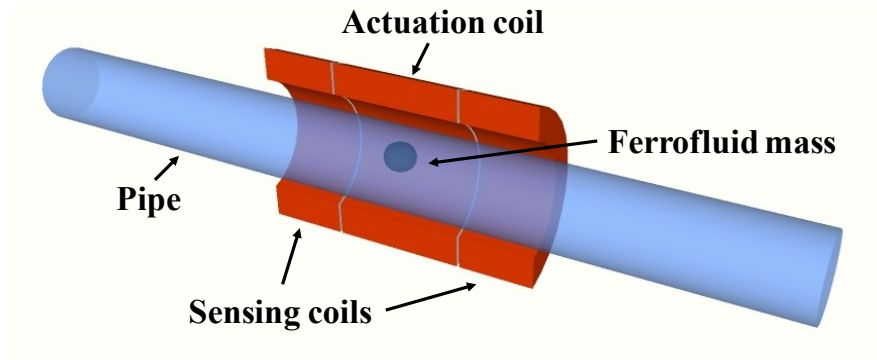


Figure 3-39 Schematization of the developed TDR inclinometer.

The actuation coil is driven by an excitation current

$$i_{exc} = I_0 + I_M \sin(\omega t) \quad (3.26)$$

The  $I_0$  bias is used to implement a retaining mechanism.

When the  $I_0$  bias is turned on the ferrofluid mass experiences a magnetic force able to suck the ferrofluid volume to the centre of the coil independently on its current position inside the pipe. The sinusoidal term is used to excite the sensing coils, while its effect on the retaining mechanism is negligible.

In the case of a null tilt the mass resides in its equilibrium position in the centre of the actuation coil. When a tilt is imposed to the device and  $I_0 = 0$  the mass moves towards the end of the pipe. When the mass reaches a control position inside the channel the restoring current  $I_0$  is



forced into the actuation coil thus producing a magnetic force sucking the mass towards the center of the actuation coil. When the mass reaches the coil center the  $I_0$  current is switched off and the mass starts again to move along the channel.

The time elapsed by the ferrofluid mass to reach the control position from the centre of the actuation coil depends on the tilt magnitude.

The mass position is detected by the sensing coils while the restoring current is activated by comparing the readout output signal with fixed levels. In this way the ferrofluid mass continuously oscillates between the centre of the actuation coil and the control position with the advantage prevent potential static friction.

The output signal of each sensing coil is given by the excitation current modulated by the mass movement inside the channel; the frequency of the modulating signal depends on the imposed tilt, because the time duration of each sweep of the ferrofluid mass between the coil center and the control section depends on the tilt.

A block diagram of the working principle is reported in Figure 3-40, while an example of the output signal modulation due to the mass position is shown in Figure 3-41: as it can be observed, the frequency of the modulating signal increases with the imposed tilt: higher is the tilt, higher is the frequency.

The idea behind the proposed approach is to use the frequency information of the de-modulated signal as the sensor output information to quantify the imposed tilt.

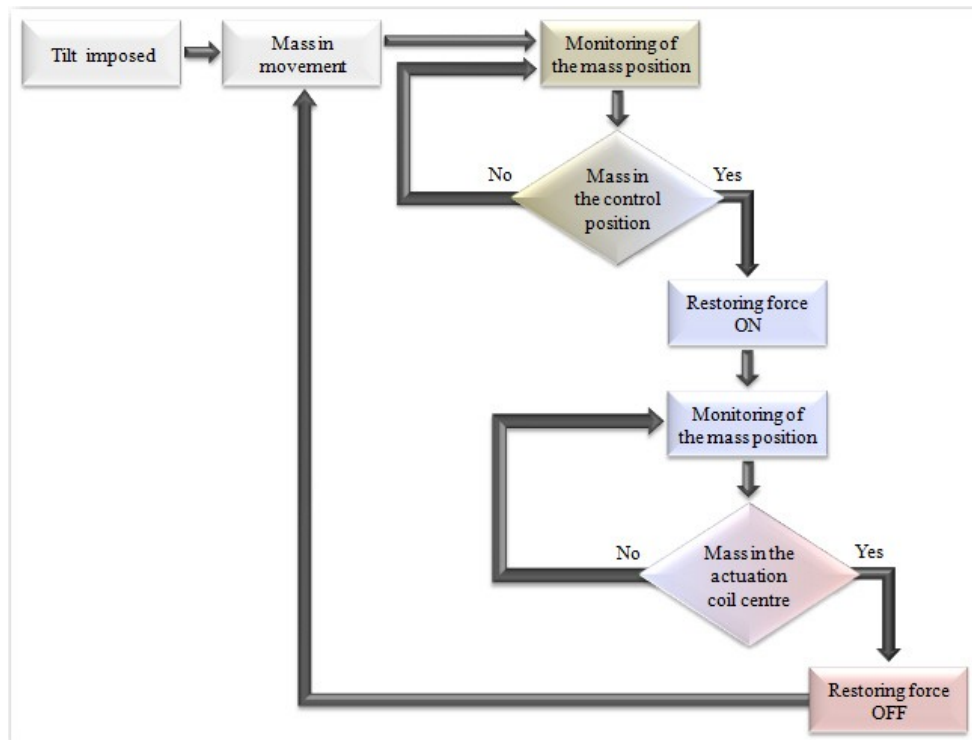
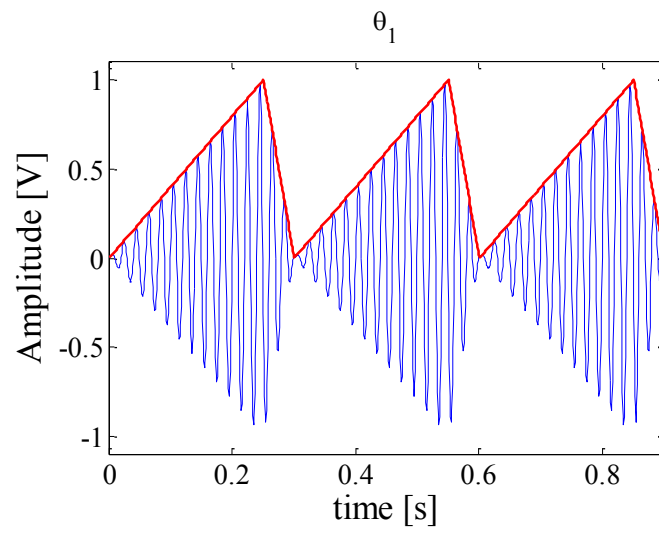
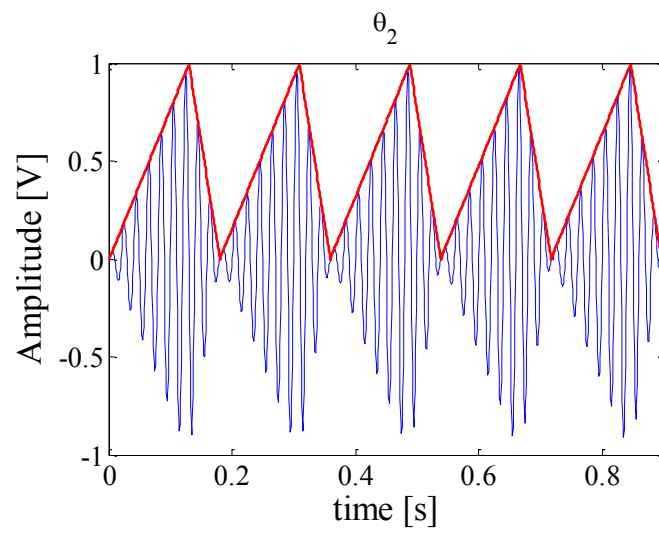


Figure 3-40 Block diagram of the sensor working principle.



a)



b)

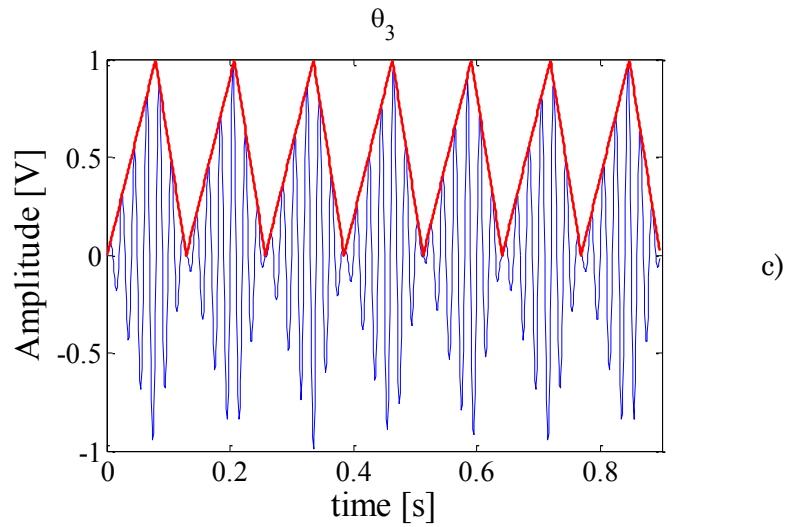


Figure 3-41 Qualitative behavior of the signal modulation due to the mass movement:  $\theta_1 < \theta_2 < \theta_3$ .

When a tilt is applied, the mass moves towards the end of the pipe; such a movement is detected through an inductive readout strategy.

The actuation coil is driven with a sinusoidal current with, when it is necessary, the superimposed constant current. The electronics used to drive the actuation coil is shown in Figure 3-42.

The two sensing coils are connected in a differential configuration, as shown in Figure 3-43.

The output voltage of the readout electronics,  $V_{out}$ , is given by the excitation signal coming from the actuation coil modulated by the movement of the ferrofluid mass between the centre of the coil and the control point. As already mentioned the frequency of the demodulated signal is strictly related to the device tilt.

The basic assumption is that the tilt dynamic is negligible as respect to the carrier frequency.

The output voltage signal of the readout system,  $V_{out}$ , is correlated to the ferrofluid position inside the pipe.

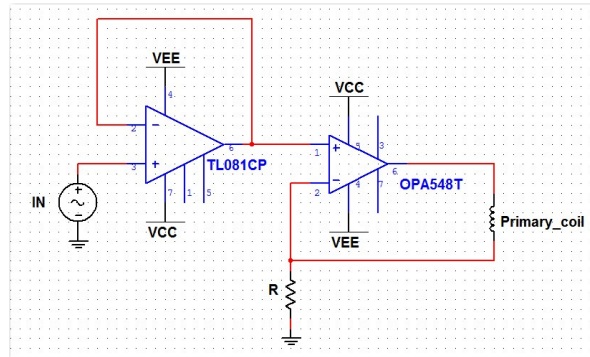


Figure 3-42 A scheme of the electronics used to drive the actuation coil.

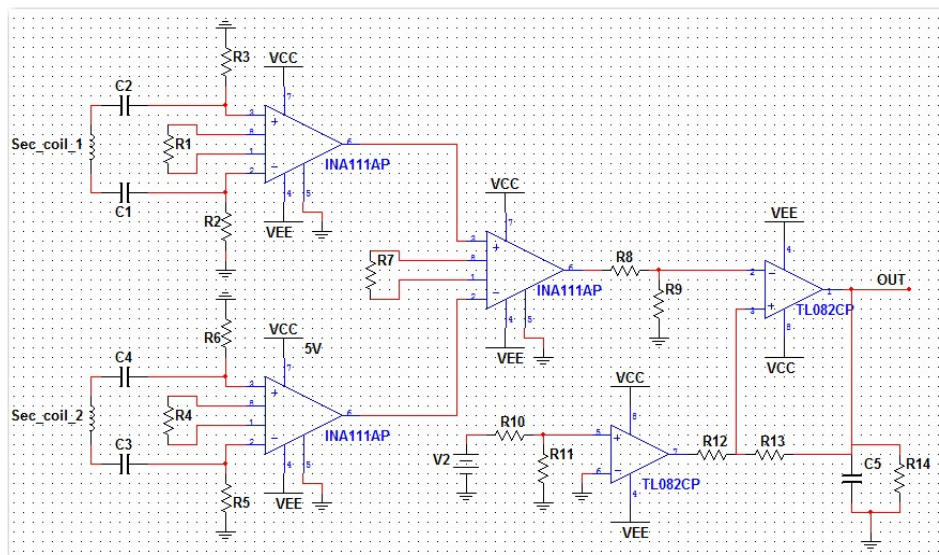


Figure 3-43 A scheme of the electronics used to sense the mass position.

When the mass reaches the first threshold position (fixed almost at the end of the sensing coils), and consequently the output voltage assumes a value  $V_{th}^1$ , the bias current  $I_0$  is turned on; such a current generates a magnetic force that sucks the ferrofluid mass towards the actuation coil center. When the ferrofluid mass reaches the centre of the actuation coil the  $V_{out}$  voltage assumes the value  $V_{th}^2$  and the  $I_0$  current is switched off. In this condition the ferrofluid mass is free to move again towards the pipe end.

*The model*

A simplified form of model describing the device behavior is the following:

$$\rho_f V_f \ddot{z} = -F_h + F_m + F_g \quad (3.27)$$

where  $F_h$  is the hydrodynamic drag force expressed by Equation 2.8;  $F_g$  is the gravitational force including the Archimedes's force, that can be expressed as

$$F_g = (\rho_f - \rho_l) V_f g \sin \theta \quad (3.28)$$

where  $\rho_f$  and  $\rho_l$  are the ferrofluid density and the liquid density, respectively and  $\theta$  is the applied tilt;

$F_m$  is the magnetic force generated along the sensing axis by the actuation coil and expressed through Equation 2.5. Such a force is applied only to recall the mass from the threshold position to the actuation coil center; it means that the magnetic force has two different values as function of the mass position:

$$\begin{cases} F_m = \frac{V_f \chi_f \mathbf{B}_x}{\mu_0} \partial \mathbf{B}_x & \text{in the threshold} \\ F_m = 0 & \text{otherwise} \end{cases} \quad (3.29)$$

### *The real device*

The sensor prototype is shown in Figure 3-44 where the pipe, the two sensing coils and the actuation coil are evincible.

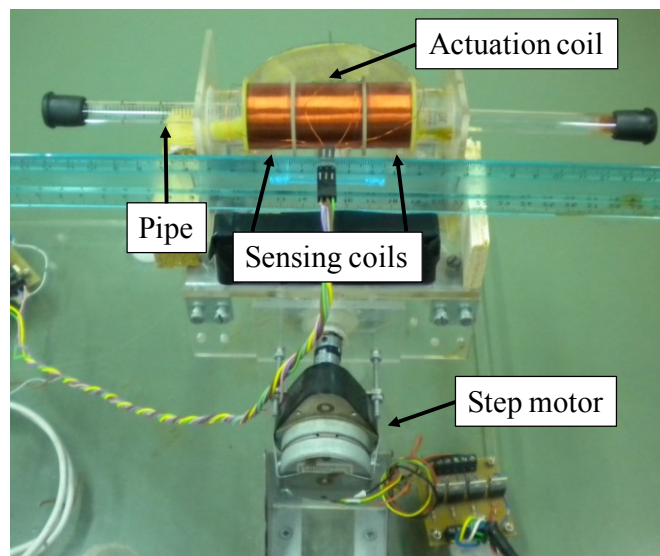


Figure 3-44 Real view of the developed prototype.

In order to implement the RTD measurement strategy (to monitor the output signal  $V_{out}$  and control the imposed retaining force) a dedicated environment in LabVIEW® software was developed. The realized interface is made of three different parts. The first section controls the step motor used to impose the tilt in the two direction.

The second one compares continuously the peak value of the output voltage with the two threshold values  $V_{th}^1$  and  $V_{th}^2$  and it controls the wave generator in order to add or remove the offset to the driving signal of the actuation coil. The control of the wave generator is due through the IEEE488 protocol. Three graphs show the signal processing: one shows the sinusoidal waveform acquired from the sensing coils. This wave is modulated in amplitude by the movement of the ferrofluid mass; another graph represents the timed-values of the array obtained from measure peak-to-peak voltage. The sequence of the peak-to peak voltage values gives a modulated waveform whose frequency is related with the imposed tilt, as it is evincible in Figure 3-41.

The last graph represents the single value of the peak-to-peak signal. The visual result of this graph is a white ball moving up and down. It seems to be a real movement of the ferrofluid mass inside the glass tube.

The third section of the LabVIEW® tool saves the data in a file.

Figure 3-45 shows snapshots of the interface realized to characterize the inclinometer.

Parameters of the actuation and sensing coils are reported in Table 3-7 and in Table 3-8.



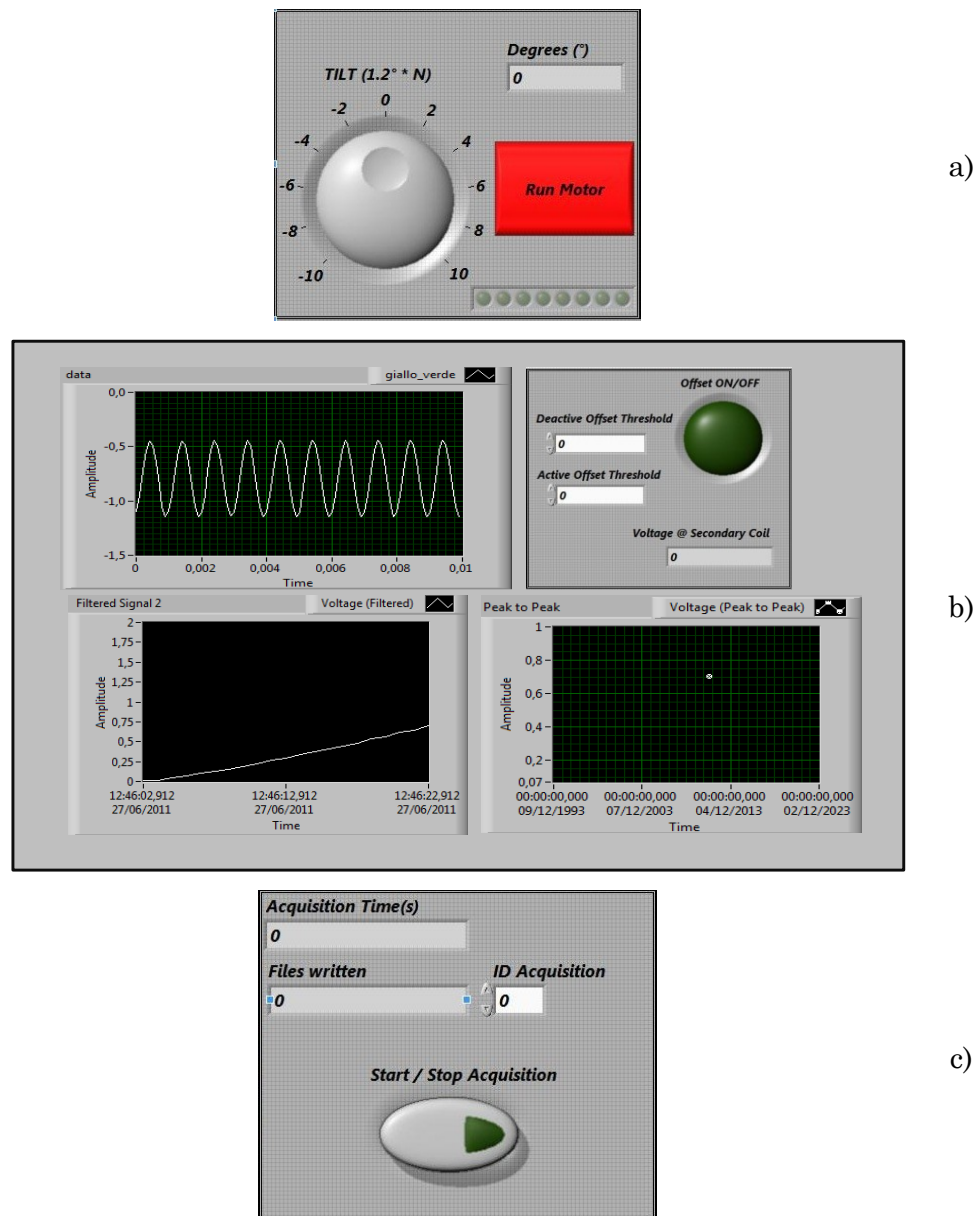


Figure 3-45 Snapshots of the realized interface: a) control of the tilt, b) comparison of the output signal with the two threshold values and monitoring of the signal processing, c) acquisition of the output data.

Table 3-7 Parameter values of the driving system.

| <b><i>Actuation coil</i></b> | <b><i>Value</i></b>           |
|------------------------------|-------------------------------|
| <i>Layers number</i>         | <i>12</i>                     |
| <i>Spires per layer</i>      | <i>~128</i>                   |
| <i>Length</i>                | <i>0.03 m</i>                 |
| <i>Internal radius</i>       | <i>0.013 m</i>                |
| <i>Resistance</i>            | <i>79 <math>\Omega</math></i> |
| <i>Inductance</i>            | <i>41.1 mH</i>                |

Table 3-8 Parameter values of the sensing system.

| <b><i>Sensing coils</i></b> | <b><i>Value</i></b>             |
|-----------------------------|---------------------------------|
| <i>Layers number</i>        | <i>12</i>                       |
| <i>Spires per layer</i>     | <i>~85</i>                      |
| <i>Length</i>               | <i>0.02 m</i>                   |
| <i>Internal radius</i>      | <i>0.013 m</i>                  |
| <i>Resistance</i>           | <i>53.2 <math>\Omega</math></i> |
| <i>Inductance</i>           | <i>23.9 mH</i>                  |

In order to implement the experimental set-up for the device characterization a step motor with a minimum step size of  $0.06^\circ$  was used.

A set of experimental measures was performed applying tilt steps of  $1.2^\circ$  from  $0^\circ$  to  $13.2^\circ$ .

The acquired signal is the modulated waveform; the information related to the mass displacement is obtained by calculating continuously the peak-to-peak voltage of the sinusoidal signal modulated by the ferrofluid mass position.

Examples of signals acquired for different imposed tilts are reported in Figure 3-46, while the comparison between the demodulated waveforms obtained for two imposed tilts (e.g  $1.2^\circ$  of difference) is shown in Figure 3-47. As it is evincible, the frequency of the modulated wave grows with the imposed tilt.

Such a behavior is highlighted also in Figure 3-48a-d, in which the power spectrum density (e.g PSD) signals in Figure 3-46, are reported. Each figure shows several superimposed PSD obtained with repeated measures relative to the same tilt: figures evidence the good repeatability of the device.

The calibration model of the developed inclinometer is reported in Figure 3-49.

Sensitivity and resolution obtained by the experimental characterization of the device are respectively  $0.0776 \text{ Hz}/^\circ$  and  $0.2535^\circ$ .

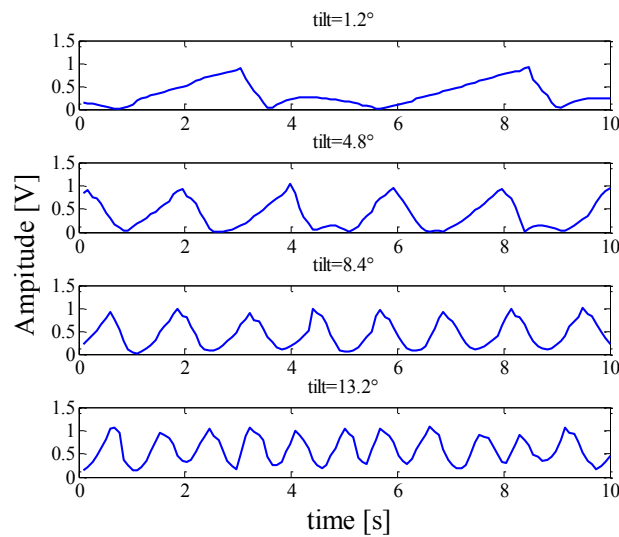


Figure 3-46 Output signals obtained imposing different tilt values.

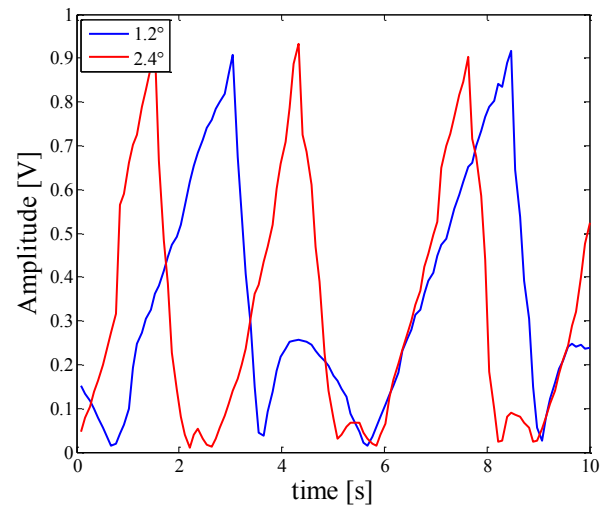
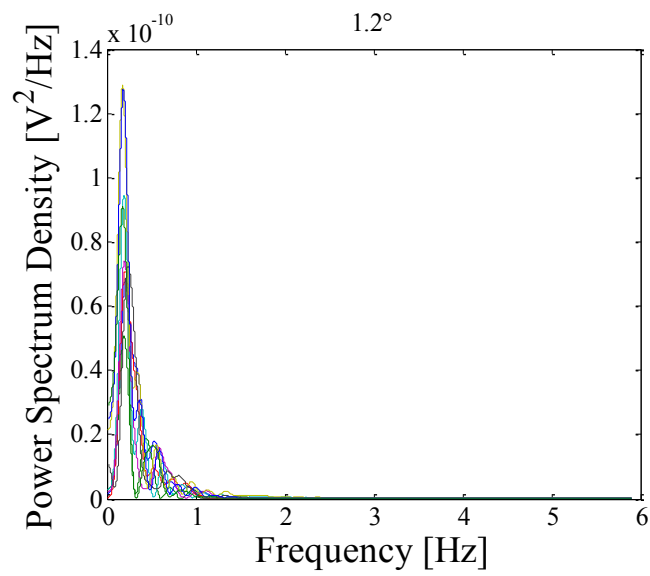
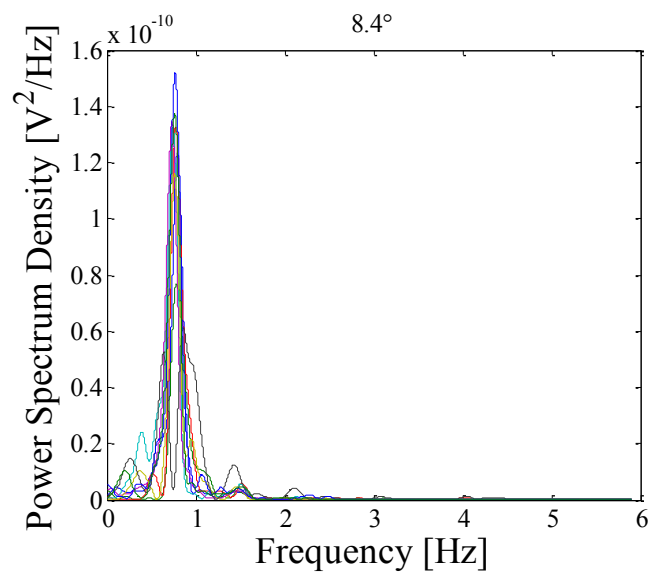
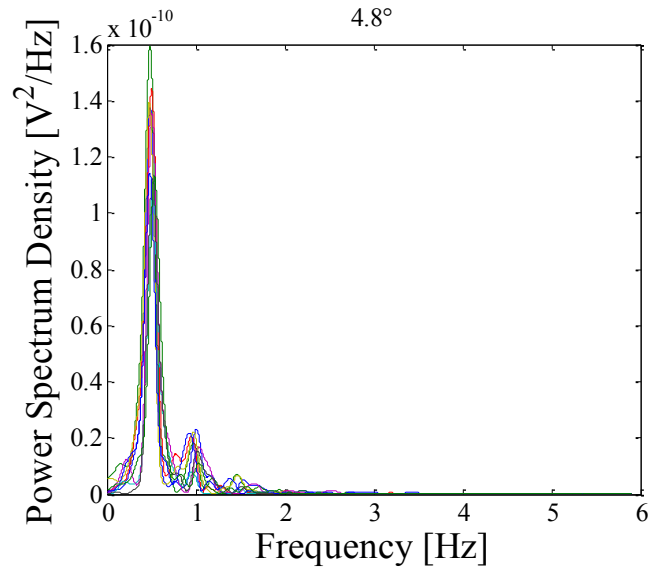


Figure 3-47 Comparison between two output signal with consecutive values of imposed tilt.



a)



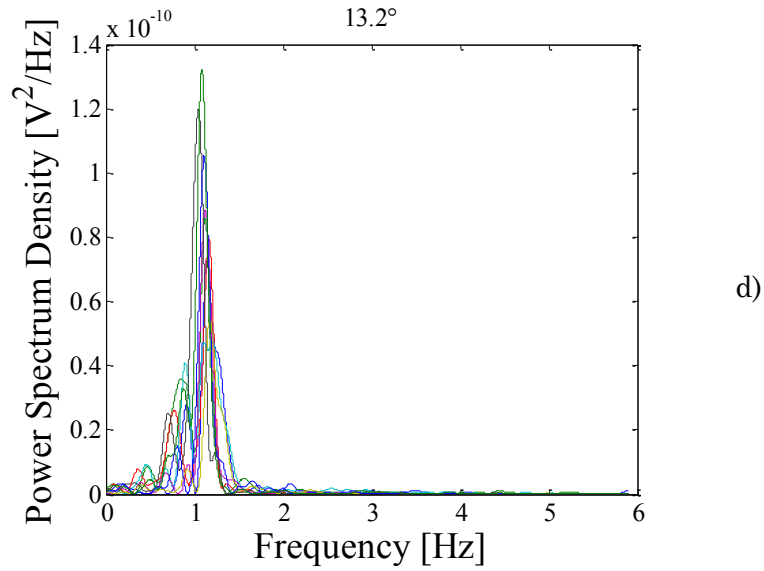


Figure 3-48 Power Spectrum Density vs frequency for four different imposed tilts: a)1.2°, b) 4.8°, c) 8.4° and d) 13.2°. it is evincible that the peak depends on the tilt.

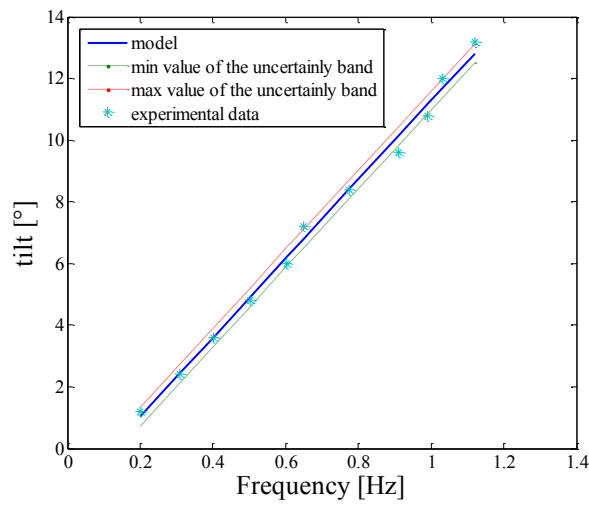


Figure 3-49 Calibration model of the TDR inclinometer.

# Chapter 4

## *ACTUATORS BASED ON FERROFLUIDS*

A field of wide interest in the modern research is related to the biomedical applications, as previously evidenced in Chapter 2. All the bio-applications, also if different each others, need a fluidic system to control and move magnetic particles along a predefined path to reach, for examples, particular cell for chemical treatment (as linking with biomolecules) or specific part of the human body (as in the hyperthermia or in drug delivery technique) or simply to move the particles inside a channel (as in magnetic separation).

A fluidic system needs of valves to open and close the channel, of plungers to move liquids in which the particles are placed and of systems to move and control the particles.

In this chapter two actuators realized to perform Lab-on-chip and generally bio-medical systems are proposed.

Actuators shown in the next sections demonstrate that it is possible to realize both plungers and valves using ferrofluids, and that a complete control of the mass movement is easily implementable through a magnetic actuation. This constitutes a concrete premise for the realization of integrated systems containing both the sensor and the fluidic part able to control and perform the process.

The use of ferrofluids gives the opportunity to handle small volumes of fluids: this is an important aspect in micro-systems because it allows to reduce the consumption of expensive reagent.

Other advantages of using ferrofluids in actuators are the low cost, the intrinsic robustness against mechanical shocks and the possibility to produce flexible structures to use for different purposes.

In the next sections developed actuators are reported, together with a description of their working principle, the prototype realization and the characterization.

#### **4.1. The “One Drop” ferrofluid pump**

The need in many applications of low cost transducers capable to handle small amounts of liquids is focusing the research community towards the development of innovative and cheap solutions. The satisfaction of



hard specifications, such as reliability and reasonable accuracy in the frame of low cost and disposable devices, is a big deal.

Although conventional micropipette can sample small liquid volumes with a precision ranging in 3-5%, the development of novel solutions showing high reliability (against shock) and flexibility (easy implementation into pre-existing pipes) especially when the dimensions are seriously shrank (e.g. MEMS) are highly demanded.

Advantages of the realized pump are the decoupling of the mechanical part from the electrical part of the system, that assures both electrical insulation of the liquid media to be pumped and the re-usability of the driving tool. The latter is the expensive part of the system, while the cheap section housing the fluid could be considered as the disposable part of the system.

Another advantage of the decoupled structure consists on the possibility to implement the pumping mechanism in a section of a pre-existing pipe without invasive actions damaging or modifying the original structure, thus increasing the flexibility of the methodology proposed and widening potential applications also in the field of biomedical devices. Actually, the pump could be implemented by injecting a single drop of ferrofluid in the considered channel and by externally plugging the electromagnetic driving system.

The use of magnetic fluids as the active mass offers the possibility to develop a device with electrically tunable specifications. As an example, in the case of the considered pump, the drop pressure and the flow rate are strictly dependent on the current flowing in the driving electromagnets. As already stated, the latter behavior resides in the possi-

bility to control the physical properties of the ferrofluid (such as the viscosity) by changing the intensity of the tuning magnetic field.

Other interesting features of such approach are related to the absence of mechanical moving parts and solid-inertial masses which provides to the device high reliability and robustness against mechanical shocks.

The device presented in this section represents an improvement of systems previously developed at the DIEEI laboratory: the “*FP1\_D*” pump [33], in which a pump using a single mass of ferrofluid to implement both a plunger and two valves is presented. The actuation system is driven by digital signals. The pump *FP1\_D* was revisited and a new driving mode was addressed. The new solution, based on an analog driving system (hereinafter “*FP1\_A*”), guarantees enhanced performances such as linearity and smooth pumping flow [34], [35], [36].

In the following sections, details about the pump operation principle are given, along with the actuation strategy adopted; the prototype realized is shown and its characterization are presented, together with an optical validation of the ferrofluid mass movement.

#### *The pump architecture*

In order to implement the pumping mechanism, a single volume of ferrofluid is injected into a glass pipe filled with de-ionized water. A sheet of paper magnet is located on the bottom of the pipe to fix the position of the magnetic fluid. Actually, the magnetic dipole is aligned with the glass pipe to allow for the formation of a “magnetic tank”: the ferrofluid is flattened at the bottom of the channel thus allowing the fluid flow.

An array of five electromagnets, wrapping the pipe with the paper-magnet, allows for the formation and the managing of a ferrofluid cap (acting contemporaneously like a valve and a plunger). Actually, this cap is moved from the left to the right due to the magnetic pressure generated by the electromagnets array.

A schematic of the proposed prototype is shown in Figure 4-1, where the driving electromagnetic system and the single ferrofluid cap are perceivable.

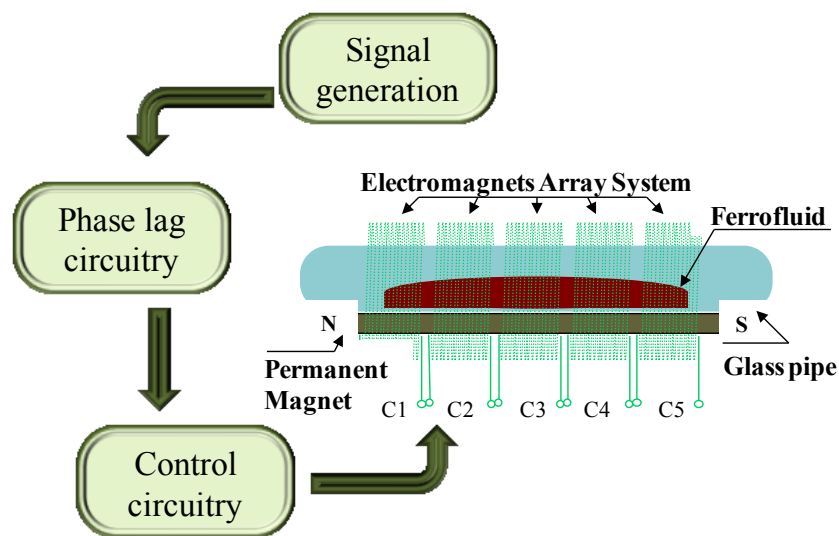


Figure 4-1 Schematic of the proposed design for FP1 pump architecture. It is possible to view the magnetic volume flattened in the channel due to the magnetic force applied by the permanent magnet, the polarization of the electromagnet and the coils, used to create and move the cap of magnetic fluid in the glass pipe, wounded around pipe and magnet.

As respect to the implementation described in [33], where the electromagnets array system is digitally controlled, the new driving strate-

gy uses a set of analog driving signals which guarantee a continuous movement of the ferrofluid cap and consequently a more linear fluid flow. This is due to the intrinsic principle of operation of the “FP1\_A” device.

The latter feature, coupled with the very simple architecture of this device, make the proposed solution very attractive for a large field of interest including bio-medical applications.

#### *The actuation strategy*

The proposed analog actuation strategy is based on the following idea: while the permanent magnet keeps flattened the ferrofluid on the bottom of the pipe, the electromagnets are excited to suitably manage the ferrofluid cap inside the pipe (creation and propagation).

In particular, the electromagnets are excited with five sinusoidal signals, with frequency  $\omega$ , showing a phase lag,  $\varphi$ , between each other.

The idea consists in the realization of a moving magnetic field (a moving magnetic wave) inside the pipe, which is materialized by the ferrofluid that, thanks to its magneto-rheological properties, conforms to the field distribution along the pipe. In this way the “cap” appears as formed at the left end of the pumping section and then smoothly moved toward the right side. When the rightmost point is reached, the cap reappears to the leftmost section of the pump. In Figure 4-2 the actuation strategy is schematized: the step  $d$  is necessary to close the channel when a new pumping sequence occurs avoiding in this way that fluid flows without the plunger action.

This approach is valuable in terms of the fluidity and linearity in the management of the fluid flow and represents an improvement as re-

spect to the digital approach presented in [33]. Furthermore, the fluid pumping can be reversed by reversing the excitation signals sequence of the electromagnets array system.

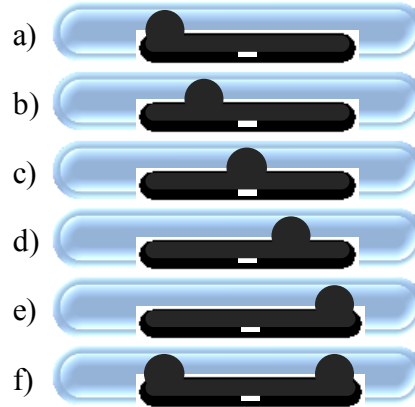


Figure 4-2 Schematization of the actuation strategy used to pump the liquid from the left to the right side of the pipe.

The mechanism leading to the cap formation is evincible by considering the magnetic force along the channel. The force produced by an electromagnet driven by a current,  $i_{exc}$ , and acting on a ferrofluid volume can be expressed as in Equation 2.5, where the magnetic field  $B$  produced by an electromagnet can be expressed through Equation 1.8.

The total magnetic force generated by the electromagnets array can be expressed as:

$$F_{mT} = V_f \chi_f \left( \sum_{i=1}^5 H_i \cdot \nabla \right) \sum_{i=1}^5 B_i \quad (4.1.)$$

where  $i$  counts for the electromagnets in the array.

A simulated time shot of a typical shape of  $F_{mT}$  along the channel is given in Figure 4-3. The simulation has been performed in Matlab® by the implementation of model (4.1). Simulation parameters are evincible in Table 4-1, while for the ferrofluid mass parameters reported in Table 2-1 and Figure 2-4 were used.

Conditions leading to the cap formation are [33], [37]:

$$\begin{cases} F_{mT} = 0 \\ \frac{\partial}{\partial z} F_{mT} < 0 \end{cases} \quad (4.2.)$$

As an example, in the case presented in Figure 4-3, the arrow points the channel position where the total magnetic force fulfils conditions (4.2).

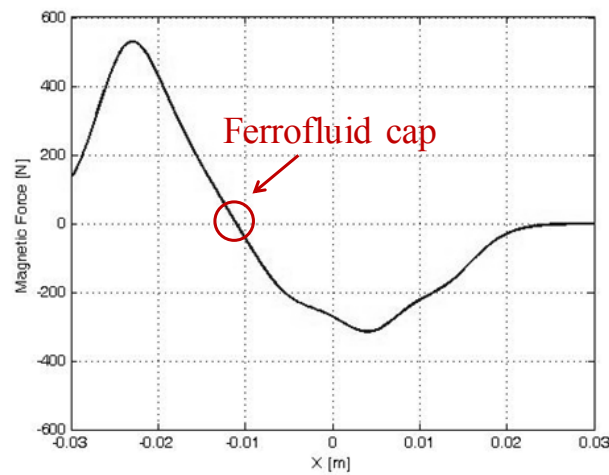


Figure 4-3 The behaviour of the total magnetic force inside the channel and the condition for the cap formation. The driving signals considered are of 400 *mApp* @ 0.5 Hz, while other simulation parameters are evincible by Table 4-1.

Table 4-1 Characteristic of electromagnets used in the Matlab® simulation.

|                           | <i>Value</i>     |
|---------------------------|------------------|
| <i>Coil length</i>        | <i>0.01 m</i>    |
| <i>Coil inner radius</i>  | <i>0.008 m</i>   |
| <i>Number of windings</i> | <i>~2000</i>     |
| <i>Coil resistance</i>    | <i>~65 Ω</i>     |
| <i>Wire diameter</i>      | <i>~0.0002 m</i> |

Two sets of signals were used to drive the electromagnets: sinusoidal signals without a superimposed bias and sinusoidal signals with a superimposed bias. To establish the right phase value to impose in order to have a fluid movement of the ferrofluid mass, simulations were performed.

The first set of signals imposed to the electromagnet array is made by sinusoidal signals without superimposed bias.

The analysis of the  $F_{mT}$  time evolution leads to results in Figure 4-4, showing typical trends of the cap movement. In particular, a set of simulations for different phase lags,  $\varphi$ , have been performed and the results obtained show the possibility to move the ferrofluid cap from the left to the right of the active area (inside the electromagnetic array).

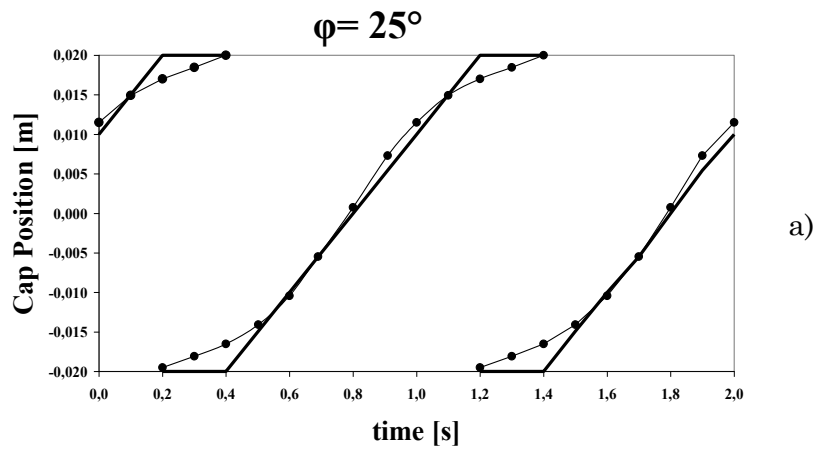
Each plot shows the ideal cap trajectory (a linear movement between the two extremities leading to a constant fluid flow) and the simulated behaviour.

In order to select the optimal  $\varphi$  value assuring the best linearity in the cap movement, the following index has been used:

$$J = \sqrt{\frac{\sum_{i=1}^N [x_N(\varphi) - \tilde{x}_N]^2}{N}} \quad (4.3.)$$

where  $N$  states for the time sampling, while  $x_N(\varphi)$  and  $\tilde{x}_N$  are the simulated and nominal cap positions, respectively.

As can be observed in Figure 4-5, showing the evolution of the index  $J$  as a function of the phase lag, the optimal solution is obtained for a phase lag equal to  $\pi/6$ .





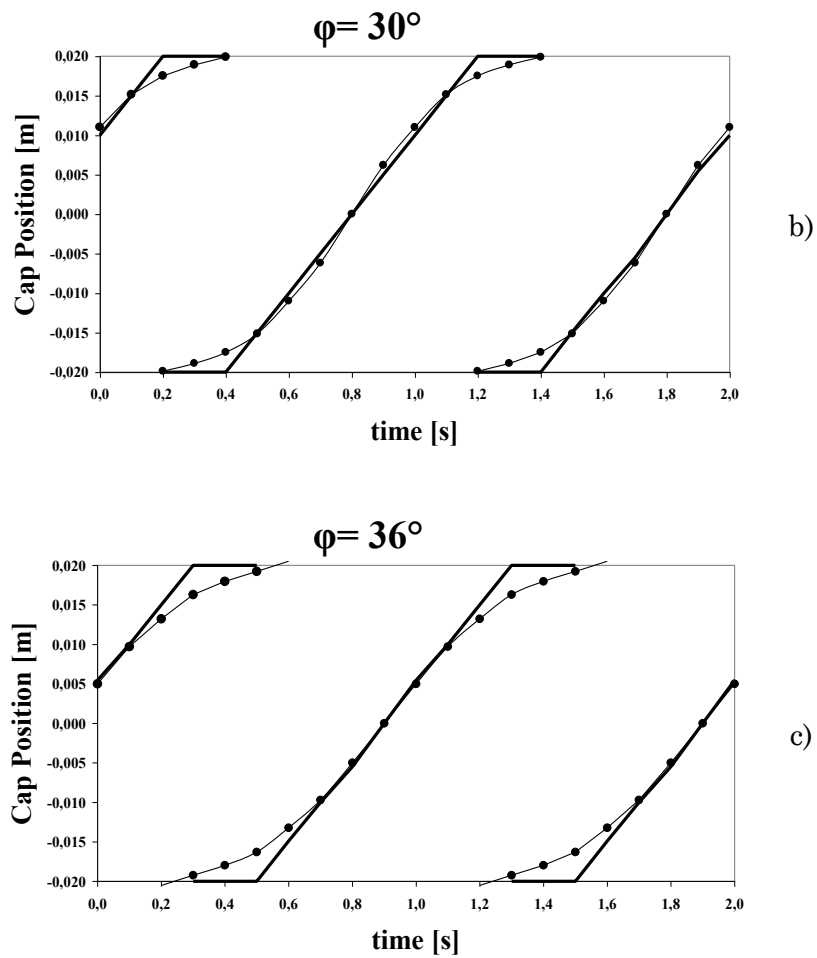


Figure 4-4 Time evolution of the cap position for different phase lags. The ferrofluid cap can be moved from the left to the right of the active area. Each plot shows the ideal cap trajectory (the continuous line) and the simulated behaviour (symbols). Electromagnets are driven with signals without superimposed bias.

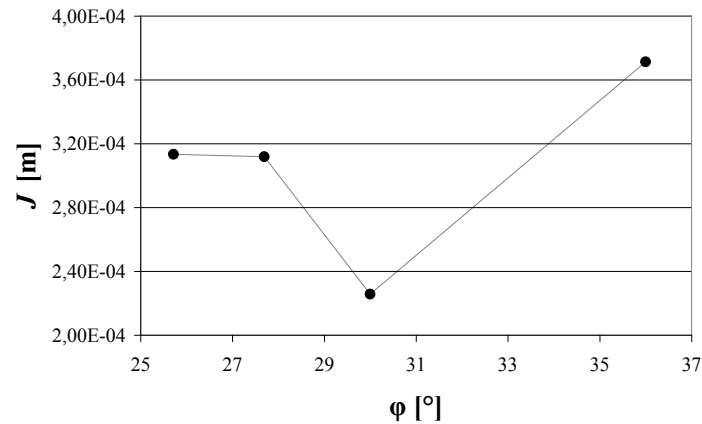


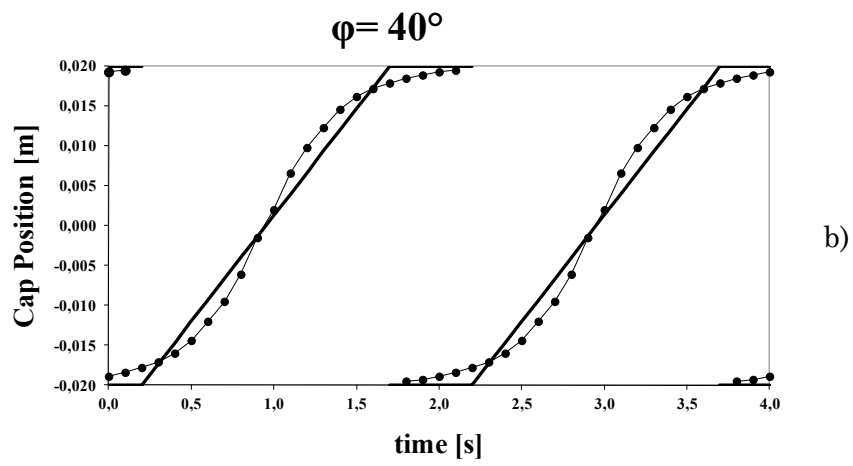
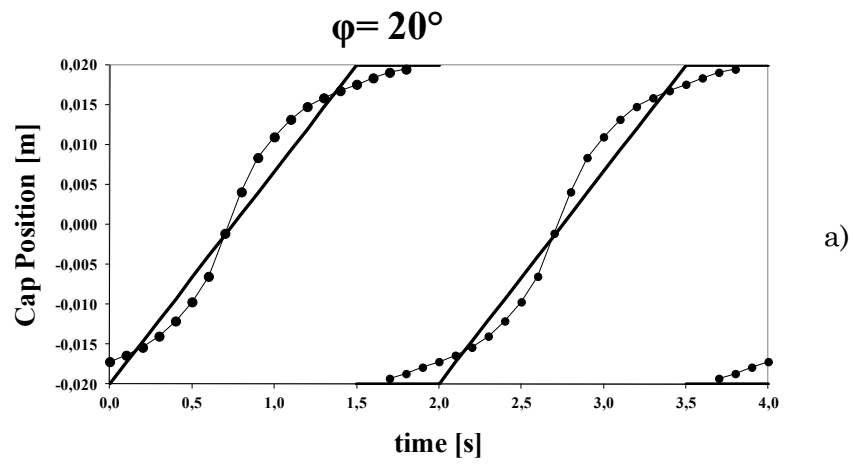
Figure 4-5 The  $J$  index adopted for the optimization of the phase lag between the driving signals.

The same simulations were performed for the second set of imposed signals: electromagnets are driven with sinusoidal signals with frequency  $\omega$ , showing a phase lag  $\varphi$  between each other and a DC level, whose value is chosen in order to have signals totally positive.

To establish the optimal phase between the driving signals the simulated evolutions of the cap position for different phase lags (ranging between  $20^\circ$  and  $70^\circ$ , with step of  $5^\circ$ ) have been investigated. Figure 4-6 shows examples of the simulated behavior.

In order to select the optimal  $\varphi$  value assuring the best linearity in the cap movement, the index  $J$  expressed in Equation 4.3 has been used.

As can be observed in Figure 4-7, showing the evolution of the index  $J$  as a function of the phase lag, the optimal solution is obtained for a phase lag equal to  $60^\circ$ .



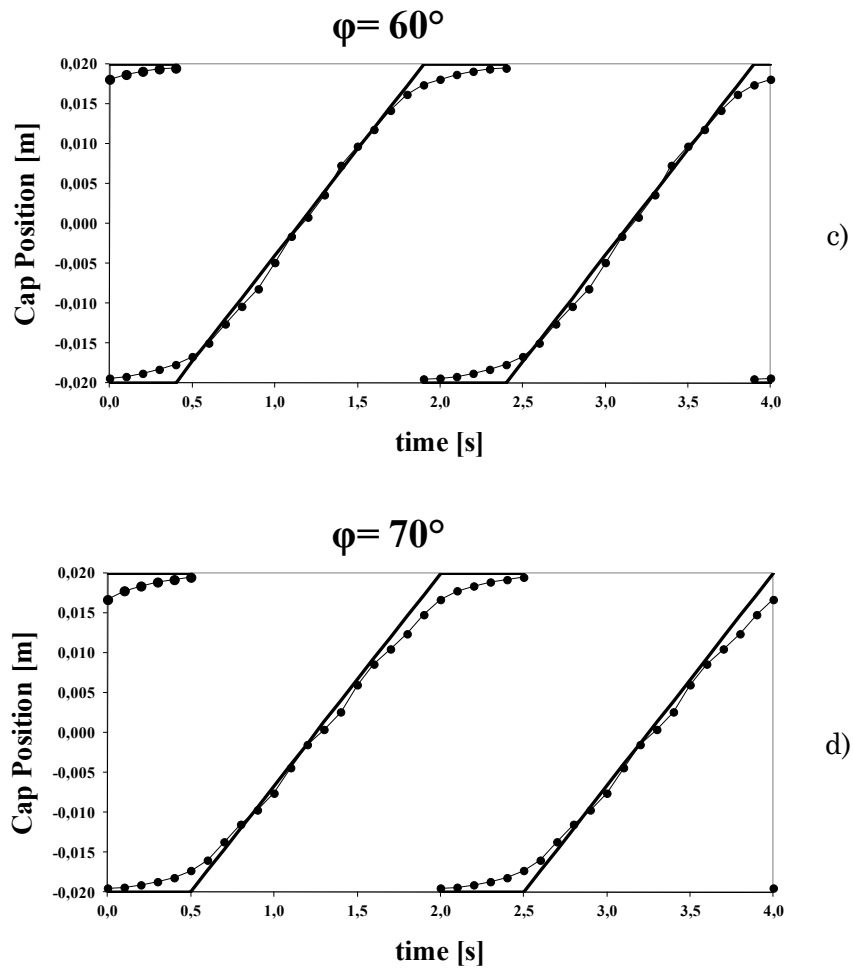


Figure 4-6 Time evolution of the cap position for different phase lags. The ferrofluid cap can be moved from the left to the right of the active area. Each plot shows the ideal cap trajectory (the continuous line) and the simulated behavior (symbols). Electromagnets are driven with signal with offset.

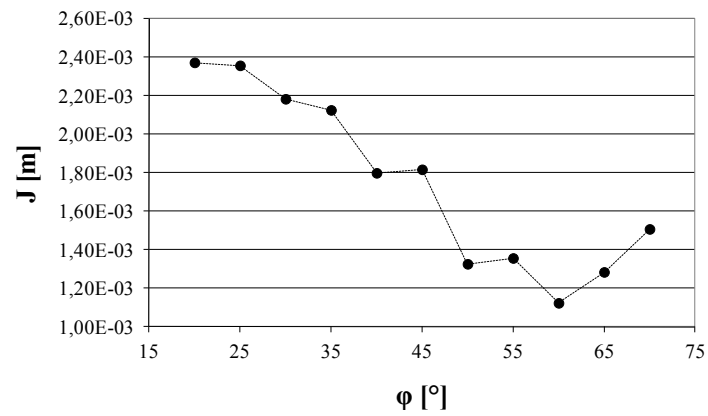


Figure 4-7 Evolution of  $J$  as function of the phase lag.

#### *The prototype realization*

A real view of the prototype realized is shown in Figure 4-8. The prototype consists of five coils wrapped around a glass pipe and a permanent magnet.

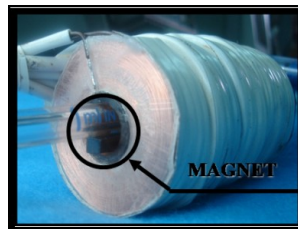


Figure 4-8 The Ferrofluid pump, FP1, prototype: view of the actuation system wrapped around the glass pipe and of the magnet.

Specifications on liquid volume handled per cycle and the maximum drop pressure have been used to perform the device design.

Assuming a typical pipe with an inner diameter of 0.004 m (and outer diameter of 0.007 m), a desired liquid volume per cycle of 0.5 ml/cycle leads to the following choices: a ferrofluid volume injected into the channel of  $V_{f\sim} = 0.3$  ml and an active range of the cap movement of 0.04 m.

As a consequence a magnetic sheet with a length  $L_m = 0.05$  m and five electromagnets with a length  $L = 0.01$  m have been used. Other characteristics of electromagnets realizing the actuation system are reported in Table 4-1.

Electromagnets are driven both with signals without superimposed bias and with signals with superimposed bias, obtaining different characterizations.

It must be observed that the fluid flow rate can be controlled by changing the frequency of the excitation current in the electromagnet, while the flow direction depends on the sequence of actuation.

A maximum current value in each electromagnet of  $I = 500$  mA and a desired maximum drop pressure value of  $DP_{max} = 1$  kPa have been used to estimate the windings number in each electromagnet. Exploiting the following expression of the magnetic pressure acting on a ferrofluid cap

$$DP = \mu(H_1M_1 - H_2M_2) \quad (4.4.)$$

a value of  $N = 2000$  windings for each electromagnet was obtained by using an optimization algorithm implemented in Matlab®.

*Characterization of the FP1\_A pump*

In Figure 4-9 the experimental setup used for the characterization of the pump is presented. It consists of an inlet tank and an outlet tank connected to a single drop pump.

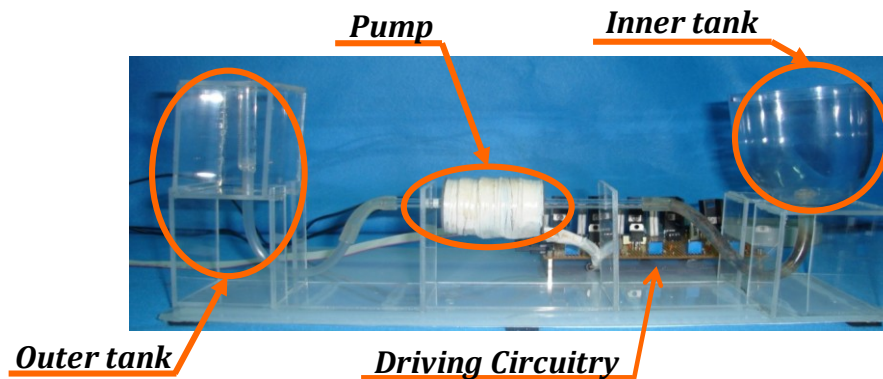


Figure 4-9 Experimental setup used to characterize the FP1\_A pump.

Experiments dedicated to estimate both the drop pressure and the average amount of pumped liquid, over a surveys of several pumping cycles, as a function of the driving current,  $I_{exc}$ , have been performed.

In order to estimate the quantity of fluid pumped over the pump operation a OADM12 laser system, by Baumer, measuring the level of liquid in the outlet tank has been installed. The diameter of the outlet tank is 26.55 mm. Considering a resolution of the laser system less than 0.1 mm, the corresponding resolution in the estimation of the pumped liquid volume is 66,43  $\mu\text{l}$  when driven signals are without offset and 55,36  $\mu\text{l}$  when driven signals are with offset.

The results, obtained for a set of driving current amplitudes and frequencies are given in Figure 4-10 (signals without superimposed

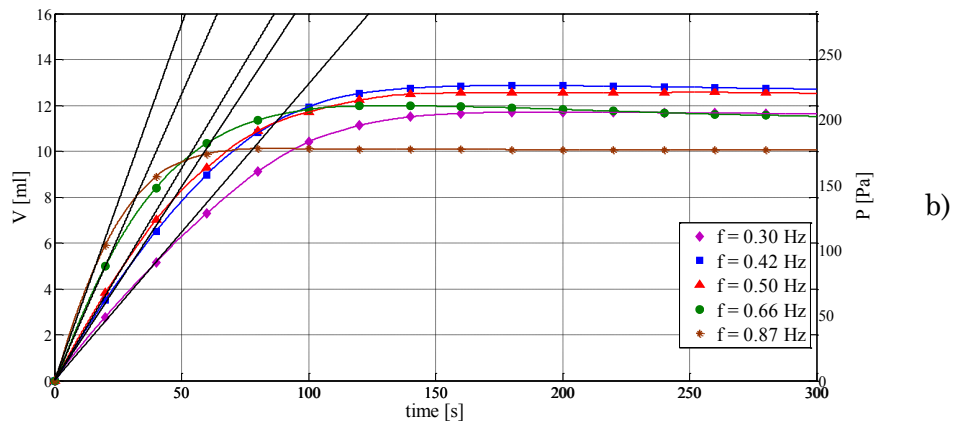
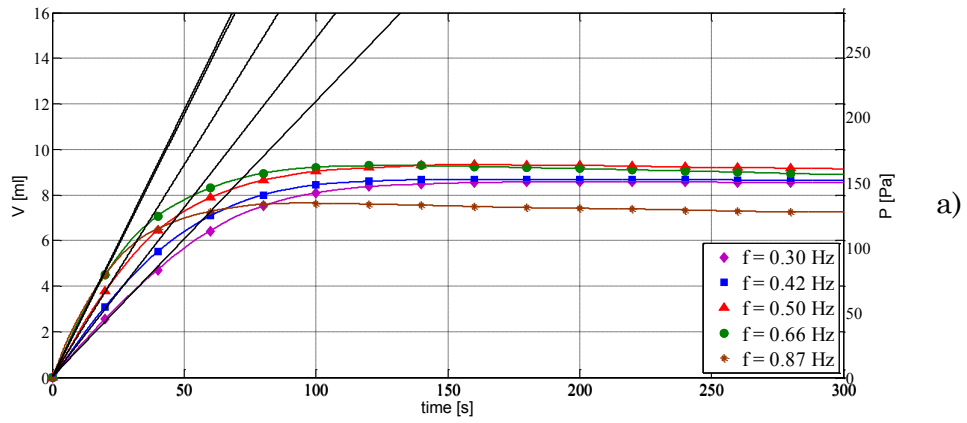
bias) and in Figure 4-11 (signals with superimposed bias) showing the amount of fluid accumulated into the outlet tank during the pump operation. This quantity can be easily converted to the pressure load produced by the accumulated fluid on the pump mechanisms (see the right axis of Figure 4-10 and Figure 4-11) with the following expression:

$$P = \rho gh \quad (4.5.)$$

Actually, these results represent the averaged values of several observations. The maximum residual observed between the different acquisitions of the liquid level pumped in the outlet tank, in the worst case, is of 0.3 mm which leads to an experimental contribution to the uncertainty of the handled volume estimation equal to 166.08  $\mu\text{l}$ .

As it can be observed, after an amount of operation time, the pump flow rate (given by the slope of the plotted curves) depends on the volume of fluid accumulated in the outlet tank (actually on the pressure load). Anyway, for this kind of pumps the operation range assuring a constant flow rate must be taken into account. This choice limits the range of operation up to a pressure threshold, defined as the value below which the flow rate is constant. The meaning of pressure threshold is evincible by the “slope line” in Figure 4-10 and Figure 4-11. The threshold pressure is defined as the pressure assuring a linear accumulation of the pumped volume.





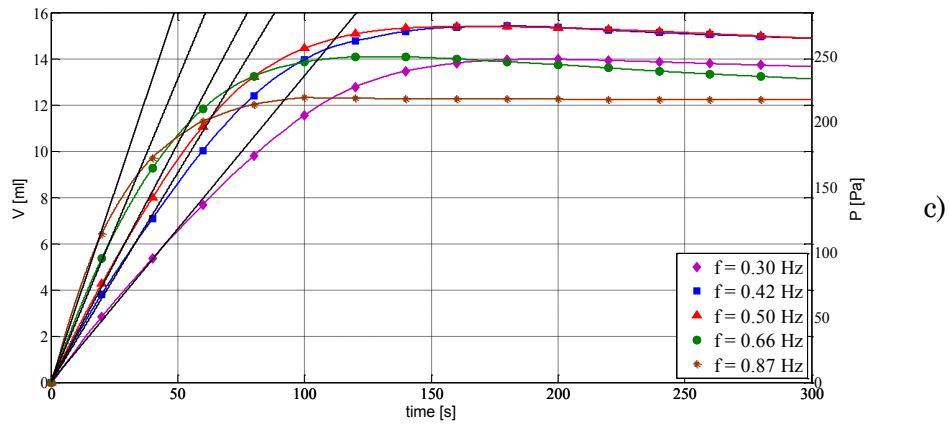
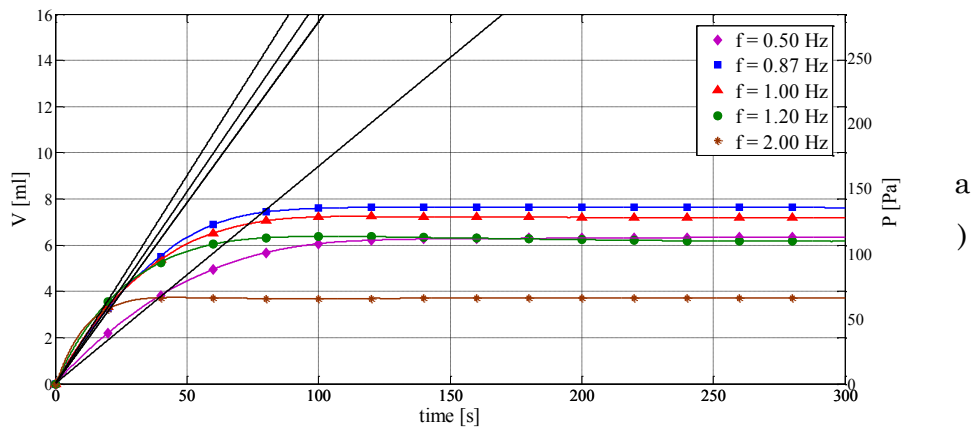


Figure 4-10 Results obtained through the device characterization procedure. The driving current has been fixed to: a) 300 *mApp*, b) 400 *mApp*, and c) 450 *mApp*.



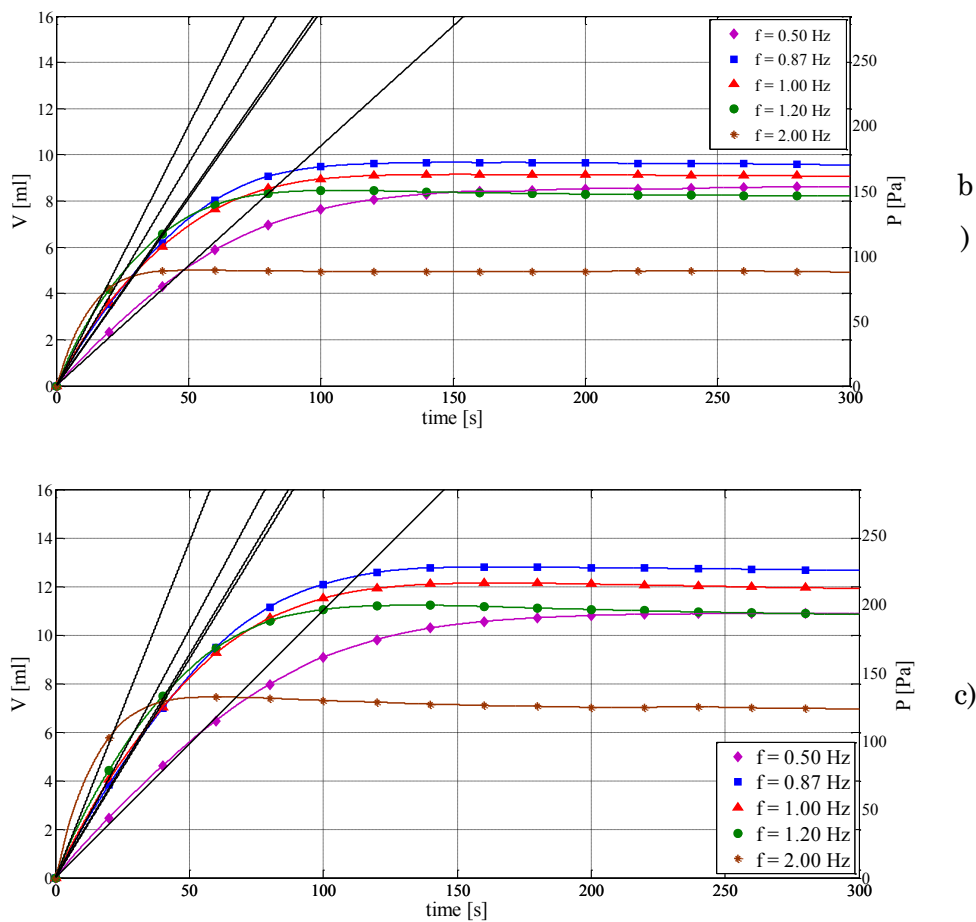


Figure 4-11 Results obtained through the device characterization procedure. The driving current has been fixed to: a)  $180 \text{ mApp} + 90 \text{ mAdc}$ , b)  $200 \text{ mApp} + 100 \text{ mAdc}$  and c)  $230 \text{ mApp} + 115 \text{ mAdc}$ .

In particular, in this operating range the flow rate increases with the frequency of the driving signals. It must be also observed that the pressure thresholds increases with the driving currents while it decreases with the frequency probably due to the sealing feature of the pumping mechanism which gets worse as the frequency increases.

All these results are summarized in Figure 4-12, showing the pressure threshold as a function of the flow rate for different value of amplitudes and frequencies of the driving currents. As can be observed the pressure threshold increases with the driving currents while it decreases with the frequency probably due to the sealing feature of the pumping mechanism which gets worse as the frequency increases.

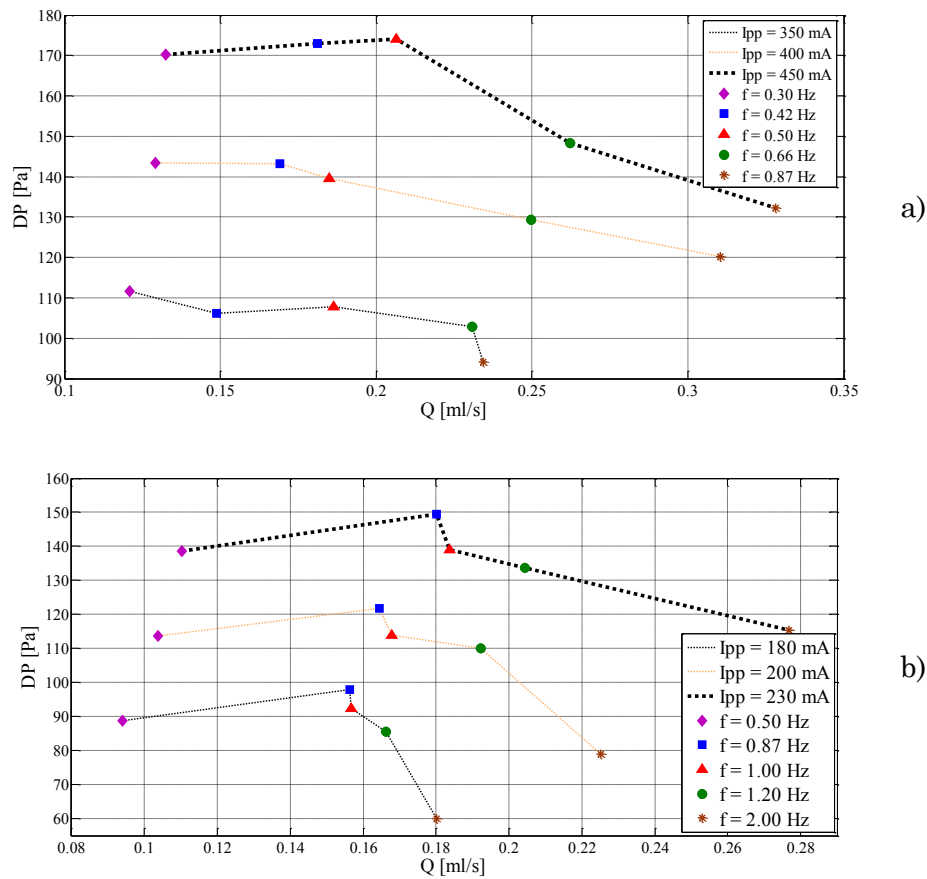


Figure 4-12 Threshold pressure and the corresponding pump flow rate as a function of the excitation current: a) signals without superimposed bias and b) signal with superimposed bias.

Figure 4-13 shows the maximum drop pressure as function of the driving frequency. The maximum drop pressure is the pressure value corresponding at the maximum pumped volume. It can be observed that the “cup sealing” is guaranteed approximately until 0.9 Hz when signals without superimposed bias are used, and until 2 Hz when driving signals have a superimposed bias.

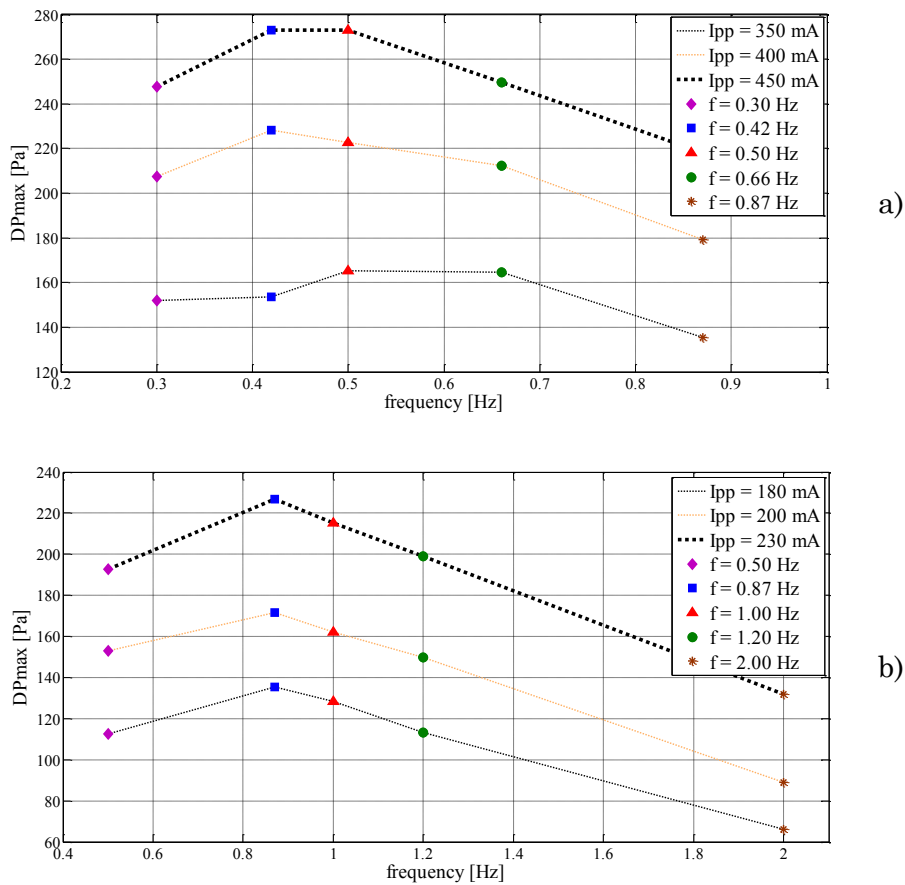


Figure 4-13 DPmax vs frequency: a) signals without superimposed bias and b) signals with superimposed bias.

In Figure 4-14 are shown results obtained in the absence of outlet tank for two different driving signals. Comparing such figure with Figure 4-11 it can be observed that in vacuum the flow rate is greatest because in this case the driving signals frequency is higher: it is due to a best sealing of the ferrofluid cup.

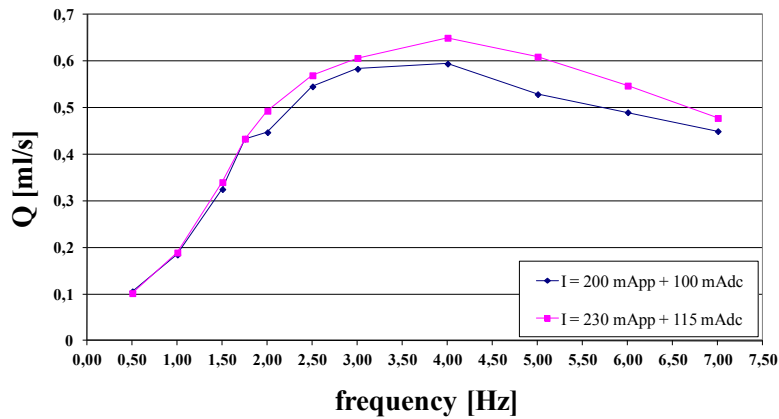


Figure 4-14 Amount of pumped liquid in vacuum.

A new set of experimental measures to estimate the average amount of pumped liquid and the maximum drop pressure for a different size of the outlet tank, was performed in the case of sinusoidal signals with a superimposed DC value. For these simulations a tank with a diameter of 15,45 mm was used; the corresponding resolution in the estimation of the pumped liquid volume is 18,75  $\mu\text{l}$ . Figure 4-15 shows the comparison between results obtained with the first tank and the second tank. As can be observed, the final pumped volume is different because

it depends on the tank diameter, while the maximum drop pressure is almost independent.

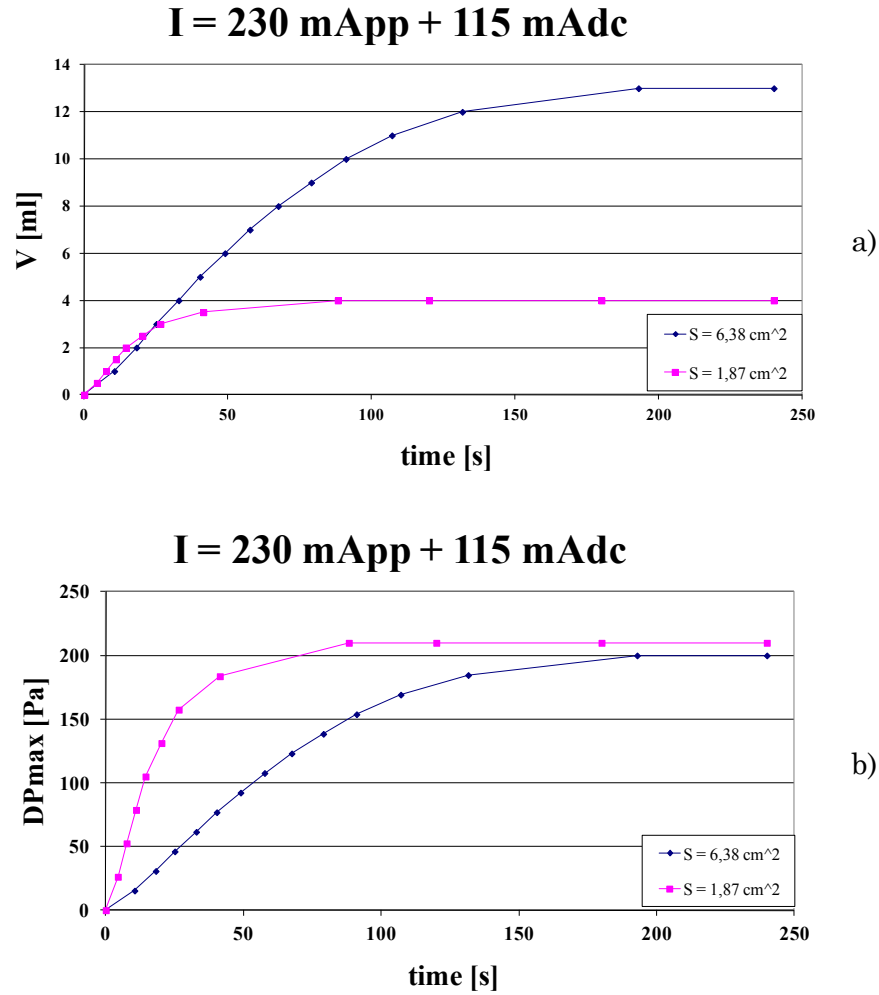


Figure 4-15 a) Average amount of pumped liquid for the two different tanks and b) maximum drop pressure for the two different tanks.

*An IR based methodology for the validation of the pumping mechanism*

The pumping mechanism described in the above section and schematized in Figure 4-2 (cap formation and propagation) has been supported by numerical simulations of models (Equations 4.1 and Equation 4.2) describing the interaction between the mass of ferrofluid and the magnetic forces. In this section a dedicated set-up, used to experimentally confirm the movement of the ferrofluid cap inside the channel during a typical pumping operation, is described.

Figure 4-16 shows the sensing architecture realized to observe the cap evolution inside the channel. In particular, a schematization of the device housing the IR (Infra Red) sensor array and a real view of the sensor array are given. The IR sensors adopted are the SFH3710 devices. The array is aligned with the electromagnets to assure one IR detector is positioned in each coil section. As shown in Figure 4-16, two light sources are positioned at the inlet/outlet sections of the channel thus allowing a quasi-uniform light propagation through the channel. In order to implement the optical readout strategy the pump set-up has been slightly modified as respect to the realization shown in Figure 4-1, by including two T connectors at the inlet and outlet sections allowing for light sources positioning without compromising the fluid management. The basic idea behind this experiment is to sense the light variation at each element of the sensing array (corresponding to each driving section of the pump) due to the cap formation at that element.

Signals coming from the sensor array are then conditioned by a dedicated electronic aimed at noise filtering and amplification. Manipulated signals are then conveyed to a data acquisition board connected to a PC



where an User Interface developed in LabVIEW® software has been used to manage signals and reconstruct the cap position during the pumping operation.

Initially, a test was performed to assess the operation of the sensing strategy adopted to sense the ferrofluid cap position inside the channel. In particular, a known ferrofluid mass was continuously moved back and forward inside the channel just by tilting the pipette filled with de-ionized water. The time evolution of signals coming from each sensor of the IR-led array during this experiment is shown in Figure 4-17a. Figure 4-17b and Figure 4-17c show the evolution of the ferrofluid mass from the left-hand side to the right-hand side of the channel.

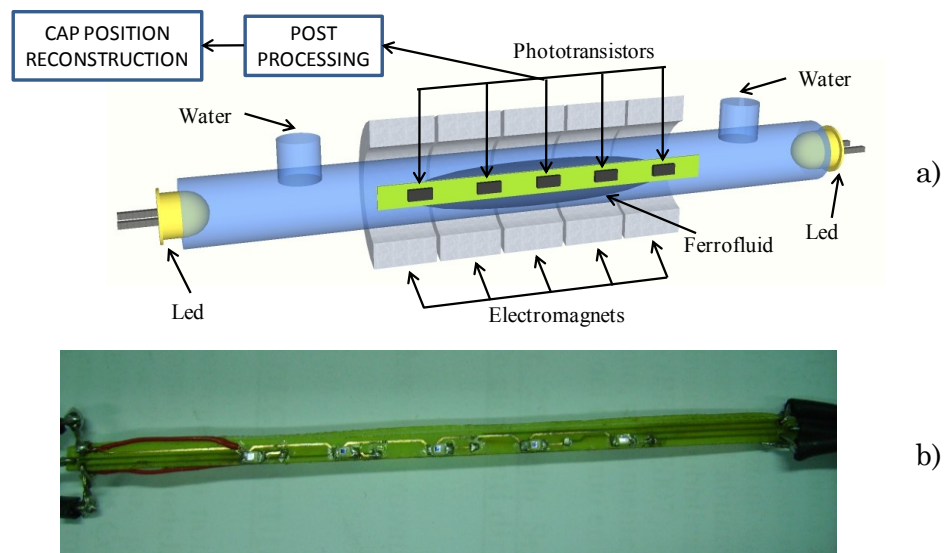


Figure 4-16 The sensing architecture realized to observe the cap evolution inside the channel. a) schematization of the device housing the IR sensor array; b) a real view of the IR sensor array.

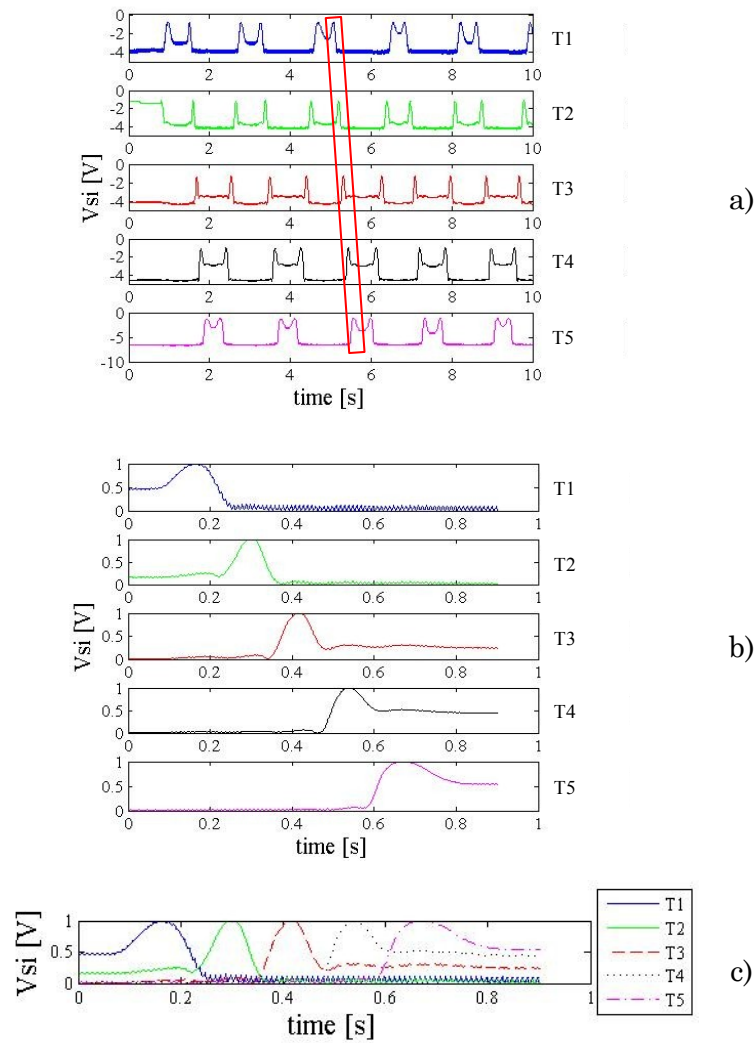


Figure 4-17 Time evolution of signals,  $V_{si}$ , coming from each sensor of the IR-led array during experiments assessing the operation of the sensing strategy adopted to sense the ferrofluid cap position inside the channel. a) the whole signal evolutions; b) a detail of a cap evolution from the left-hand side to the right-hand side of the actuation area, corresponding to the time interval highlighted in figure 4a; c) synthesis of the results shown in Figure 4-17b.

Signals recorded during the test evidence the proper operation of the developed sensing system and the suitability of the proposed methodology exploiting the ferrofluid opacity to produce significant light variation at the IR detectors.

A second set of tests has been implemented to reconstruct the cap movement inside the channel during a pumping session. Figure 4-18 shows the time evolution of signals coming from the IR-led array in the case of driving signals with amplitude and frequency of 200 mA (with a superimposed bias of 100 mAdc) and 0.6 Hz, respectively.

The observed cap position has been then compared with the expected movement of the ferrofluid mass. Results of this analysis are shown in Figure 4-19 for two different driving frequency, 0.6 Hz and 1 Hz.

As can be stated the observed trend represented by diagonal bands matches the expected behavior represented by solid lines. The diagonal bands are the observed cap movement and derive from the actual area covered by the ferrofluid mass, while the solid lines represent the expected cap movement under the hypothesis of a punctiform ferrofluid mass.

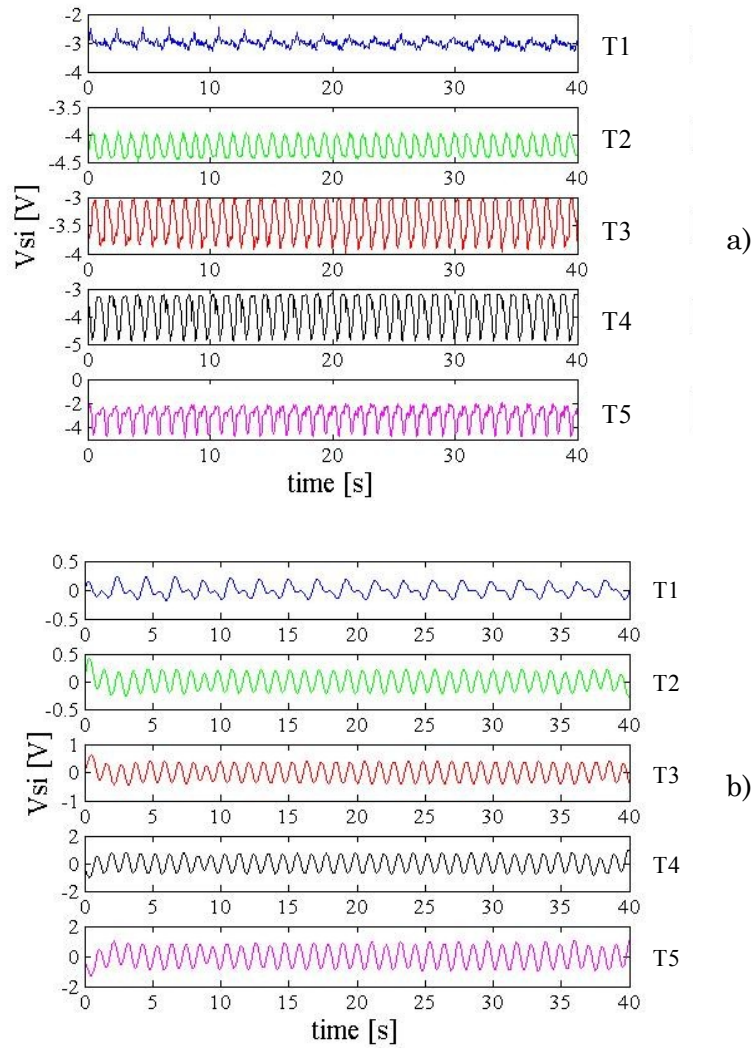


Figure 4-18 Time evolution of signals coming from the IR-led array during a pumping session. a) original signals and b) filtered signals. The driving signal parameters are:  $200\text{ mA} + 100\text{ mAdc} @ 0.6\text{ Hz}$ .

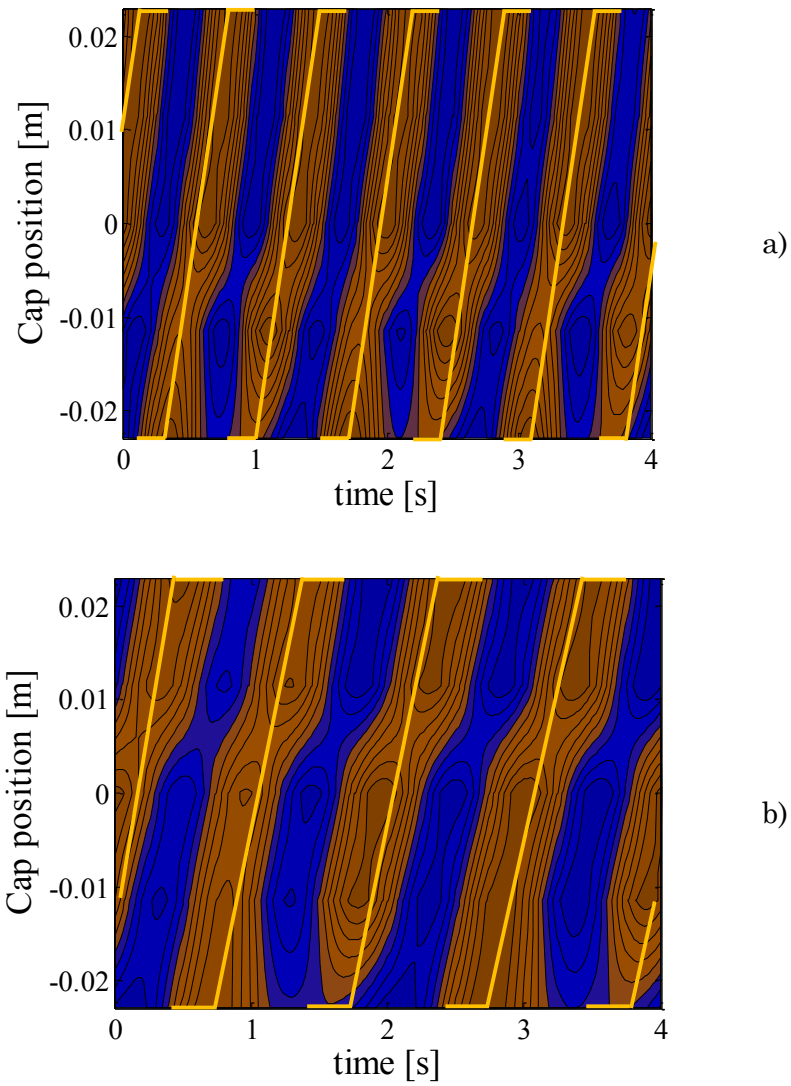


Figure 4-19 Observed evolution of the cap position during a pumping session (diagonal bands) and comparison with the theoretical trend (solid line) in Figure 4-6. Forcing signals parameters are: a)  $200\text{ mApp} + 100\text{ mAdc}$  @  $1\text{ Hz}$  and b)  $0.6\text{ Hz}$ .

## 4.2. Path Tracking of Ferrofluid Samples for Bio-sensing Applications

As previously wrote in Chapter 2, ferrofluids can be used in bio-applications as magnetic targets to link with biological molecules. Coating ferrofluid particles with biocompatible molecules allow to use them as markers to identify bio-entities, as schematized in Figure 4-20, in which the antigen is the molecule to identify and the antibodies are used only to link the antigen with the magnetic particle, that acts as marker. The main advantage of this form of labelling as compared to other techniques is related to the simple mechanisms to identify, to localize and to transport magnetic labelled entities. Actually, all these mechanisms are based on the use of magnetic fields which are also intrinsically penetrable into human tissue.

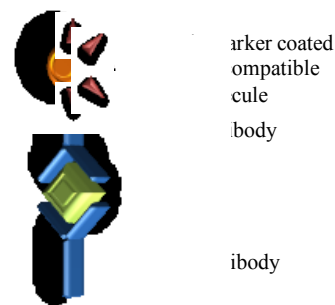


Figure 4-20 Schematization of the mechanism of magnetic labelling: the antigen is linked on the one hand with a capturing antibody and on the other hand with a detecting antibody, linked with the magnetic marker coated with a biocompatible molecule.

The magnetic particles, after the coating process, need to move to specific location inside a channel or inside the human body. Due to their magnetic nature, particles of ferrofluids can be controlled and moved by suitable magnetic fields.

In this section a convenient approach to move a ferrofluid mass along a pre-defined path is shown, together with some experimental results. In particular, the proposed methodology exploits a travelling magnetic field able to capture the bio-target linked to the magnetic beads and to move the sample along a pre-defined path consisting of a number of sites. Each site can be considered a stable position where the sample is subjected to chemical or thermal processes. The bio-sample to be managed is supposed immersed in a working fluid. As an example, such strategy could allow for bio-labeling and for the implementation of immune-assay tasks.

Although the working prototype developed is in the macro-scale, the proposed mechanism to track and process a bio-target sample linked to magnetic beads can be suitably down scaled.

Advantages of the use of ferrofluids in bio-applications are mainly related to their bio-compatibility. Other claims are the absence of moving mechanics which enables the system scaling down, the electric isolation between the liquid media (the bio-target and the magnetic beads) and the system electronics including the magnetic actuation devices, the physical decoupling between the device structure and the readout system, which allows to re-use the expensive part of the device (external electronics implementing the readout strategy) while the disposable part of the device, that is very cheap, can be replaced.

*The working principle*

The developed system is intended to demonstrate the possibility of moving a ferrofluid sample dispersed in a carrier liquid along a path defined by a number of sites. As previously mentioned, outcomes of such methodology could be the implementation of immune-assay techniques where the sample must be processed by different steps. As an example, in each site the bio-target conveyed by the magnetic mechanism can be subjected to a specific process (thermal or chemical).

The basic idea behind the proposed approach is the generation of a travelling magnetic field able to move the magnetic fluid sample across neighboring sites.

Figure 4-21a shows a matrix of sites where the ferrofluid sample can reside. Each site would represent one processing step for the bio-target linked to the ferrofluid carrier.

In order to create the mechanism to move the ferrofluid mass from one site to another site an array of actuation system, like the one shown in Figure 4-21b, was realized. Each actuation system consists in an electromagnet coupled to a permanent magnet.

Electromagnets are able to create both positive magnetic field (if driven by a positive current) and negative field (if driven by a negative current), while the permanent magnet creates an additive magnetic field.



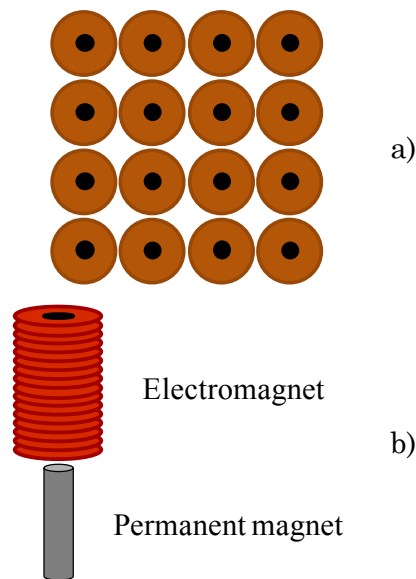


Figure 4-21 a) schematization of the matrix of the sites in which ferrofluid can be states and b) schematization of the magnetic actuation system.

The driving current amplitude must be able to null the magnetic field generated by the permanent magnet. Such choice will allow to switch the total magnetic field from a strong value (in case the two fields are in agreement) to an almost zero field (in case of opposite fields). In order to estimate the current value Equation 1.8 was used.

Figure 4-22 shows the sequence of operations allowing the transition of the ferrofluid sample from a site A to a site B. When the mass is in the site A, the A electromagnet is driven with a positive current and the resulting field is added to the field generated by the permanent magnet positioned in the A site; the B electromagnet is switched off. To move the mass from the A position to the B position, the A electromagnet is driven with a negative current in order to null the total magnetic

field in the A site while the B electromagnet is driven with a positive current. When the mass reaches the B position, the A electromagnet is turned off.

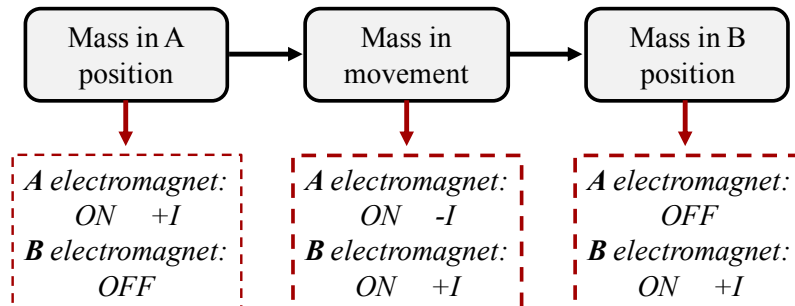


Figure 4-22 Block diagram of the sequence performed to move the mass from the A position to the B position.

### *The device*

The system consists of a matrix of sixteen magnetic actuators, a glass plate filled with de-ionized water and a drop of ferrofluid. Every electromagnet represents a possible stable position. Figure 4-23 is a picture of the prototype.

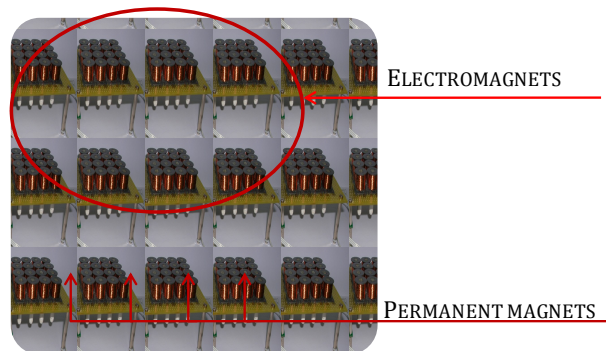


Figure 4-23 Real view of the realized prototype.

To force the actuation coil with a positive current or a negative current the half bridge configuration, shown in Figure 4-24, was used. The operation of the device is given in Table 4-2. When both Q1 and Q2 are off, no current flows in the electromagnet and no magnetic field is produced. When Q1 is on and Q2 is off a positive current flows in the electromagnet creating a positive field; when Q1 is off and Q2 is on, a negative current flows and the relative magnetic field is negative.

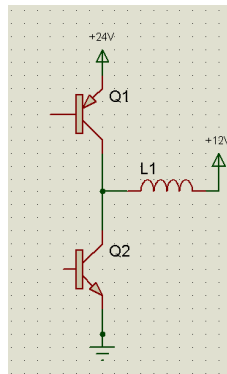


Figure 4-24 Scheme of the electronics.

Table 4-2 Operative conditions of the electromagnet as function of the desired current value.

| <b>Q1</b>  | <b>Q2</b>  | <b>I</b>     |
|------------|------------|--------------|
| <i>OFF</i> | <i>OFF</i> | <i>0</i>     |
| <i>ON</i>  | <i>OFF</i> | <i>&gt;0</i> |
| <i>OFF</i> | <i>ON</i>  | <i>&lt;0</i> |

*The GUI for path definition and tracking*

In order to define the path of the ferrofluid mass a Graphic User Interface (GUI) was developed in LabVIEW®. The status of each site is defined by a matrix of switches.

Two conditions are allowable, ON and OFF, which directly reflect on the electromagnet status. Sites in the ON status will be part of the established path. The interface allows to choose only adjacent sites; in order to define the path, electromagnets have to be chosen in the same sequence in which they must be activated. If a wrong electromagnet is chosen (because it isn't adjacent with the previous one) a warning message appears. The interface gives also the possibility to establish if the ferrofluid mass has to moves in a continuous cycle or if it has to stop after a single path. It is also possible to choose the residence time during which the mass remains in each site. An array of led highlights which electromagnet is active and which half bridge is turned on. The developed GUI interface is shown in Figure 4-25.

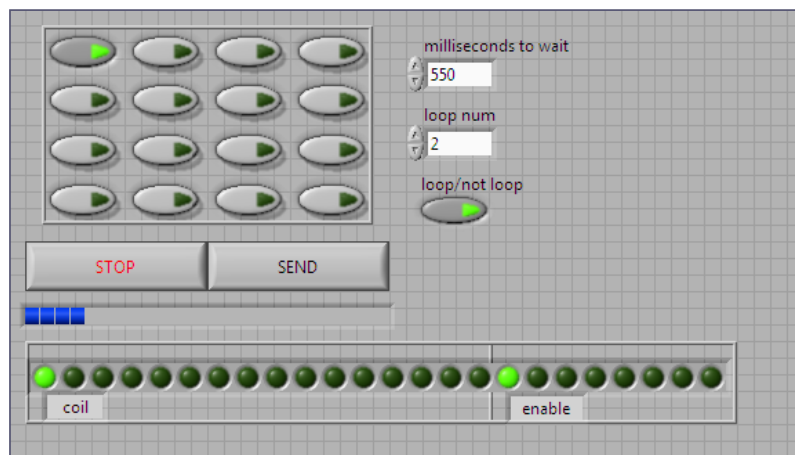


Figure 4-25 A picture of the realized interface in Labview® software.

*The experimental results*

Figure 4-26 shows frames of a video in which a ferrofluid mass follows a path established through the developed interface.

A set of experiments was performed in order to establish the minimum time step allowing the ferrofluid mass transition between two adjacent sites. A ferrofluid mass of 0.1 ml was used to perform this experiment. The time step was increased from 250ms up to 2000ms and several measures for each time step were performed.

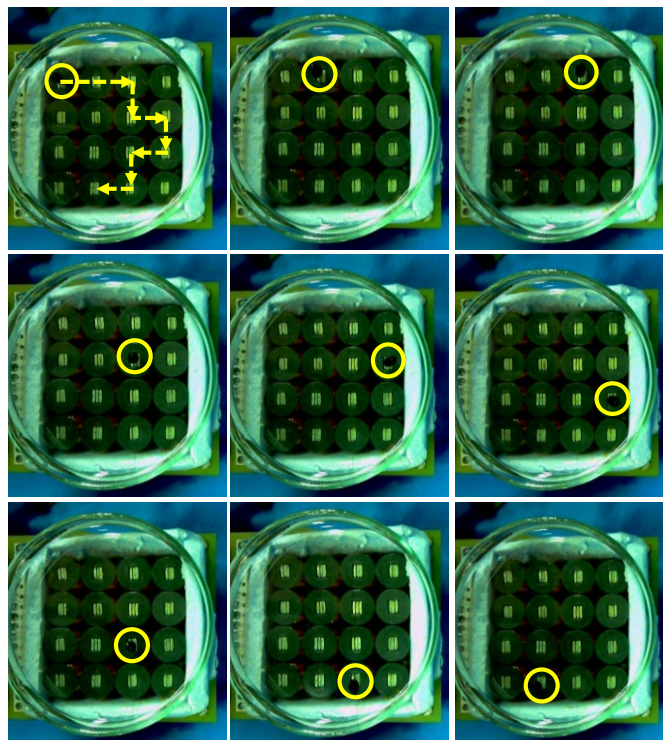


Figure 4-26 Frames of a video showing the movement of the ferrofluid mass along a pre-defined path.

When the time step is too low, the ferrofluid mass is not always able to follow the defined path. This phenomena is evincible from results shown in Figure 8. As it can be observed for a time step less than 500 ms the system is not always able to follow the selected path. Experiments performed for time step higher than 500 ms show the repeatability of the developed system.

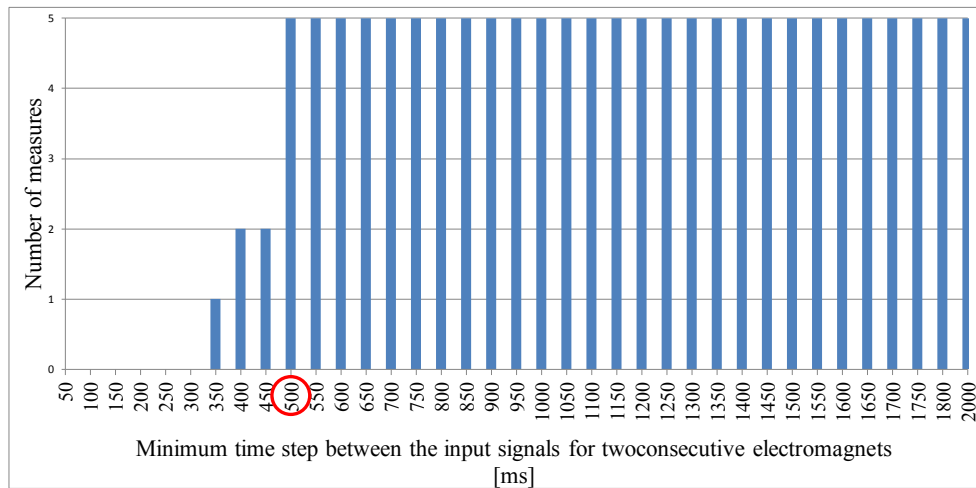


Figure 4-27 Number of successful transitions between two adjacent positions vs minimum time step between the input signal for two consecutive electromagnets.

# Chapter 5

## *TOWARDS INTEGRATED MICROFLUID MAGNETIC DEVICES*

As evidenced in the Introduction, the advantages related to micro-systems integrating both the sensing structures and the fluidic part are various: the possibility to have a portable device to make measure in different environments, the low cost related to the low amount of raw materials and the low power budget, are only some characteristics of such structures.

In Chapters 3 and 4 it has been demonstrated as it is possible to use ferrofluids both to realize sensing devices and to implement actuators useful for the fluidic system. Consequently, ferrofluids can be used to realize complex systems including the sensors and the fluidic part. As mentioned before, the use of ferrofluids confers to the devices numerous

advantages as the opportunity to control the device specifications by manipulating the ferrofluid mass properties by imposing magnetic fields, the high reliability and robustness against shock, the reusability of the expensive part of the device and the low cost due to the very small amount of ferrofluid used as inertial mass.

In the following sections two different structures are presented as examples of realization of systems integrating the sensing part and the fluidic part.

### **5.1. An integrated device for biological measurements**

In the modern research the realization of biosensors for applications in different fields like public health, clinical analysis, water and air pollution, biotechnology holds an important position. For such devices a very high sensitivity and specificity, a short analysis time, low cost, easiness to handle, capability for portable applications are of fundamental importance.

Biosensors with high sensitivity and specificity can be obtained by using Immunoassay techniques [38], [39], whose working principle is schematized in Figure 4-20. By comparison with the others, magnetic markers have potential advantages, due to their low price, very high stability and absence of toxicity. In addition, bio-molecules fixed to magnetic nano-particles can be easily localized and manipulated by suitable magnetic fields [40]. The problem of detecting biological agents is therefore shifted to the ability of sensing the presence of the chosen marker and, in particular, referring to the magnetic markers the issue arising concerns the possibility of detecting the weak magnetic field, or



perturbation to an externally applied magnetic field, due to the presence of a small number of particles having magnetic properties.

In the following sections an example of integrated system for biological measurement is shown. In this structures ferrofluids are used both to implement the fluidic part and as magnetic marker in order to realize the Immunoassay technique.

#### *The device architecture*

The first step consists in the realization of the links between the ferrofluid particle, the antibody and the antigen to identify, as schematized in Figure 4-20.

A scheme of the proposed structure is reported in Figure 5-1. The functionalized magnetic beads and the fluid sample containing the analyte bounded to the antibodies, are driven into the "mixing chamber" to realize the antibody-antigene binding. This agglomerate is driven to the "sensing chamber" by a valve-pump system. If the chambers are pre-loaded or, a positive pressure difference is applied, valves can be single-use because the sample goes from the "mixing chamber" to the "sensing chamber"; otherwise a volumetric pumping mechanism can be adopted to move the fluid to the "sensing chamber" without the need of valves.

The inductive sensor will be placed on the bottom of the "sensing chamber" and here the immunoassay mechanism will be completed by the binding of the functionalized magnetic beads to the receptors over the active sensor surface to complete the sandwich shown in Figure 4-20. In the "sensing chamber" the above described sensor reveals the amount of the molecule to detect.

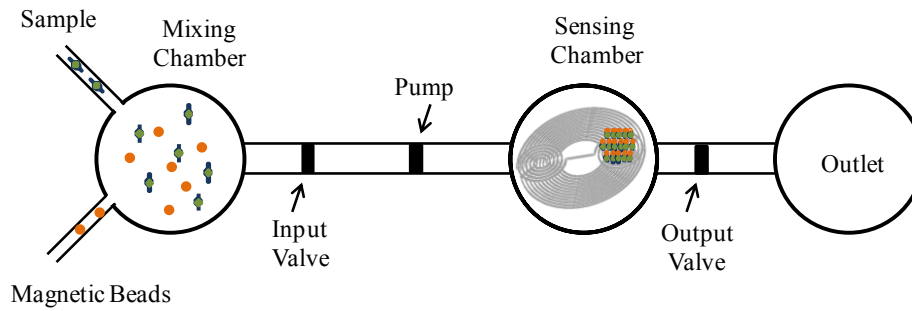


Figure 5-1 The functional block scheme of the lab on chip system embedding the inductive sensor for magnetic beads.

Both the valves and the pump can be realized using ferrofluids and an actuation system made by electromagnets, as shown in the previous chapter.

#### *The magnetic sensor*

Several different works have been presented in the scientific literature which deal with the problem of detecting the presence of magnetic markers into a selected area, [41], [42]: in these sensors the inductance value changes as a function of a certain density of magnetic particles in the active region of the sensor device.

First the active region must be functionalized, very often silanized, to allow the binding of the antibody over the sensor surface; then both the active region and the magnetic particles must be functionalized with an antibody specific to the analyte to be detected. The interaction antibody-analyte-antibody binds the magnetic particles to the sensor surface. If a magnetic field source is considered, the distribution of the magnetic flux lines will be affected by the presence of a number of mag-

netic particles, this in turn induces a change in the inductive impedance of the coil placed in the active area of the sensor. In comparison with other kinds of magnetic biosensors, inductive devices have several potential advantages, which are related to their higher simplicity, fully compatibility with standard Si technology materials, low cost and higher flexibility.

The device presented is based on a planar coreless differential transformer configuration [43], [44], [45]. A primary coil generates a magnetic flux which links with two secondary coils, having opposite winding sense, connected in a differential arrangement, as shown in Figure 5-2.

The primary coil generates a magnetic flux that therefore induces voltages with equal values but opposite in sign in the secondary coils, due to their opposite winding sense and the symmetry properties of the device; therefore the resulting output voltage, which is the difference between the voltages across the secondary coils, is zero when no magnetic particles are present. On the other hand, the presence of magnetic particles in one of the secondary coils will cause an increase of the magnetic field density on an area close to the magnetic particles; in this way, the output voltage will be non-zero in fact the voltages induced into the two secondary windings will not be equal anymore.

In the proposed device only the secondary coil over which the magnetic particles are placed, acts as the "active" sensor, while the other one acts as "dummy", like in most differential sensing approaches. In particular here the differential configuration is used not to enhance sensitivity; in fact there are no opposite variations of inductance, but to lower the noise floor. In fact any unwanted external excitation will af-

fect the two secondary coils at the same manner and therefore will be nulled by the differential arrangement, while only the signal produced by the magnetic markers placed over one of the two coils will be useful for a non zero output voltage. The primary coil is a source of excitation of the sensor.

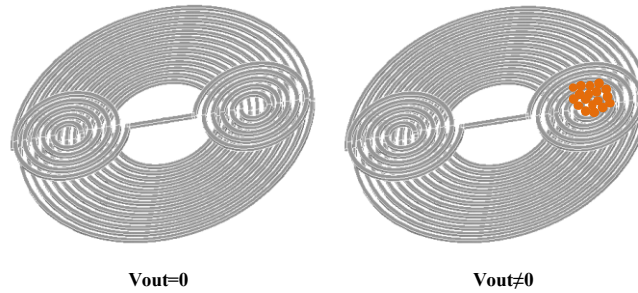


Figure 5-2 Working principle of the planar differential transformer.

This approach allows a more flexible optimization of the device in terms of sensitivity; in fact in the case in which the primary coil is current driven and the secondary coil has an infinite impedance, the open circuit voltage at the secondary coil, if expressed in terms of the current applied to the primary winding, is proportional to the product of the number of turns of the primary and the secondary coils as reported in Equation 5.1.

$$S = N_1 N_2 \frac{2R_1 + R_2}{\left[ R_1 \left( 2 - \frac{\Delta L}{L_1} \right) + R_2 \left( 1 - \frac{\Delta L}{L_2} \right) \right]^2} \frac{di_1}{dt} \quad (5.1)$$

Where  $N_1$  and  $N_2$  are the number of turns respectively of the primary and each secondary coils,  $R_1$  and  $R_2$  are the reluctances of primary and secondary coils,  $i_1$  is the current in the primary coil,  $\Delta L$  is the dif-

ference of inductance of the secondary coil over which the magnetic beads are (such variation is due to the thickening of magnetic field),  $L'_2$  is the inductance value of the secondary coil over which the magnetic beads are.

While the secondary coils can be subjected to more restrictive design constraints due to their sensing function, the primary coils has less restrictions, therefore both the sensitivity requirements and the design constraints can be more easily satisfied with respect to the single inductor case, by proper designing the primary and secondary coils.

Furthermore, the approach presented here is intrinsically differential, thus allowing a better rejection of noise and interferences. It is suitable for the integration in Si technology due to its simple and planar geometry.

Moreover, it is not based on the direct estimation of the inductance, resulting in a great simplification of the measurement strategy. In fact the magnetic particles act as a moveable nucleus and the differential output voltage at the secondary coils is directly related to the number (or density) of magnetic particles. Therefore a high impedance detection of the differential output voltage at the secondary coils is a simple but good strategy to the detection of the magnetic particles.

Simulations were performed in ANSYS® software in order to verify the change of the magnetic field density due to the presence of the magnetic particles on the active area of the differential device. The simulated differential transformer is made up of two metal layers (Metal 1 and Metal 2) separated by a layer of silicon oxide. The primary winding has been realized in the Metal 1 layer, while the Metal 2 layer has been used to realize the secondary windings. A passivation layer covers the

whole transformer. Figure 5-3 shows a schematics of the cross section of the device: the primary and secondary centers are indicated by vertical axis.

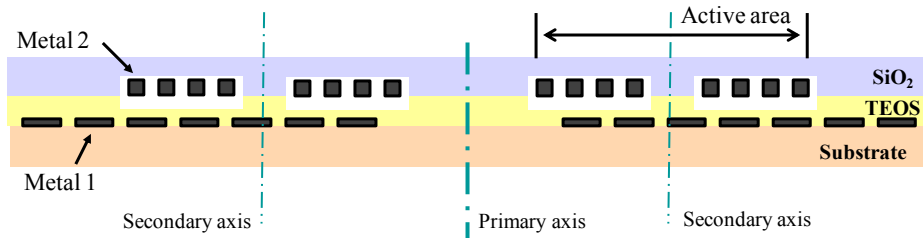


Figure 5-3 Schematic of the cross-section along a radial direction.

The geometric characteristics of the simulated transformer are reported in Table 5-1.

Table 5-1 Geometric characteristics of differential transformer.

| <i>Geometrical parameters</i>                     | <i>Values</i>                       |
|---|-------------------------------------|
| <i>Metal1 thickness</i>                           | <i>0.5 <math>\mu\text{m}</math></i> |
| <i>Minimum track spacing and width for Metal1</i> | <i>1 <math>\mu\text{m}</math></i>   |
| <i>Oxide thickness</i>                            | <i>1 <math>\mu\text{m}</math></i>   |
| <i>Metal2 thickness</i>                           | <i>1 <math>\mu\text{m}</math></i>   |
| <i>Minimum track spacing and width for Metal2</i> | <i>1.2 <math>\mu\text{m}</math></i> |
| <i>Passivation thickness</i>                      | <i>0.5 <math>\mu\text{m}</math></i> |

The magnetic beads in the sensing area of the active secondary coil attract the magnetic flux lines and change the magnetic field distribution by creating a thickening zone, as shown in Figure 5-4.

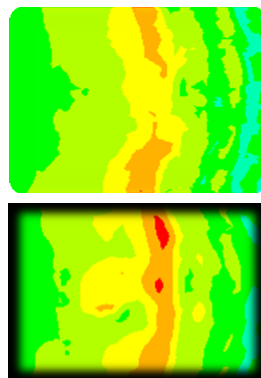
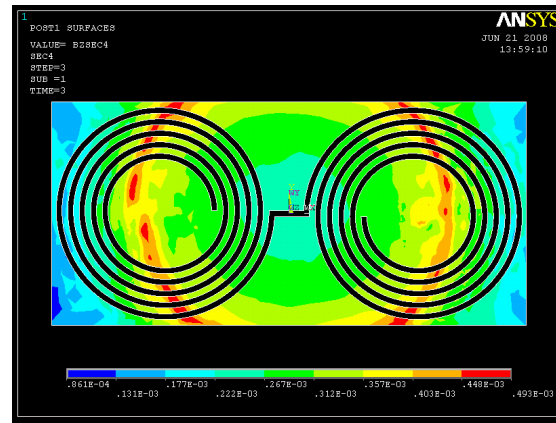


Figure 5-4 Distribution of the magnetic field produced by the primary coil and view of the secondary coils (top). Zoom of the area inside the active coil (the one at the right in the top figure) both in absence -picture b) on the top side- and in presence -picture b) in the bottom side- of magnetic beads.

Simulations have been performed to determine the influence of the different device parameters (as number of rings, separation between rings, active surface dimension, position of secondary centre, etc) on the sensor response.

Table 5-2 Optimized inductive microsensor parameters.

|                                  |   |
|----------------------------------|---|
| <b>Primary coil</b>              | <i>Turns number 13</i>                                  |
|                                  | <i>Track width 2.5 <math>\mu\text{m}</math></i>         |
|                                  | <i>Spacing 1 <math>\mu\text{m}</math></i>               |
|                                  | <i>Inner radius 9 <math>\mu\text{m}</math></i>          |
| <b>Secondary coil</b>            | <i>Turns number 5</i>                                   |
|                                  | <i>Track width 1.2 <math>\mu\text{m}</math></i>         |
|                                  | <i>Spacing 1.2 <math>\mu\text{m}</math></i>             |
|                                  | <i>Inner radius <math>\leq 3 \mu\text{m}</math></i>     |
| <b>Radius of the active area</b> | <i>Centers position <math>\pm 18 \mu\text{m}</math></i> |
|                                  | <i>3.6 <math>\mu\text{m}</math></i>                     |

Layouts of the differential inductive sensor were designed starting from the simulation results; test devices were realized using the dedicated technology developed in cooperation with the STMicroelectronics of Catania (Italy) and shown in Figure 5-5.

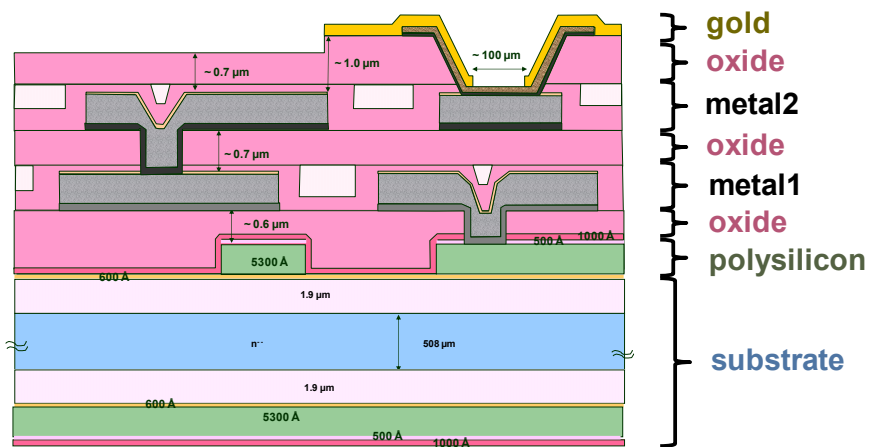


Figure 5-5 The dedicated technology used to realize the differential inductive sensor.



Experimental measurements were performed in order to validate the working principle of the realized devices. Several concentration of magnetic particles were deposited on the active area of the secondary coils; pictures of the depositions are reported in Figure 5-6.

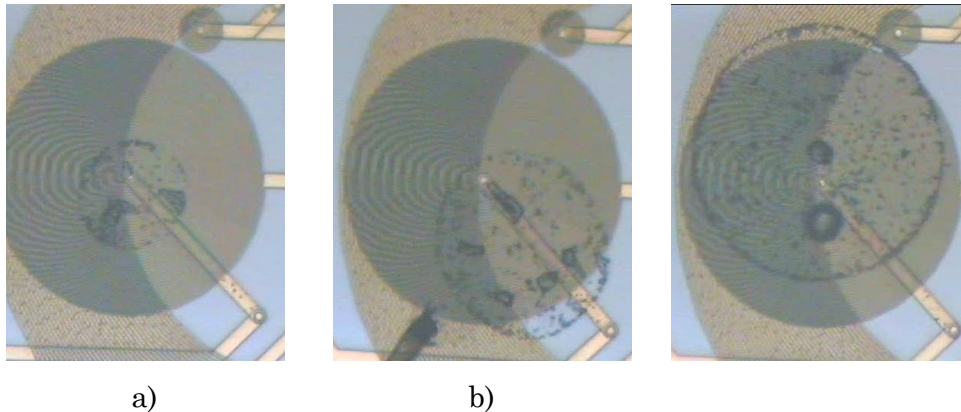


Figure 5-6 Pictures of the active secondary coil with different deposition of magnetic particles: a) quantity  $Q_1$ ; b) quantity  $Q_2=2*Q_1$  and c) quantity  $Q_3=10*Q_1$ .

Results are shown in Figure 5-7, where it is evincible as the sensor output depends on the amount of magnetic particles deposited in the active area. For each amount of magnetic particles twenty sets of measures were performed; Figure 5-7 shows the output voltage obtained during the measurement: lines represent the mean value related to a set of measure, while each blue circle represents a single acquisition of the sensor output voltage without deposited magnetic particles.

The mean value of the output voltage as function of the amount of the magnetic particles is shown in Figure 5-8.

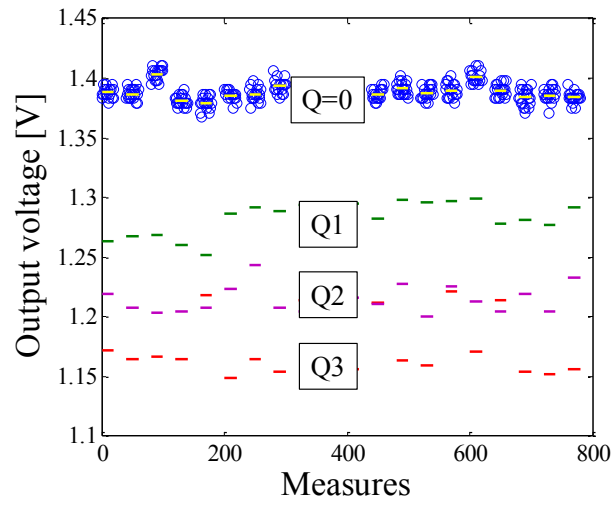


Figure 5-7 Sensor output voltage with different amount of deposited magnetic particles.

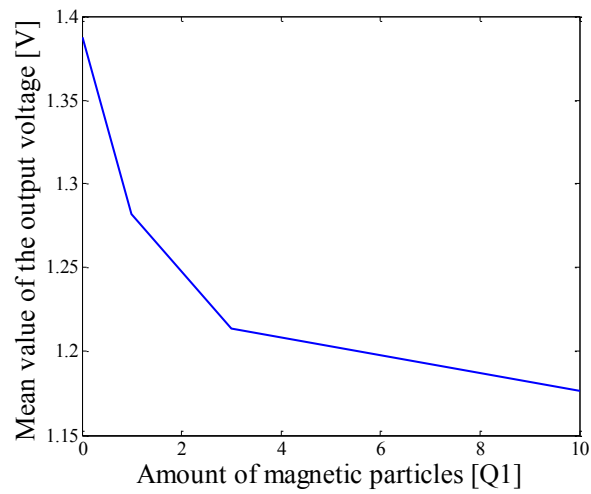


Figure 5-8 Mean value of the sensor output as function of the magnetic particles amount.

## 5.2. A multi-sensing structure for inertial measurements

The second example is a structure in which ferrofluids are used both as inertial mass in the sensing devices and as valves and plungers in the fluidic system; it can be schematized as in Figure 5-9.

The system is made by several chambers, each of which contains an inertial sensor (such as a gyroscope, a displacement sensor, an acceleration sensor), a pipe filled with a liquid, and several rooms of rest for the ferrofluid masses. The sensors in the chambers utilize a ferrofluid mass as inertial mass; to avoid adhesions between the mass and the faces of the chambers, the masses of the sensors are removed from the active area and are kept in the primary room of rest. A dedicated actuation system moves the mass from this room to a chamber depending on the kind of measures to perform. After the measures, the mass returns to its steady position in the room of rest.

Moreover, making several rooms of rest it is possible to move different amounts of ferrofluid masses in the sensor chamber; the response of a ferrofluid sensor depends on the amount of the ferrofluid mass used as inertial mass; changing the ferrofluid quantity it is possible to adapt the sensor parameters, as resolution, sensitivity and operative range, to the particular case in exam.

When a sensor is not used, its open is closed by a ferrofluid mass acting as a valve, as shown in Figure 5-9, where only the Sensor 3 is working. In fact, when a sensor has to be used an actuation system moves the mass in the relative secondary room of rest, making free the access of the sensor to the ferrofluid that will act as the inertial mass of the sensor. After the measurement, when the working sensor has to be

switched off, the active mass is moved in the primary room and the access is closed by the mass stored in the relative secondary room.

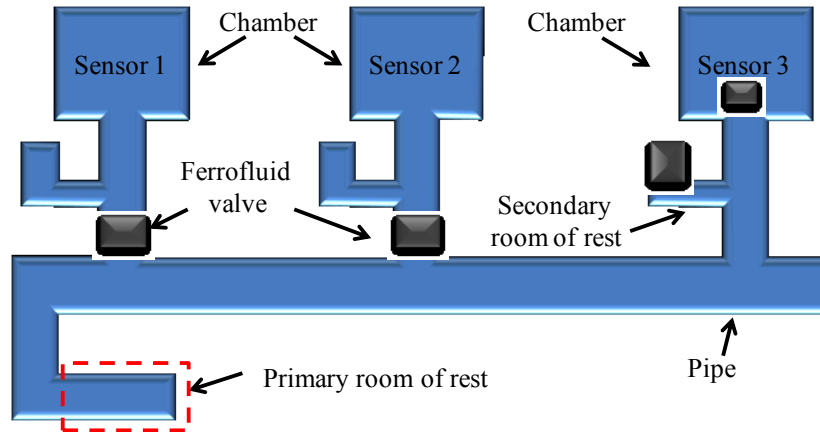


Figure 5-9 Schematization of the multi-sensing structure.

The multi-sensing structure shown in this section presents all the advantages related to the use of ferrofluid as inertial mass and, in addition, it can be used to make different measures using the same mass of ferrofluid and the same actuation system, reducing in this way the cost of realization. Moreover, scaling down the size of the sensors, it is possible to realize a portable structure to use, for example, in hostile environments.

## *Conclusions*

An important field of research for modern scientists is the study and realization of innovative materials and sensing strategies in order to realize devices with high performances and tunable characteristics.

In addition, the possibility to integrate in the same chip several sections each one implementing different basic operations, allows to conceive single device performing a complex process of measure.

This Thesis points out to the potentiality of magnetic fluids to realize the several constitutive parts of an integrated structure. In fact, ferrofluids can be successfully used both in sensors and in actuation system, as demonstrated in this work.

The use of a ferrofluid mass as inertial mass in the developed sensors gives the possibility to control the device specifications through appropriate magnetic fields generated by permanent magnets or electromag-

nets. In addition, other advantages are related to the use of ferrofluids: low cost, decoupling between the device structure and the readout system, the robustness against mechanical shock are only some of the characteristics of the ferrofluid sensors.

In Chapter 3 developed sensors have been shown, together with the theoretical model and the experimental characterization.

Magnetic fluids can be also used to implement a fluidic system made by valves and plungers, controlled by suitable magnetic fields. In Chapter 4 actuation systems able to control ferrofluid mass in order to open/close channels, to move fluids from an inlet tank to an outlet tank, or able to control the mass movement along a pre-defined path, are reported together with the experimental results.

All the proposed methodologies are realization and characterization of laboratory prototypes.

As final effort, in Chapter 5 the convergence of all the concepts developed in the area of both sensors and actuators toward the implementation of two complex structures, in which ferrofluids are used at the same time as core component in the sensing part and in the fluidic part, have been discussed. Two specific applications have been addressed: a multi-sensorial system and a device for biomedical applications.

## *References*

- [1] F D. D. Pollock, *"Physics of Engineering Materials"*, Prentice-Hall, Inc., Englewood Cliffs, NJ.
- [2] G. Antonie van Ewijk, *"Phase behavior of mixtures of magnetic colloids and non-adsorbing polymer"*, Phd thesis Utrecht University.
- [3] E. L. Jr. Resler and R. E. Rosensweig, *"Magnetocaloric power"*. AIAA J., 2, 8 pp. 1418, 1964.
- [4] S. S. Papell, U.S. Patent n° 3, 215, 572 (1965).
- [5] R. E. Rosensweig, *"Ferrohydrodynamics"*, Cambridge Univ. Press, New York, 1985.

- [6] G. S. W. Charles, "The preparation of magnetic fluids", in: S. Odenbach (Editor), *"Ferrofluids: Magnetically controllable fluids and their applications"*, Lecture Notes in Physics, Springer-Verlag, pp.3-18, 2002.
- [7] J. Popplewell, R E Rosensweig. *"Magnetorheological fluid composites"*, J. Phys. D, Appl. Phys.1996; 29, p. 2297-2303.
- [8] Yu. I. Dikanskii and O. A. Nechaev, *"Magnetic Fluid Structural Transformations in Electric and Magnetic Field"*, Colloid Journal, Vol. 65, No. 3, pp. 305–330, 2003.
- [9] Raj K et al, *"Commercial applications of ferrofluids"*, Journal of Magnetism and Magnetic Materials, Vol. 85, No. 1-3, pp. 233–245, 1990.
- [10] M. T. Thompson, *"Simple Models and measurement of magnetically induced heating effects in ferromagnetic fluids"*, IEEE Transaction on magnetic, Vol. 34, No. 5, September 1998.
- [11] Q. A. Pankhurst, J Connolly, S K Jones and J Dobson, *"Applications of magnetic nanoparticles in biomedicine"*, Journal of Physics D: Applied Physics, Vol.36, No.13, pp167–181, 2003.
- [12] B. Y Kularatne, P Lorigan, S Browne, S K Suvarna, M O Smith and J Lawry, *"Monitoring tumour cells in the peripheral blood of small cell lung cancer patients"*, Cytometry, Vol.50, No.3, pp.160–167, 2002.
- [13] R. S Molday and D MacKenzie, *"Immunospecific ferromagnetic iron–dextran reagents for the labeling and magnetic separation of"*



- cells*”, Journal of Immunological Methods, Vol.52, No.3, pp.353–367, 1982.
- [14] R. E Zigeuner, R Riesenberger, H Pohla, A Hofstetter and R Oberneder, “*Isolation of circulating cancer cells from whole blood by immunomagnetic cell enrichment and unenriched immunocytochemistry in vitro*”, The Journal of urology, Vol.169, No.2, pp.701–705, 2003.
- [15] F. Gazeau, C Baravian, J C Bacri, R Perzynski & M I Shliomis, “*Energy conversion in ferrofluids: Magnetic nanoparticles as motors and generators*”. Physical Review E, Vol. 56, No. 1, pp. 614–618, 1997.
- [16] B. Andò B, A. Ascia A, S. Baglio, N. Pitrone, “*Magnetic fluids and their use in transducers*”. IEEE Magazine on Instrumentation and Measurements, Vol. 9, No. 6, pp.44-47, 2006.
- [17] R. Perez-Castillejos, J A Plaza, J Esteve, P Losantos, M C Acero, C Cane, F Serra-Mestres, “*The use of ferrofluids in micromechanics*”, Sensors and Actuators, Vol.84, No.1-2, pp.176–180, 2000.
- [18] G. Q. Hu, W. H. Liao, “*A feasibility study of a microaccelerometer with magnetorheological fluids*”, Proceedings of the 2003 IEEE International Conference on Robotics, Intelligent System and Signal Processing, China, pp.825-830, October 2003.
- [19] R. Olaru, D. D. Dragoi, “*Inductive tilt sensor with magnets and magnetic fluid*”, Sensor and actuators A, Elsevier, Vol. 120, pp. 424-428, February 2005.

- [20] O. Baltag, D Costandache, , “*Sensor with ferrofluid for magnetic measurements*”, IEEE Transaction on instrumentation and measurement, Vol.46, No.2, pp.629-631, 1997.
- [21] D. Zhang, Z. Di, Y. Zou, X. Chen, “*Temperature sensor using ferrofluid thin film*”, Microfluid Nanofluid, Vol.7, pp.141–144, 2009.
- [22] N. E Greivell, B. Hannaford, “*The design of ferrofluid magnetic pipette*”, IEEE Transactions on Biomedical Engineering, Vol.44, No.3, pp.129-135, 1997.
- [23] A. Hatch, A E Kamholz, G Holman, P Yager and K F Böhringer, “*A Ferrofluidic Magnetic Micropump*”, Journal Of Microelectromechanical Systems, Vol.10, No.2, pp.215-221, 2001.
- [24] J. Joung, J Shen, and P Grodzinski, “*Micropumps Based on Alternating High-Gradient Magnetic Fields*”, IEEE transactions on magnetics, Vol.36, No.4, pp. 2012-2014, 2000.
- [25] M. Zahn, L L Pioch, “*Ferrofluid flows in AC and travelling wave magnetic fields with effective positive, zero or negative dynamic viscosity*”, Journal of magnetism and magnetic materials, Vol.201, No7, pp.144–148,1999.
- [26] B. Andò, S. Baglio, A. Beninato, “*Behavior Analysis of a Ferrofluidic Gyroscope Performances*”, Proceedings of the Eurosensors XXIII conference, Volume 1, No 1, September 2009, Pages 116-119.
- [27] B. Andò, S. Baglio, A. Beninato, “*Behavior Analysis of Ferrofluidic Gyroscope Performances*”, Sensors and Actuators A: Physical, Vol. 162, No 2, pp. 348-354, 2010.

- [28] B. Andò, S. Baglio, A. Beninato, “*A inertial sensor exploiting a spike shaped ferrofluid*”, Instrumentation and Measurement Technology Conference (I2MTC), 2011 IEEE, pp. 1 – 5, 2011
- [29] B. Andò, S. Baglio, A. Beninato , “*A low cost inertial sensor based on shaped magnetic fluids*”, IEEE Transactions on Instrumentation and Measurement, in press.
- [30] B. Andò, S. Baglio, A. Beninato, “*A flow sensor exploiting magnetic fluids*”, Proc. Eurosensors XXV, Athens, Greece, September 4-7, 2011.
- [31] B. Ando, A Ascia, S. Baglio, N. Savalli, “*A Novel Ferrofluidic Incliniometer*”, IEEE Transactions on Instrumentation and Measurement, Vol. 56, No 4, pp. 1114-1123, August 2007.
- [32] B. Ando, A Ascia, S. Baglio, C. Trigona, “*Resonant Ferrofluidic Incliniometers*”, Proceeding of IEEE Sensors, pp. 776-779, 2007.
- [33] B. Andò, A. Ascia, S. Baglio, N. Pitrone, “*Development of a pump with a single ferrofluidic mass*”, Eurosensors conference, 2008.
- [34] B. Andò, A. Ascia, S. Baglio, A. Beninato, “*The “One drop” Ferrofluidic Pump with Analog control: “FP1\_A”*”, Sensors & Actuators: A. Physical, Vol. 156, No. 1, pp. 251-256, 2009.
- [35] B. Ando’, S. Baglio, A. Beninato, “*A Novel Non-invasive Implementation of Pumping Mechanism in Preexisting Capillary*”, IEEE sensors 2009, pp. 1349-1353, 2009.
- [36] B. Andò, S. Baglio, A. Beninato, “*An IR methodology to assess the behavior of Ferrofluidic transducers. Case of study: a contact-less*

- driven pump*”, *Sensors Journal*, IEEE, Vol. 1, No. 1, pp. 93-98, 2011.
- [37] R. Tadmor, R. E. Rosensweig, J. Frey, and J. Klein, “*Resolving the Puzzle of Ferrofluid Dispersants*”, *American Chemical Society, Langmuir* 2000, Vol. 16, pp. 9117-9120.
- [38] K. Larsson, K. Kriz, D. Kriz, (1999). “*Magnetic Transducers in Biosensors and Bioassays*”, *Analisis*, Vol. 27, No. 7, pp. 617-621.
- [39] K. Kriz, J. Gehrke, D. Kriz (1998). “*Advance toward magneto immunoassays. Biosensors and Bioelec.*”, Vol. 13, pp. 817-821.
- [40] D.R.Baselt, G.U.Lee, K.M.Handen, L.A.Chrisey and R.J.Colton, “*High-sensitivity Micromachined Biosensor*”, *Proc. of the IEEE*, Vol. 85, pp. 672, 1997.
- [41] S. Baglio, S. Castorina, N. Savalli, “*Integrated inductive sensors for magnetic immunoassay applications*”, *IEEE Sensors Journal*, Vol. 5, No. 3, pp. 372-384, 2005.
- [42] C. Serre, S. Martnez, A.Pérez-Rodríguez, J.R. Morante, J.Esteve, J.Montserrat, “*Si technology based microinductive devices for bio-detection applications*”, *Sensors and Actuators A*, Vol. 132, No. 3, pp. 499-505, 2006.
- [43] B. Andò, S. Baglio, A. Beninato, G. Fallica, V. Marletta, N. Pitrone, “*Analysis and design of inductive biosensors for magnetic immuno assay*”, *XIX IMEKO World Congress Fundamental and Applied Metrology*, pp.1729-1733, 2009.
- [44] B. Andò, S. Baglio, A. Beninato, G. Fallica, C. Galati, V. Marletta, L. Renna, “*Development of an integrated inductive sensor for mag-*

- netic immunoassay in lab on chip device*", Physcon 2009, pp. 189, 2009.
- [45] B. Andò, S. Baglio, A. Beninato, V. Marletta, "*An integrated differential inductive sensor implementing bio-immunoassay*", IEEE - Biosensing 2009



# *List of publications*

## *Book contributions*

- B. Andò, S. Baglio, A. Beninato, *Magnetic fluids for bio-medical application*, in “Advances in Biomedical Sensing, Measurements, Instrumentation and Systems” Springer – Verlag Berlin Heidelberg Publisher, Series: Lecture Notes in Electrical Engineering , Vol. 55, Mukhopadhyay, Subhas Chandra; Lay-Ekuakille, Aimé (Eds.) 2010, pp.16-28, ISBN: 978-3-642-05166-1, 2010.
- B. Andò, S. Baglio, A. Beninato, V. Marletta, G. Fallica, *Development of an integrated inductive sensor for magnetic immunoassay in “Lab on Chip” device*, in “From Physics to Control through an emergent view”, World Scientific Series on Nonlinear Science, Series B - Vol. 15, pp.163-170 edited by Luigi Fortuna, Alexander Fradkov, Mattia Frasca, World Scientific Publishing, 2010.

- B. Andò, S. Baglio, A. Beninato, V. Marletta, *Ferrofluids and their use in sensors*, in “Sensors Technologies”, CRC press, in press.

*International journals*

- B. Andò, S. Baglio, A. Beninato , *A low cost inertial sensor based on shaped magnetic fluids*, IEEE Transactions on Instrumentation and Measurement, in press.
- B. Andò, S. Baglio, and A. Beninato, *Can Ferrohydrodynamic Instabilities be Useful in Transducers?*, IEEE Magazine on Instrumentation and Measurements, Vol. 14, No.1, pp. 38-45, 2011.
- B. Andò, S. Baglio, A. Beninato, *An IR methodology to assess the behavior of Ferrofluidic transducers. Case of study: a contact-less driven pump*, IEEE sensors journal, Vol. 11, No. 1 , pp. 93-98, 2011.
- B. Andò, S. Baglio, A. Beninato, *Behavior Analysis of Ferrofluidic Gyroscope Performances*, Sensors & Actuators: A. Physical Vol. 162, Issue 2, pp. 348-354, 2010.
- B. Andò, A. Ascia, S. Baglio, A. Beninato, *A Ferrofluidic Inertial Sensor exploiting the Rosensweig effect*, IEEE Trans. on Instrumentation and Measurements, Vol.59, No.5, pp.1471-1476, May 2010.
- B. Andò, A. Ascia, S. Baglio, A. Beninato, *The “One drop” ferrofluidic pump with analog control*”, Sensors & Actuators: A Physical No. 156, pp. 251–256, 2009.
- B. Andò, S. Baglio, A. Beninato, S. La Malfa, N. Pitrone, *Advanced Educational Tools in Measurement and Sensors: from re-*



*mote monitoring systems to magnetic fluids*, Inter. Journal of Education and Information Technologies, Vol. 3, Issue 1, pp. 75-84, 2009.

*International conference proceedings*

- B. Andò, S. Baglio, A. Beninato, *A inertial sensor exploiting a spike shaped ferrofluid*, Instrumentation and Measurement Technology Conference (I2MTC), 2011 IEEE , pp. 1-5, May 2011.
- B. Andò, S. Baglio, A. Beninato, *A flow sensor exploiting magnetic fluids*, Proc. Eurosensors XXV, Athens, Greece, September 4-7, 2011.
- B. Andò, S. Baglio, A. Beninato, V. Marletta, *An integrated differential inductive sensor implementing bio-immunoassay*, IEEE - Biosensing 2009.
- B. Andò, S. Baglio, A. Beninato, G. Fallica, C. Galati, V. Marletta, L. Renna, *Development of an integrated inductive sensor for magnetic immunoassay in lab on chip device*, Physcon 2009, pp. 264-266, 2009.
- B. Andò, A. Ascia, S. Baglio, A. Beninato, *Innovative Ferrofluidic Inertial Sensor exploiting the Rosensweig effect*, IEEE, IMTC2009, pp. 1419-1422, 2009.
- B. Andò, S. Baglio, A. Beninato, G. Fallica, V. Marletta, N. Pitrone, *Analysis and design of inductive biosensors for magnetic immuno assay*, XIX IMEKO World Congress Fundamental and Applied Metrology, pp.1729-1733, 2009.

- B. Andò, S. Baglio, A. Beninato, *Behavior Analysis of a Ferrofluidic Gyroscope Performances*, Proceedings of the Eurosensors XXIII conference, 2009, pp.1-4.
- B. Andò, S. Baglio, A. Beninato, *A Novel Non-invasive Implementation of Pumping Mechanism in Preexisting Capillary*, IEEE sensors 2009, pp.1349-1353, 2009.
- B. Andò, A. Ascia, S. Baglio, A. Beninato, S. La Malfa, N. Pitrone, *Sensing a physical movement with a ferrofluidic device*, the 4th WSEAS International Conference on Remote Sensing (Remote'08), pp. 99-102, 2008.
- B. Andò, A. Beninato, S. La Malfa, N. Pitrone, *Didactic tool assisting visually impaired students during laboratory sessions*, the 7th WSEAS International Conference on Education and Educational Technology, EDU'08, pp. 190-193, 2008.

*National conference proceedings*

- B. Andò, S. Baglio, A. Beninato, S. Graziani, N. Pitrone, *Sensori basati sull'impiego di ferrofluidi*, GMEE Atti del Congresso Nazionale, 2009.
- B. Andò, S. Baglio, A. Beninato, S. Graziani, N. Pitrone, *Sensori basati sull'impiego di ferrofluidi*, GMEE Atti del Congresso Nazionale, Gaeta, pp. 90-91, 2010.
- B. Andò, S. Baglio, A. Beninato, S. Graziani, S. La Malfa, V. Marletta, N. Pitrone, F. Pagano, E. Umana, *Sviluppo di sistemi sperimentali innovativi di ausilio alla didattica*, GMEE Atti del Congresso Nazionale, Gaeta, pp. 288-289, 2010.

- B. Andò, S. Baglio, A. Beninato, G. L'Episcopo, *Strategie di sviluppo e fabbricazione di nanosensori*, GMEE Atti del Congresso Nazionale, 2011.
- B. Andò, S. Baglio, A. Beninato, S. Graziani, *Un sensore di flusso basato su fluidi magnetici*, GMEE Atti del Congresso Nazionale, 2011.
- B. Andò, S. Baglio, A. Beninato, *Transducers adopting magnetic fluids*, Convegno nazionale sensori 2012